PRECISION POLISHING DYNAMICS: THE INFLUENCE OF PROCESS VIBRATIONS ON POLISHING RESULTS

by

Mohammad Mainuddin

A dissertation submitted to the faculty of
The University of North Carolina at Charlotte
in partial fulfillment of the requirements
for the degree of Doctor of Philosophy in
Mechanical Engineering

Charlotte

2014

Approved by:

_____
Dr. Brigid Mullany

_____
Dr. Christopher Evans

_____
Dr. Matthew Davies

_____
Dr. Wesley Williams

_____
Dr. Xingde Dai

ABSTRACT

MOHAMMAD MAINUDDIN. Precision polishing dynamics: the influence of process vibrations on polishing results. (Under the direction of DR. BRIGID MULLANY)

The optical pitch polishing process has been used over 300 years to obtain high quality optical surface finish with little subsurface damage. A pitch tool consists of a metal platen coated with a layer of polishing pitch whereby pitch is a highly viscoelastic material. In polishing the workpiece is rubbed against the tool while abrasive slurry is supplied in between them. During polishing the workpiece is subjected to process vibrations, whereby be these vibrations are generated by the machine itself due to moving parts, or that are transmitted from the shop floor through the machine to the workpiece. To date, little is available in the public domain regarding the role of process induced vibrations on polishing outcomes. This research investigates such vibrations, how they transfer through the pitch layer on the tool, and ultimately how they affect the material removal rates and surface finishes obtainable on fused silica workpieces. Fundamental understandings with respect to the process vibration will reduce the heuristic nature of pitch polishing and generate deterministic polishing outcomes.

Key findings include the following. The pitch selection has little influence on the magnitude or range of process vibrations transmitted through the tool to the workpiece in the 1 Hz to 16 kHz range. Within the same frequency bandwidth the recorded process vibrations are in the range of 0.2 to 10 nm and the main factors found to affect their magnitude include; the polishing machine itself, process speeds, and the use of passive damping materials in the tool construction. Material removal rates and surface finishes obtained on fused silica workpieces were found to be sensitive to the extent of the

process vibrations. Up to 30% changes in the material removal rates were observed with increasing vibrational magnitudes. The higher level vibrations were also found to have a negative impact on the finishes obtained in the lower spatial domains. Additional testing on a specifically made test-bed demonstrated a linear correlation between the material removal rates and the vibrational power input. This relationship was further explored by adding external vibrational sources to an existing machine, and as expected the increased vibrational power resulted in 80% higher material removal rates. The results from this experimental work facilitated Dr. Keanini's development of a vibrational based material removal model. Additional polishing tests combined with surface topography analysis of both hard and soft pitch tools demonstrated the robustness of the proposed model to accommodate the influence of different pitch grades.

The summary in general is that in pitch polishing the process vibrations are important to monitor and control for process optimization.

ACKNOWLEDGMENTS

First and foremost, I thank the ALMIGHTY for having bestowed the blessings on me and giving me the strength to complete my dissertation.

I would like to express my deep sense of appreciation and sincere gratitude to my PhD supervisor, Dr. Brigid Mullany, for supporting me during these past years. Ever since, she has supported me not only by providing a research assistantship over four years, but also academically and emotionally through the rough road to finish this dissertation. Her wealth of knowledge in the field of precision manufacturing, particularly in surface finishing, is very inspiring. I must appreciate the opportunity she provided me to grow in this field, believing in me and giving me the firm foundation to be a good researcher. She spent enormous amount of time cooperating me to improve my writing skills and there is no way that I can show my gratitude to her patient and effort she contributed on my writing. The joy and enthusiasm she has for her research was contagious and motivational for me, even during tough times in the PhD pursuit. She has been supportive and has given me the freedom to pursue various experiments without objection. I am also thankful for the excellent example she has provided as a successful woman engineer and professor. I hope that there will be many more collaborations between us in the time to come.

I also like to thank the members of my PhD committee especially to Dr. Christopher Evans for his thoughtful suggestions, constructive criticisms and advices at many stages of the research. Special thanks to Dr. Wesley Williams for his time he spent to evaluate the sub-surface damage (SSD) of various samples. I am grateful to Dr. Matthew Davies, for his time and insightful questions. I would like to thank Dr. Xingde

Dai for his time and considerations. Out of my PhD committee, I extend my sincere gratitude to Dr. Russell Keanini for his immense contribution to develop the material removal model. To be honest, without him it would not be possible by us to develop the fluid based polishing model. I would also like to express my appreciation to Dr. Tony Schmitz for reviewing the approach we used to calculate vibrational energy and providing additional suggestions.

I wish to thank Dr. Mesbah Uddin for helping me bringing here in UNC Charlotte. Sincere thanks to Dr. Harish Cherukuri for his kind support to transfer eighteen credits hours from my MS course work into PhD program. The credits transfer reduced my overall course requirements in PhD and thereby allowed me to perform more research work.

I express my heartfelt thanks to Dr. Jonathan Beaman, post doc fellow, for all of his initial help regarding pitch tool making. He always provided helpful suggestions. Special thanks to graduate student Eric Browy for helping us to make the test-bed, to me he is an inspiring personality. I very much appreciated Joel Pritchard, Faculty Associate for Manufacturing Lab, for his enthusiasm, intensity, willingness to train me on various machines in machine shop. He is so friendly and I enjoyed a lot of talking to him on various topics even out of my research work. I am also grateful to Dr. Haitao Zhang and his student Sheng Tao for helping us to measure the SEM images.

A good support system is important to surviving and staying sane in grad school. I was lucky to be a part of center for precision metrology (CMP) at UNCC, the best precision metrology institute in the world, where I have been surrounded by wonderful colleagues who have provided a rich and fertile environment to study and explore new

ideas. I would like to thank Dr. Robert Hocken, Director of CMP, who has been extremely supportive in allowing me to participate in lab activities. I appreciate Greg Caskey, Metrology Lab Manager, for providing me training on optical interferometers and Talysurf surface profilers. His strictness taught me how to handle expensive instrument. Thanks to John Brien, a nice and helpful person, he helped me to design and fabricate the electrical circuit that controls the test-best operation. I am very grateful to Dr. Jimmie Miller, chief engineer at CPM, for his scientific advice and many insightful discussions. I also like to gratefully acknowledge to the funding sources that made my PhD work possible. I was funded by the National Science Foundation (Grant No.0747637).

I owe my deepest gratitude to some staffs in UNCC. I would like to show my best gratitude to Tracy Beauregard, Student Services Specialist in Mechanical Department, who has made available her support in a number of ways. She is awesome lovely and really smart in providing academic advises for a wide range of area. I appreciate Marion Cantor, Motorsports Business Service Specialist, for all of her helps for purchasing stuffs and making travel reimbursements. My grateful thanks to all staffs in International Student and Scholar Office (ISSO) for providing their supports in various way to continue my study in UNCC. Thanks to Rebecca Urquhart, Tax Specialist in UNCC, for her time to prepare ‘tax treaty benefits’ paper works every years.

I am thankful to other past and present group members that I have had the pleasure to work with, grad students Mark Marcos, SERU student Racheal Pedent, and the numerous summer and rotation students who have come through the lab. I also like to thank grad student Dr. Feilong Lin (for his help on initial MATLAB coding and

LabVIEW programs), Jacob Chesna (insightful discussions about cap gauge measurement), Jeffery Thousand (debugging LabVIEW program), and Dr. Sam Hellman, Dr. Samira and Bishuda (they provided supporting materials for PhD qualifying examination). Thanks go to some of my friends in UNCC, Dr. Mohammad Saad, Deepak Kohli and Abu Mohammad Ali, for their inspirational discussions during my stay in UNCC, I feel comfortable to call them anytime about any issue.

My times at Charlotte have been enjoyable in large part due to the many friends and groups that became a part of my life. I thank my friends (too many to list here but you know who you are!) for providing support and friendship that I needed. I must thankful to Sajjad Husain (Udoy) for being supportive brother throughout my time here in Charlotte. He provided his house for last three years with a rent lower than usual. Thanks must go to other community members and grad student in UNCC from Bangladesh like Ashiqur Rahman, Jahed, Ahrar, Reza, Saurav, and Estiak, thanks to all for banding together over social meeting, games playing and life; thanks for just being there for me. I couldn't have survived in Charlotte without them.

Lastly, I would like to thank my family for all their love and encouragement. For my parents who raised me with a love of science and supported me in all my pursuits, their support has been unconditional all these years. Their prayer for me was what sustained me thus far. I would like to pursue my thanks to my brothers, sisters and their families for all of their supports and encouragements. And most of all for my loving, supportive, encouraging, and patient wife Kh. Ehsana Rahman (Hridita) whose faithful support during the final stages of this PhD is so appreciated. Thank you.

TABLE OF CONTENTS

LIST OF ABBREVIATIONS

ADC	analog to digital converter
AFM	Atomic Force Microscopy
AL	aluminum substrate
Asoft	Acculap™Soft
Avf	Acculap™VeryFirm
BK7	Borosilicate glass
CI	cast iron substrates
CMP	chemical mechanical planarization
DAQ	data acquisition
DI	digital Instruments
DSA	dynamic signal analyzer
EDS	energy dispersive spectroscopy
FE	finite-element
FWHP	full width half power
Gsoft	Gugolz55 pitch
Gvf	Gugolz73 pitch
HDPE	high density polyethylene
HF	hydrofluoric acid
Hz	hertz ($second^{-1}$)
IC	integrated circuits
MS	mild steel /steel substrate
MSF	mid-spatial frequency

MRF	Magneto Rheological Finishing
MRR	material removal rate
NA	numerical aperture
PSD	power spectrum density
PZT	piezoelectric
SEM	Scanning Electron Microscopy
SSD	sub surface damage
Stdev	standard deviation
SWLI	Scanning White Light Interferometer

LIST OF SYMBOLS

A	amplitude, area
Å	angstrom
E	modulus of elasticity
f	frequency
g	gram, gravitation acceleration
h	height
k	kilo
K	spring constant, particle concentration
Kg	kilogram
l	length
mg	milligram
mm	millimeter
P	power, Load
p	pressure
Pa	Pascal
r	radius
R_a	average roughness (line / profile)
R_q / R_{rms}	root mean square roughness (line / profile)
S_q	root mean square roughness (areal)
t	time
v	velocity
ω	angular velocity

λ	light wavelength, ripple wavelength
σ	stress rate, standard deviation
ε	strain rate
μm	micrometer
η	coefficient of viscosity
ζ	damping ratio
θ	geometric angle
Ø	diameter
%	percentage
~	approximately
≈	equivalent
δ	characteristic elastic deformation

DISCLAIMER

This material is based upon the work supported by the National Science Foundation under Grant No. 0747637. Any opinions, findings, and conclusions or recommendations expressed in this material are those of the authors and do not necessarily reflect the views of the National Science Foundation.

CHAPTER 1: INTRODUCTION

1.1 Introduction and Motivation for Current Work

The overall goal of this work is to determine if the vibrations in polishing processes have a significant influence on polishing outcomes such as material removal rates and surface finish and thereby better understand the process fundamentals to optimize the polishing process.

Optical pitch polishing process has been used for more than 300 years to obtain high quality optical surface finishes with little subsurface damage [1]. A pitch tool consists of a metal platen coated with a layer of polishing pitch whereby pitch is a highly viscoelastic material derived from tree resin [2]. Synthetic versions are also produced [3]. At room temperature the pitch is a stiff, brittle material with Shore D hardness values ranging between 70 and 83 [2]. Polishing with pitch was first introduced by Sir Isaac Newton in the 1700's and has since been used to produce high quality optical surfaces [1]. Pitch polishing can generate surfaces with roughness and flatness values less than 1 Å RMS and $\lambda/20$ respectively (where $\lambda = 632$ nm) [5]. However the polishing processes using these tools has not received the same level of scientific investigation as other precision processes such as milling, grinding, etc. [6]. Pitch polishing researchers have done extensive work on investigating polishing process aspects such as pitch properties, tool parameters, slurry composition (chemical and mechanical properties), tool-slurry-workpiece interaction, workpiece material, and basic process parameters such as

polishing load and relative velocity. To date, little is available in the public domain on the dynamic aspects of pitch polishing processes, i.e. how do process vibrations impact material removal rates and surface finishes?

Process vibrations are considered to be the vibrations generated by the machine itself, due to moving parts, or that transmitted from the shop floor through the machine to the workpiece. The role of process vibrations did not receive much attention until recently in 2010 when Mullany et al. investigated the dynamic response of different polishing pitches [7]. The investigation revealed that each grade and type of pitch has unique dynamic properties (dynamic stiffness, damping ratio, natural frequency) and that pitch types, which have the same long term response, have different short term dynamic responses. This leads to the question; can these differences account for the different polishing results obtained when using different types of pitch? A key component of answering this is to understand the extent and magnitude of vibrations existing in polishing processes, how they interact with the pitch tooling, and what impact, if any, do they have on polishing mechanisms.

1.2 Application of the Research

The dynamic properties of pitch and their impact on polishing processes have never been fully evaluated. The measurements of process vibrations and the evaluation of their impact on process outcomes will enhance the fundamental understanding of polishing material removal mechanisms and provide opportunities for process monitoring and statistical process control. The ability to monitor and control the process will facilitate process automation and undoubtedly process automation is the key to generate repeatable polishing outcomes. This research will reduce the dependency on worker

experience and heuristic nature of pitch polishing outcomes and thereby enhance the deterministic outcomes. Optimization of the polishing process will significantly reduce polishing time and cost associated with high quality optical surface generation. Better optical components could be generated at a lower cost for a wide range of applications that include metrology instruments, astronomical lenses and other high quality laser equipment. The knowledge could be implemented in other machining process such as grinding, ultrasonic finishing etc. Innovative explanations of the correlation between process vibrations and the process outcomes in pitch polishing will also help better understanding the chemical mechanical planarization (CMP) process in IC industries.

1.3 Structure of the Dissertation

The dissertation starts with a literature survey that reviews the history of pitch polishing, its application, the existing knowledge and the gaps in our knowledge. The physical and dynamic properties of pitch are explained. An overview of the polishing process, the key parameters for characterizing polishing outputs and the existing material removal mechanisms are provided. The dynamic aspects of the polishing process are scrutinized and tabulated, particularly focusing on the material removal rate (MRR) and surface finish (roughness).

Chapter 3 investigates the dynamic response of different pitch grades, types and tools to different vibrational inputs. Factors considered include; pitch grade, pitch type, and tool geometry. The tests are subcategorized in to two sections, frequency sweep tests and impact frequency tests. The frequency sweep tests investigate how vibrations transmit through pitch while the impact tests evaluate the dynamic response of pitch to

transient vibrations. This chapter also provides details on tests conducted to evaluate the ability of a wide range of passive damping materials to attenuate process vibrations.

Chapter 4 is concerned with quantifying the vibrations existing during actual polishing processes, and how they affect the material removal rates (MRRs) and surface finishes obtained on fused silica samples. The vibration measurement system and analysis approach are described. The impact of tool selection, machine, and process parameters on the vibrations are considered. The chapter concludes by presenting the polishing tests results and by offering insights into how the process vibrations affect the MRRs and surface finish.

Chapter 5 outlines a test-platform specifically designed, and fabricated to analyze the effect of vibration frequency and amplitude on polishing outcomes in a controlled manner not possible on actual polishing machines. Fused silica samples were polished on the test bed and the results analyzed. The results from these tests provide the basis for a new material removal model developed by Dr. Keanini, which combines both mechanical and fluid dynamics aspects. The chapter ends with a summary of the model and explains the results with respect to the experimental results.

In chapter 6 SEM and AFM evaluations of both a hard and soft tool are presented. The differences in the tool topographies and the polishing results obtained on fused silica are considered with respect to the material removal model developed by Dr. Keanini (see chapter 5).

Chapter 7 investigates the possibility of applying external vibrational sources to the polishing machine so as to induce higher removal rates. Small, low cost, battery

operated unbalanced motors running at speeds between 10 and 15 krpm were used to generate additional vibrations.

Chapter 8 summarizes the overall findings from the previous chapters, discusses the results, and provides recommendations for future work. Finally the appendices contain relevant programming codes and additional supporting information.

CHAPTER 2: LITERATURE REVIEW

2.1 Pitch Polishing Process

There are a number of polishing techniques available to generate high quality optical surfaces. Chemical mechanical planarization (CMP) [13], magneto-rheological finishing (MRF) [14], laser polishing [15], float polishing [16], Jet Polishing [180, 22], ion-beam polishing [17], and traditional polishing [8, 11] are some examples of them. Traditional polishing can be categorized into two sub-divisions: 1) continuous polishing, also known as a full-aperture technique, where the tool diameter is larger than workpiece diameter [18], and 2) sub-aperture techniques where the tool is smaller than the workpiece [19]. Polishing with pitch tooling primarily corresponds to the full-aperture continuous process though it has applications in sub-aperture polishing too [181, 21]. Figure 2-1 classifies the different polishing processes.

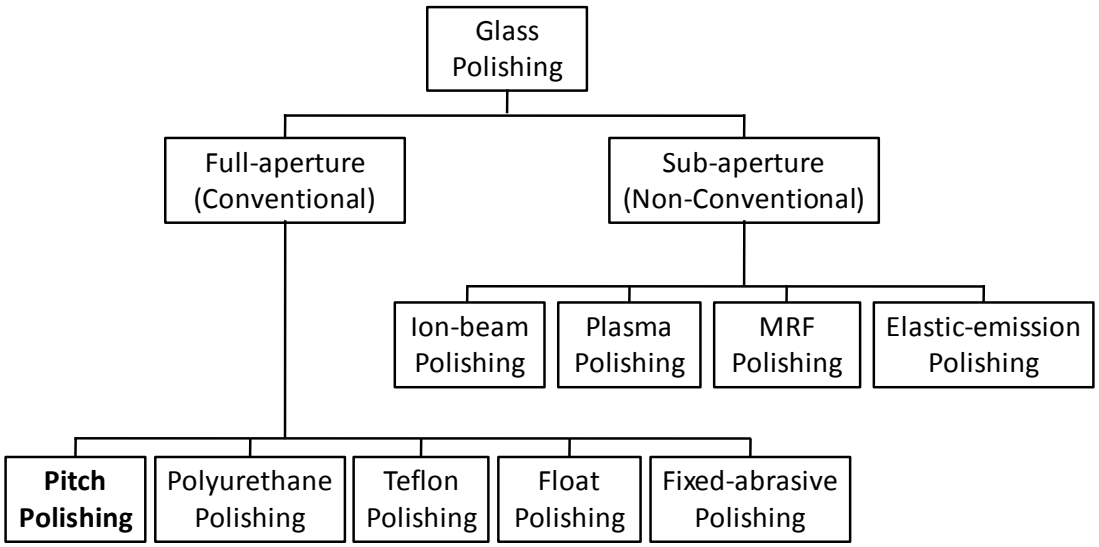

Figure 2-1 : Classification of basic glass polishing processes [20].

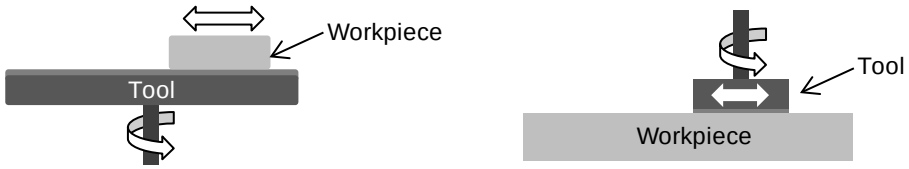

Full aperture Sub-aperture

Figure 2-2: Schematic of full aperture and sub-aperture polishing process.

Figure 2-2 presents schematics of full and sub-aperture polishing process setups. In full-aperture pitch polishing, the tool consists of a layer of pitch on a metal platen that has a diameter larger than the workpiece. Pitch is a viscoelastic material that slowly deforms under pressure [11]. During polishing the workpiece surface (glass) is pressed against the pitch tool surface, and slurry consisting of abrasive particles mixed with liquid (usually water) is added to the system throughout polishing. Before polishing the tool is conditioned so as to create a layer of embedded abrasive particles in its top most layer, without this crust little material removal is expected. Material is removed by the relative motion between the tool and the workpiece in the presence of slurry. To aid slurry delivery to the workpiece surface grooves are cut into the tool surface. These grooves promote better slurry circulation and the transfer of polishing debris away from the workpiece. Pitch tooling has the ability to produce surfaces with sub-nanometer level of finishes and very little sub-surface damage [5]. Its ability to achieve these results is partially due to its ability to deform slowly under loading thus facilitating good contact between it and the workpiece.

2.2 Pitch Polishing Components

The basic elements used in pitch polishing processes are the pitch tool, the slurry, and the workpiece. This section briefly highlights the basics associated with each element.

2.2.1 Pitch Tool

A pitch tool consists of a layer of pitch on a metal substrate. The layer thickness varies from user to user and could be from a few millimeters to several centimeters. The life span of such tooling ranges from a few days for smaller tools to over a year for the larger tools [7].

In a basic tool making process the pitch is first softened by controlled heating to make it pourable, it is then poured onto the platen [70 - 73] and allowed to cool for several hours (often overnight). Before use grooves are cut into the top surface of the pitch layer whereby these groves will assist in slurry supply and debris removal. Attention should be given to both grooving depths and patterns as they can affect the overall compliance and performance of the pitch tool [11]. Pitch grooving dimensions, when represented in a dimensionless form (ratio of depth to thickness), range from 0.01 to 1[11]. Figure 2-3 illustrates a typical pitch tool with grooving. The common facet shapes are square, equilateral triangle or a combination of both [11].

Figure 2-3: pitch tool with grooving [24].

2.2.2 Polishing Pitch

Pitch is primarily derived from either pine tree (natural) or petroleum based products. The petroleum-based pitch is commercially named as Cycad™, and the most common wood based pitch is sold as Gugolz™. The synthetic versions are also available [3] and are sold under the trade name Acculap™. For natural pitch the basic properties slightly vary from batch to batch and with preservation time. The reason for possible variations includes the evaporation of the solvents added to the natural pitches to control its hardness values. The synthetic versions developed in the laboratory are more stable, consistent, and resistant to chemical attack, including high temperature oxidation or degradation. The Acculap™ range of pitches were designed to perform just as natural pitches of comparable hardness [56]. The softening temperatures and handling procedures are similar for both. Pictures of natural and synthetic pitches are illustrated in Figure 2-4 [58].

Natural pitch
Trade name: Gugolz™

Synthetic pitch
Trade name: Acculap™

Figure 2-4: Synthetic and Natural pitch [58].

At room temperature the pitch is a stiff, highly viscous and brittle material (see Figure 2-5)with Shore D hardness values ranging between 70 and 83 [2]. As it has the ability to flow under pressure, which enables different removal rates between high and low contact points on the optical surface which reduce mid and high spatial frequency

errors [21]. Therefore, pitch polishing is considered for many high end optical components such as lithography, laser, military or astronomy based optics. Despite its advantages pitch has some limitations. Natural pitch contains solvents which with time dry out, making the pitch harder. All types of pitch are temperature sensitive, a 5 °C change in temperature can change the pitch grade (hardness) [11]. Besides these points, pitch polishing is a very slow material removal process, it relies highly on operator experience [23] and can have consistency issues.

Figure 2-5: a. Pitch a very high viscous liquid, b. Brittle fracture resulted from an impact hit [**7**].

2.2.3 Pitch Properties

2.2.3.1 Hardness

According to Norman J Brown [11] “Pitch flow affects lapping in at least two ways 1) allowing polishing agent particles of polishing agent to seat into the pitch surface and 2) enabling the lap to mate with the surface being polished.” According to his observation the ability of pitch to alter its form depends on the grade (hardness) of pitch. Hardness values are very temperature dependent. For a good polishing outcome, selection of the correct pitch hardness is important. Soft pitches allow more slurry particles to embed in tool surface and this will have a great influence on polishing outcomes [11].

Harder pitches are more difficult to condition (i.e. embed particles within its surface). Harder pitches generate higher surface roughness values [2]. Proper combination of pitch and glass hardness can improve removal by a factor of two [10]. Twyman recommended softer pitch for softer materials while Izumitani [10] found harder pitches produce finer surfaces on soft glass. Several methods are proposed to measure hardness of pitch [2, 59, 60]. Gillman [2] and DeGroot [60] describe two different tests capable of assessing the hardness of pitch; the indentation test (see Figure 2-6), and the durometer test.

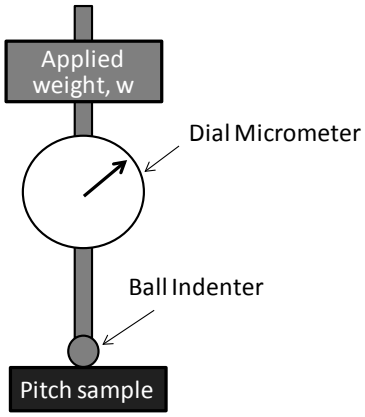

Figure 2-6: Schematic of an indentation test setup.

Table 2-1: Comparable hardness between natural and synthetic pitches [2, 56].

Synthetic Pitch	Natural Pitch	Shear Viscosity (GPa-s)*	Shore D Hardness	Softening point (°C)
Acculp™ Very Soft	--	0.05	--	--
Acculap™ Soft	Gugolz 55	0.1	60	63-64
Acculap™ Standard	Gugolz 64	0.8	72	65-68
Acculap™ Intermediate	--	1.1	--	68-70
Acculap™ Very Firm	Gugolz 73	8.0	80	71-74
Acculap™ Very Hard	Gugolz 82	70	85	75-77

* For T = 20 °C

Gillman also determined softening points for different pitch grades and found that harder pitches have higher softening point temperature. The comparable hardness between Gugolz™ and Acculap™ are provided in Table 2-1 [2, 56].

2.2.3.2 Viscosity

Polishing pitch is a viscoelastic material, similar in nature to road pitch or asphalt. Various materials exhibit viscoelasticity, where the deformation depends on the applied load, time, and temperature. Viscoelastic materials have a mix of material properties. When they undergo deformation they exhibit both viscous and elastic behavior. Viscosity is the resistance of fluid to shear loading under a shear load. Elasticity is the ability of a material to return to its original shape after the removal of the applied load that deformed it [66]. In the case of pitch, its viscous component is more dominant than its elastic component [2].

According to Newton's laws of viscosity the shear stress is directly proportional to the rate of deformation [65], i.e. the shear stress τ can be defined as, $\tau = \mu \times d\varepsilon/dy$ (Pa or N/m^2) where $d\varepsilon/dy$ is the rate of deformation due to the shear load. The proportional constant μ (N/m) is called the viscosity. Higher viscosity fluids require higher shear loads to flow. Viscosity is temperature dependent. At room temperature pitch appears solid with very high viscosity values (Table 2-1) while at higher temperatures (>60 °C) it is more fluid. Brown [11] found pitch viscosity changes by a factor of two for every 2 to 3 °C change in temperature while Twyman [59] found the exponential dependency of pitch viscosity with temperature. Harder pitches have a higher viscosity value, i.e. a greater resistance to flow.

2.2.3.3 Dynamic Behavior

The dynamic behavior of pitch has not received much attention even though pitch polishing tools have been used for more than three centuries. Until recent publications by Mullany et al. [63, 64] no literature was found that dealt with the dynamic properties of pitch. Mullany and Corcoran [61 - 63] showed a correlation between pitch hardness and dynamic properties such as damping ratios and the natural frequencies.

2.2.3.3.1 Impact Frequency Response: Evaluation of Natural Frequency

Mullany et al. [7, 61-64] used impact tests as a method of characterizing pitch and pitch tools. Impact testing was used to determine the damping ratio and natural frequency of different pitch grades and types. The measured natural frequency and damping ratio of some common pitch types are presented in Figure 2-7. The figures illustrates that each pitch type has unique natural frequency and unique damping ratio. Harder pitches have higher natural frequencies and lower damping ratios, which implies that a pitch with a higher natural frequency is more resistant to deformation. Indent and impact testing on pitch samples of different ages indicated that over time natural pitches become harder and the dynamic stiffness also increases [7]. They also evaluated the effect of temperature on pitch hardness and its dynamic properties. Higher temperatures soften the pitch and thereby reduce their natural frequency values [61].

Mullany's [7] analysis provides some insights into why natural and synthetic pitches with comparable hardness values give different polishing outcomes. They analyzed two types of pitches (Gugolz or Acculap) and for each of the series they found a separate linear relationship between the natural frequency values and the hardness of material.

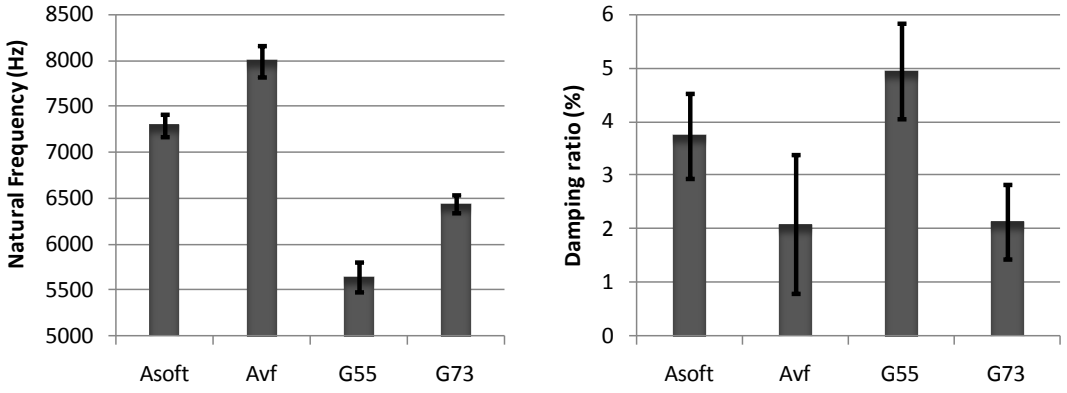

Figure 2-7: The natural frequency and damping ratio measurements of different pitches from reference [7].

Figure 2-8 represents the plots of hardness versus natural frequency for the two series. The hardness was evaluated by indentation test. They found different dynamic characteristics associated with the two types of pitches evaluated. They concluded that two different types of pitches may have similar hardness but can have different dynamic properties, and that this may result in different polishing outcomes.

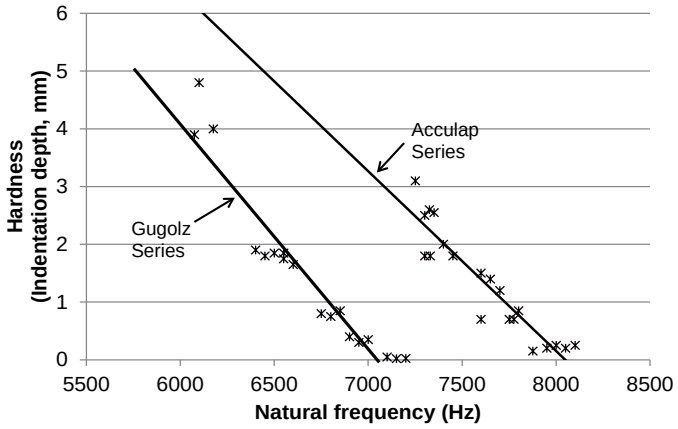

Figure 2-8: Mullany's findings, hardness versus natural frequency for Gugolz and Acculap series [7 (modified from the paper)].

2.2.4 Workpiece/Glass

Optical grade glass is characterized by well-defined optical properties, optical homogeneous performance and the absence of bubbles, strains and inclusions. The majority of the polishing tests conducted in this work were done on fused silica samples. Fused silica is the purest form of silicon dioxide (99.99%) in amorphous form i.e. a non-crystalline form of silicon dioxide (SiO_2) [75]. Single constituent in fused silica makes chemical reaction more straight forward when compare to other glasses with multiple constituents [77, 78]. In this work the experimental tests concerned with tool conditioning utilized Bk7 glass for economic reasons (significantly cheaper than fused silica [76]). Bk7 is a barium borosilicate glass which has very good optical properties.

2.2.5 Abrasive Polishing Slurry

A polishing slurry consists of an abrasive - liquid mixture. Water is typically the base liquid used. Different abrasive particles are used in pitch polishing process depending on workpiece material and required surface finish. Cerium Oxide (ceria), Aluminum Oxide (alumina), Iron oxides, Zirconium oxide, Silicon Carbide, Cubic Boron Nitride (CBN), and diamond are the most common abrasives used in polishing process [22, 81]. Ceria is a very popular polishing compound for a variety of optical materials [81, 82]. For a workpiece material like fused silica, ceria based slurries can provide the best removal rate when compared to other abrasive types [11, 12, 81]. Ceria is a rare earth oxide that can be acquired, purified and processed for commercial use. As abrasives chemically react with workpiece material, their chemical composition can have a profound influence on the polishing process and process outcomes [83]. Some basic properties of CeO_2 are provided in Table 2-2 [85, 86].

Table 2-2: Some physical properties of pure CeO_2.

Property	Value (unit)
Density	7.22 g/cm^3
Melting Point	2477 °C
Youngs' Modulus	1.65×10^{11} N/m^2
Hardness	Mohs Hardness 6
Crystallography	Cubic, face centered
Solubility in Water	Non-soluble

While CeO_2 hardness is lower than that of fused silica, the chemical interaction between the slurry (abrasive and water) and the workpiece create a hydrated layer on the silica surface which is softer that CeO_2 [121]. The mixing ratio (water: ceria) has a broader impact on the removal rate. The most common ratio that used in pitch polishing process is, H_2O:CeO_2 = 10: 1 [11, 25, 84, 125].

2.2.6 Polishing Metrics

The polishing metrics typical encountered include; material removal rate (MRR), surface finish (roughness), and subsurface damage (SSD). A brief review of the literature for each of the metrics is reported in following sections.

2.2.6.1 Material Removal Rate (MRR)

Material removal rate is the loss of material over time. In the polishing world the typical approaches to determining the removal rate are to measure the mass loss of the workpiece per unit area, or to measure the change in physical dimension, i.e. height reduction [9, 11, and 12]. In the mass measurement method the sample is weighed before and after polishing. This method is subject to some potential errors such as cleanliness of the part after exposure to the slurry and water absorption by the workpiece (which can

also be a function of humidity [24]). While in the latter approach, the change in physical dimension, the material removal rate is determined based on the change of physical height of a workpiece before and after polishing. In the reviewed literature most of the authors utilized the change of physical height to evaluate the material removal rates although the mass loss method was importantly considered by some researchers. Some used both to cross check the variation [9, 24, and 25]. Table 2-3 presents the removal methods used in the published polishing related papers.

Table 2-3: Pitch Polishing removal rate of SiO_2 and BK7 glasses in reported work.

References	Glass Type	Slurry (size ~1 µm)	Mass Loss ($g/cm^2.s$)	Height Loss (µm/min)	Preston coefficient C_p, (cm^2/dyne)
Izumitani[9]	SiO_2	CeO_2	3×10^{-6}	0.02	2×10^{-14}
	SiO_2	SiO_2	7.3×10^{-8}	0.00005	- -
	BK7	CeO_2	- -	0.12	1.2×10^{-13}
A. A. Tesar [25]	SiO_2	CeO_2	2.2×10^{-7}	0.06~0.16	$6\text{-}16\times10^{-14}$
	Zerodur	CeO_2	2.6×10^{-7}	0.07	7×10^{-14}
Landis [24]	SiO_2	CeO_2	- -	0.007	2.8×10^{-14}
	Quatz	CeO_2	- -	0.0003	0.14×10^{-14}
	Zerodur	CeO_2	- -	0.006	7.3×10^{-14}
W. Silvernail [26]	SiO_2	CeO_2	- -	0.1	- -
A. Kaller [27]	SiO_2	CeO_2	- -	0.03~0.05	- -
M. J. Cumbo [31]	SiO_2	CeO_2	- -	0.013	- -
	BK7	CeO_2	- -	0.04	- -

Note: In some of the references the removal rates are available for various pH, while in this table the removal rate only presented for slurry pH=7.

2.2.6.2 Surface Quality

The ultimate performance of fine polishing processes can be determined by their achievable surface quality. The roughness, waviness and the form error of the resulting surface are considered in high-end glass polishing process.

Surface roughness is the closely spaced irregularities which measure the texture of a surface, waviness is more widely spaced surface textures when compared to that considered as roughness, and the flatness is the long spaced deviation, see Figure 2-9.

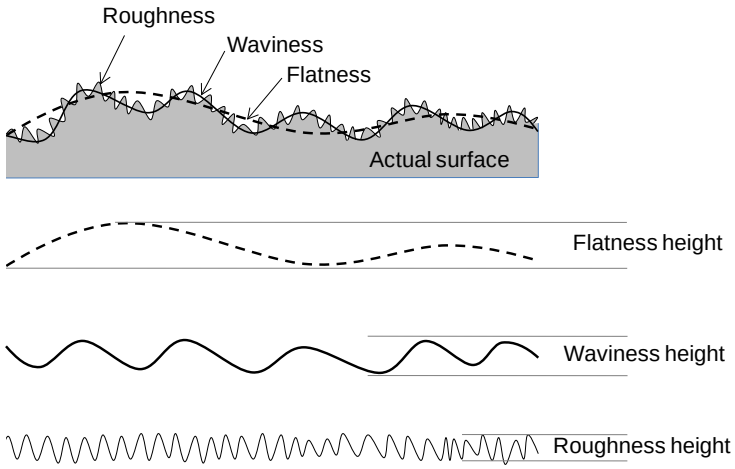

Figure 2-9: Schematic of surface roughness, waviness and flatness (form).

For 2D measurements (line profile) the arithmetic mean of all the roughness heights is denoted by R_a, the average roughness, while the root mean square (RMS) roughness is denoted as R_q. If the roughness is calculated over an area (3D), for example by using optical interferometry measurements, then the average and RMS roughnesses are denoted by S_a and S_q respectively. In addition to the roughness, an additional term R_{sk} (2D) or S_{sk} (3D) the skewness, is considered. This term indicates the deviation of height distribution from normal curve, i.e. if the surface contains more peaks (positive skewness) or valleys (negative skewness). Many other parameters are available to

describe surfaces and readers should refer to the following sources for additional information [183].

In the optics industry surfaces features are often characterized with respect to their spatial frequency domain [28]. Spatial frequency demonstrates the lateral distance between cyclic irregularities, where the total spatial distance is split in to three categories, low, mid, and high spatial frequency domains, see Figure 2-11. The lower spatial frequency domain is associated with the form of the surface, the mid-spatial frequency domain is associated with surface waviness, and the high spatial frequency domain corresponds to surface roughness.

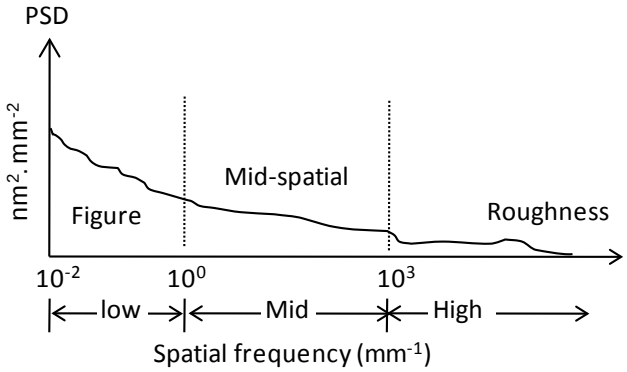

Figure 2-10: the low, mid and high spatial frequency regions are indicated [29].

To evaluate the surface roughness various instruments can be utilized. The selected instrument type and the implementation technique depend on the ultimate requirements of the sample. Several research papers describing the techniques and limitations are available, including the paper by Vorburger [36], Lonardo et al. [37] and Komanduri [38], paper by Sakata et al. [39], De Chiffre et al. [40], and Whitehouse [41, 42] are few of them. There are two types of instruments used to quantify surfaces; contact type and noncontact type. For example the mechanical stylus systems (Talysurf,

Mitutoyo), AFM, and Talystep systems are contact types, while optical interferometers are of the noncontact type. The noncontact type has advantage over contact type in that this method is quick and it can measure without touching the surface. But in optical systems the measurement resolution is limited by the wavelength of optical light and the system's numerical aperture. Contact type measurements are typically slower, however in the case of AFM systems, the achievable lateral resolution can surpass that of optical systems. The lateral resolution of contact systems can be limited by the geometry of the contact probe. Lateral resolution refers to the smallest lateral/horizontal spatial distance measurable, while vertical resolution refers to the minimum vertical feature height distinguishable. A brief summary of the lateral and vertical resolutions, and ranges of some of the instruments used to examine surfaces are presented in Table 2-4.

Table 2-4: Resolution and range of some instruments that used to evaluate polished surfaces [38, 182, 183].

Instrument		Resolution (nm)		Range (mm)	
		Lateral	Vertical	Lateral	Vertical
Profilometer: Mitutoyo Surftest SJ-400		2000	5	12	0.35
Profilometer: Taylor Hobson Talysurf		250	16	> 100	1.0*
White Light Interferometer (SWLI)	2.5× Michelson	26000**	0.1	2-3	0.1
	50× Mirau	1280**	0.1	0.1-0.15	0.1
Atomic Force Microscopy (AFM)		2	<0.1	0.1	0.005

*For a standard stylus arm length of 57.5 mm.
**Based on Nyquist sampling limit (objective dependent).

2.2.6.3 Subsurface Damage (SSD)

In form generation processes, such as grinding and high volume lapping etc., the material is removed primarily by brittle fracture methods, which results in cracks forming

beneath the surface. These subsurface cracks are often not visible on a polished surface and are referred to as subsurface damage (SSD) [13, 38, 43 - 50], see Figure 2-11. SSD can reduce the strength of a material, promote the laser induced damage [46, 47], and reduce the life time of the component. P. P. Hed analyzed the relationship between surface roughness and the remaining SSD [51]. The use of finer abrasives during the form generation processes can reduce the depth of the resulting SSD [45]. During a sequence of finishing processes, the abrasive sizes are reduced at each step so that current step can remove the SSD layer left by previous step. Although the ultimate goal is to generate SSD free surfaces traditional polishing processes are not able to eliminate SSD completely. The goal is to reduce the level of SSD under certain limit depending on the application of the glass and the required specification.

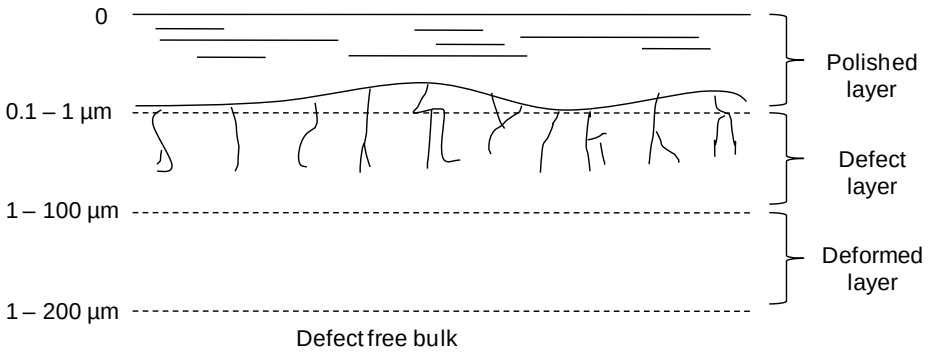

Figure 2-11: Schematic of Subsurface damage [53].

The topmost layers on a polished glass surface can conceal the damage generated by polishing or previous lapping and grinding processes. Chemical etching can reveal the scratches and pits beneath the surface [52, 53]. A number of methods can be utilized to measure the extent of SSD [28 - 32], the methods are classified as either destructive or nondestructive. Destructive methods can measure SSD more precisely but it destroys the

polished surface (chemical etching) while the nondestructive methods are complex and the equipment expensive (Optical tomography, Quantum dots, Laser scattering and confocal microscopy) [54, 55].

2.3 Process Kinematics: Polishing Mechanism

Over 300 years ago, when the optics industry began in earnest, polishing was thought of as a wear process. During last century numerous researchers have attempted to better explain the mechanisms and have proposed several theories [4-12], however none of them fully explain every aspect of abrasive polishing. The proposed theories can be broadly classified into three main categories: 1) mechanical removal theories, 2) chemical removal theories, and 3) chemical-mechanical removal theories. CIRP keynotes papers by Komandari et al. [38] and Evans, et al. [13] summarize the prevalent theories available. A brief review of each main category is presented in the following sections.

2.3.1 Mechanical Removal Theories

The material removal that is based on the purely mechanical interaction between the workpiece, tool, and abrasive particles contained within the slurry is denoted as mechanical removal. Removal takes place due to the relative motion between the two surfaces and interaction with the abrasive slurry. According to Rayleigh [87] the particles induce mechanical fracture and removal take places on the molecular scale. While Beilby [88] said the interaction between particles and workpiece generates frictional energy. The local heat generated from the frictional energy reduces the viscosity at the contact point and removal takes place by local flow of material. Yoshikawa [89] added, mechanical removal takes place due to the combined actions of material flow and brittle fracture. According to Yoshikawa, material flow creates initial cracks and the cracks propagate to

dominant brittle fractures.

Preston [8] defined mechanical removal by an empirically based mathematical model. According to his model the removal depends on the applied load and the relative motion between the workpiece and the tool. Preston's equation for material removal rate is given by:

$$MRR = C_p \times P \times V \qquad (2\text{-}1)$$

Where P stands for polishing pressure and V is the relative velocity between the tool and the workpiece. C_p is a proportional constant termed as Preston coefficient, which accounts of all the other factors (aside from pressure and relative velocity) that contribute to material removal [90]. Still today C_p is importantly considered to evaluate polishing efficiency. Some values of C_p are provided in Table 2-3. The values were determined from experimental tests and published in the references literature. Preston [8] also developed a model for polishing work, which considered the coefficient of friction, the contact area, and the polishing time along with pressure and velocity, see references [8, 11] for details.

In mechanical removal theories the removal results from ultimate contact between workpiece and abrasive particles. The tool and workpiece properties, the size and shape of the particles all have significant influence on removal rates. For example, the removal rate is proportional to the square root of the mean particle size [91]. Guanghui Fu [92] explained that the shape of the abrasive, whether sharp or spherical (blunt), has distinctive influences on the MRR. He found that the MRR depends on the yield strength of the work-surface and that the nature of dependency changes with particle shape. For either sharp or blunt particles, if tool and workpiece do not touch the MRR is independent

of tool properties, while when they touch each other, higher tool stiffness leads to higher removal rates, which indicates the influence of mechanical contact. Leistner et al. [30] analyzed the impact of tool textures. His analysis found that for a coarser tool the pressure between surface and lap is higher at contact zones and produces faster removal. In contrast, for a fine tool contact points are uniform and removal rate is slower. Although, regardless of the tool condition, i.e. coarser or smoother, Leistner found that a higher contact velocity produces higher mechanical action and resulted in higher removal rates.

2.3.2 Chemical Removal Theories

The material removal that based on the chemical reaction between the workpiece and the slurry is termed as chemical removal. According to this hypothesis the slurry particles chemically react with workpiece material and forms complex molecules. As the particles move along the workpiece surface the bonds between the workpiece and its surface atoms, now attached to the abrasives, are broken and thus workpiece material is removed. The removal take places on an atomic or molecular scale [88]. Temperature may play an important role in enhancing the chemical reactions [88]. For cerium oxide the reaction rate depends on the presence of hydroxyl ions i.e. slurry pH. The polishing rate is much lower with an oil based slurry when compared to a water based slurry [98, 10]. In case of silica glass polishing with cerium oxide mixed with water, chemical removal reactions take place in four different stages [12, 13].The reactions and the schematic of the removal mechanism are presented in Figure 2-12.

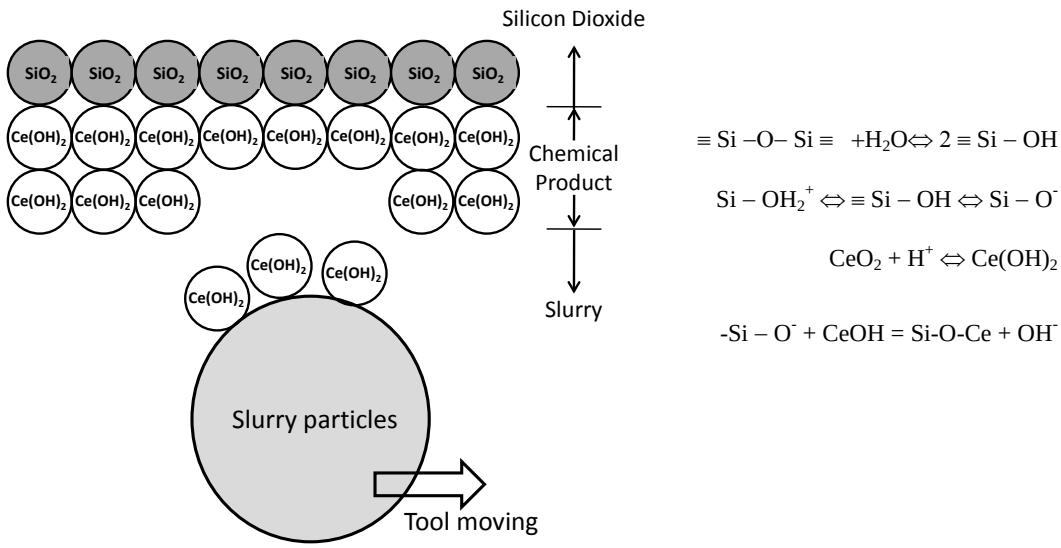

Figure 2-12: Chemical reaction and schematic of chemical removal.

2.3.3 Mechanical + Chemical Removal Theories

Izumitani and Harada [95] proposed that in glass polishing with abrasive slurry the removal mechanism take place with the attributes of both the mechanical and chemical aspects. They hypothesized that when in contact with an aqueous based slurry a softer hydrated layer (sub-nano meter thickness) develops on the glass surface and that this softer layer is then mechanically removed by abrasives particles. Their analysis found that the polishing rate is proportional to the rate at which the hydrated layer formed. The mechanism was further analyzed and modeled by Lee Cook [12]. He proposed that the particles embedded in the tool remove the chemically modified layer though a ploughing (mechanical) or plucking (chemical tooth) mechanism. As outlined by Cook [12], the chemical reactions presented in Figure 2-12 have several possible outcomes. If the Ce-O bond is weaker than the Si-O bond then the silica particles are retained on the glass surface (reposition) while if the Ce-O bond is stronger, the silica will be removed from the glass surface. Accordion to Cook, CeO_2 possess a strong

chemical tooth that transports the reaction products away from the surface faster than their rate of re-deposition.

In the chemical-mechanical hypothesis, the glass polishing rate is critically dependent upon the presence of water. The rates were observed to be nearly zero for hydrocarbons such as kerosene, paraffin, or oil. Cornish and Watt [96] reviewed cerium polishing rates relative to water for a series of alcohols and the rates were found to increase directly with increasing hydroxyl components. Similarly, Silvernail and Goetzinger [97] studied cerium polishing rates in a series of ethylene glycol and water mixtures and the rates were extremely low in pure ethylene glycol, increasing logarithmically with the molar concentration of water. Nogami et al. [93] explained how the water mechanically diffused into the glass surface. As the abrasive particle moves across the surface, a compressive stress field develops in front of the particle, while a tensile stress field develops behind the particle and the diffusion of water into the glass increases exponentially with tensile strain.

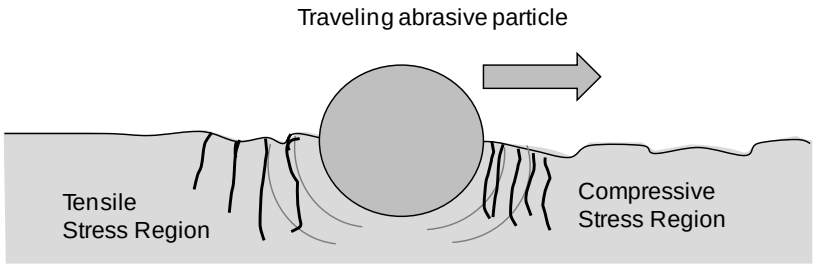

Figure 2-13: Nogami's model, water diffusion by tensile and compressive stress around a traveling abrasive [93, 53].

In chemical-mechanical theory the polishing rate is dependent on the slurry pH. M. J. Cumbo [31, 98] performed numerous polishing tests on different glasses using different polishing agents. Test outcomes suggested that the polishing rate moderately

depends on slurry pH. He found that for CeO_2 mixed with water, pH = 7 resulted in maximum removal rates.

2.4 Vibrations in Lapping and Polishing Processes

The sensitivity of pitch polishing process outcomes to process vibrations has not received much attention, although the importance of vibrations has been recognized in many other removal processes [155 - 167]. At best, for high quality finishes Leistner [108] recommended that the machine (using a Teflon lap) has to run very slowly, so as to generate minimum vibrations. No details on threshold vibration levels are available for pitch polishing operations. When vibrations have been considered in polishing they focused mostly on vibrations induced by external sources, i.e. high frequency (>20 kHz) ultrasonic-vibration assisted polishing. In ultrasonic assisted polishing the vibrational frequencies are above 20 kHz and the amplitude of the vibrations are in the range of 1 µm to 40 µm [126-135]. The noisy vibration in ultrasonic polishing machine can be heard (some frequencies are below 20 kHz) or felt by touching the machine parts, while on a typical, smooth running polishing machine the process vibrations are harder to hear and more difficult to. It is worth noting that the human's ability to feel vibrations is limited to particular bandwidths. Robotic scientist Masashi Konyo's [154] simulation determined the human detection thresholds for up to 1 kHz, see Figure 2-14.

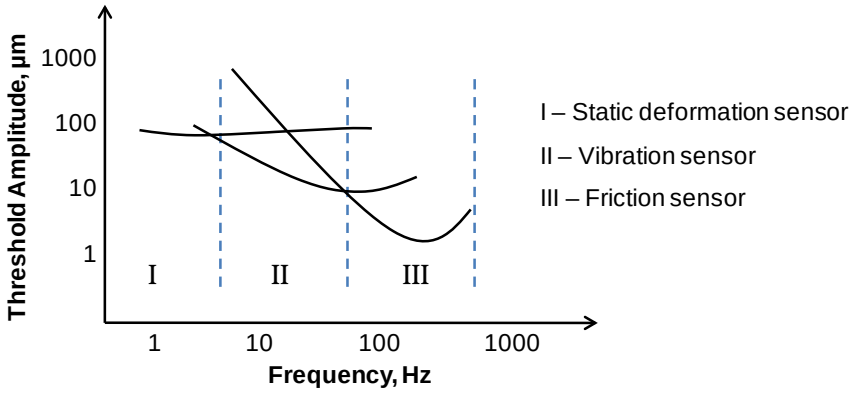

Figure 2-14: Thresholds amplitudes of human detection level [154].

As there is little data available regarding vibrations in pitch polishing processes, the literature outlined in this section considers the consequences of vibrations in polishing process other than pitch polishing. Table 2-5 lists the vibrational frequency and amplitude ranges along with tool and workpiece information found in the literature for different polishing processes. Considering the vibration analysis conducted for other removal process should facilitate a better understanding of the possible impacts of process vibrations in pitch polishing processes.

Table 2-5: Range of frequency and amplitude of vibration in different abrasive polishing process that considered impact of vibration.

Reference	Tool	Workpiece	Slurry	Frequency (kHz)	Amplitude (μm)
H. Shan [109]	Polishing pad	Nd-doped Metaphosph-ate Glasses	Simulated particles	~0.002	0 - 400
S. Yin [110]	Magnetic pole	Brass, Stainless Steel	80 μm dry magnetic abrasive	0.006	1000 - 3000
E. Brinksmeier [111]	Synthetic Felt	Hardened Steel	1 μm diamond	0.05-0.15	±150
W. Lin et al. [113]	Phenol	Die Steel HPM75	4 μm WA diamond slurry	0.5	100
F. Jung [114]	Felt polishing Ball	Stainless Steel	0.5 μm Al_2O_3	0.8	80
S.K. Chee [115-117]	Polyurethane or Nylon, sub aperture	Titanium Alloy	0.5 μm diamond	0.9	80
J. Guo [118, 119]	polyurethane tool with a radius of curvature 1 mm	Tungsten Carbide	0.25 μm diamond	9.2	30
Y. Li [120 - 123]	Resin Matrix Pellets	Fused Silica	Dry CeO_2	15.3	1
M. P. Mandina [124]	Pad/Fabric coated with pitch	Silica glass	0.05-10 μm CeO_2	0.25-50	±1.5 mm
N. Kobayashi [125]	Composite polymeric pad	Silicon Wafer	0.12 μm silica	21.9	- -
H. Suzuki [126]	Polyurethane, sub-aperture	Tungsten Carbide	0.5 μm diamond	22.4-28.9	30-40
H. Wang [127]	Spherical head	K9 Optical Glass	CeO_2	20	- -

Table 2-5(continued)

W. Xu [128, 129, 134]	Polyurethane Pad	Sapphire Wafer	80 nm Silica abrasive	20	± 4.5
M. Y. Tsai [131]	Polyurethane Pad	Copper Substrate	Aluminum Oxide, C7092	20	5-15
H. Suzuki [132]	Polyurethane	Tungsten Carbide	0.5 µm Diamond	25	10
U. S. Kim [133]	Electrode	Stainless Steel	H_2SO_4 and H_3PO_4 mixed with water	28	- -
J. Xu [136]	No tool used, abrasive vibrates around the fiber	Fiber MPO Connector	3 µm Diamond	20	- -
G. Amza [141]	Steel	Optical Glass	80 µm SiC	21.9-35.7	10
Y.S. Liao [142]	Carbon Steel Horn	Silicon Carbide	1 µm Fe_2O_3	20-34	- -
H. Hocheng [143]	Steel Rod	Mold Steel	8-150 µm SiC	25.6	35 - 60
M. T. Cuberes [144]	Rectangular Si Cantilever (AFM tip).	Highly Oriented Pyrolitic Graphite (HOPG)		1.5-2.15 MHz	
A.R. Jones [146]	End face tool with non-contact flow polishing	Aluminum	Boron Carbide F120-F600	40	4.5
Z. G. Huang [147]	Flow polishing	Silicon Carbide	0.05-0.5 µm Simulated particles	44 kHz	- -

Most of the literature listed above assessed the impact of vibrations on material removal rate and surface finish, two major outcomes of interest when considering polishing processes. The main findings are briefly highlighted below.

2.4.1 Impact of Vibration on Removal Rates

As polishing is a time intensive process, all process parameters and consumables must be optimized to enhance the material removal rates. Addition of external vibrations (into the tool or workpiece) is one such way to enhance the removal rate. In the vibration assisted polishing literature, listed in Table 2-5 [128-147], the basic mechanisms identified as promoting material removal rates include: enhanced mechanical abrasive-workpiece indentation, local micro-pumping, breaking-up of agglomerated particles, tool surface re-dressing, cavitation erosion, and weakening of the binding force of the ions.

Y. Li et al. [120 -123] polished fused silica samples using a fixed abrasive (CeO_2) pellet (sub-aperture)in both the presence and absence of ultrasonic vibrations. The results showed that ultrasonic vibrations can result in an increased material removal rate while maintaining comparable surface roughness to that obtained in conventional, non-vibrational assisted polishing. They proposed a mathematical model [120] that dealt with the indentation of abrasive particles into the workpiece. They found the indentation significantly increased due to the ultrasonic vibrations which resulted higher removal rate. According to the model the removal rate can be increased by a factor of two by increasing vibrational amplitude in vertical direction while the horizontal vibrations contribute little to the overall removal rate. S. Yin [110] found that vibrations from vertical direction generate a pulsating pressure on the workpiece, and that vibrations in horizontal direction promote cross-cutting effects, stirring action and increase relative

motion of abrasive particles. Wenhu Xu et al. [128, 129] polished a sapphire workpiece using Al_2O_3abrasives. He also induced ultrasonic vibrations in a vertical direction and found that the removal rate also doubled. The schematic of his polishing system is given in Figure 2-15.

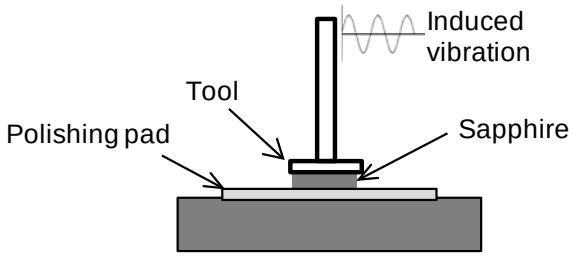

Figure 2-15: Schematic of Wenhu Xu polishing system.

N. Kobayashi [125] polished silicon wafers using a silica abrasive under ultrasonic vibrational conditions. He proposed that abrasive particles under ultrasonic vibration conditions impact the work piece surface with extremely high accelerations and that the vibrating abrasives create localized slurry pumping action. The pumping action prevents the agglomeration of micro-particles and the impact load allows abrasive particles to penetrate more easily into the polishing zone, both contribute to the higher removal rate.

M. P. Mandina [124] developed a polishing apparatus that utilizes ultrasonic vibration for rapid removal rate, see Figure 2-16. He observed that in conventional polishing the smaller particles tend to aggregate into bigger particles while during vibrational assisted polishing the vibrations help to prevent particle agglomeration, which is preferable for better polishing. Vibrations are also thought to assist in tool cleaning, conditioning/dressing thus promoting higher removal rates [124].G. Amza et al. [141] used finite element analysis techniques to study the effects of ultrasonic finishing process

on optical devices. According to his analysis, ultrasonic vibrations enable slippery contact (low friction) between the tool and the abrasives, this is thought to enable rolling contact between the abrasives and the workpiece providing enhanced removal rates. Huang et al. [147] applied molecular dynamics method to study the interaction between the abrasive particles under ultrasonic vibrations and a silicon carbide workpiece. Both the simulation and experimental investigations suggested that the particles vibrate and roll viscously on the substrate. The cyclic loading of the rolling particles induce compressive stresses in the substrate promoting brittle fracture.

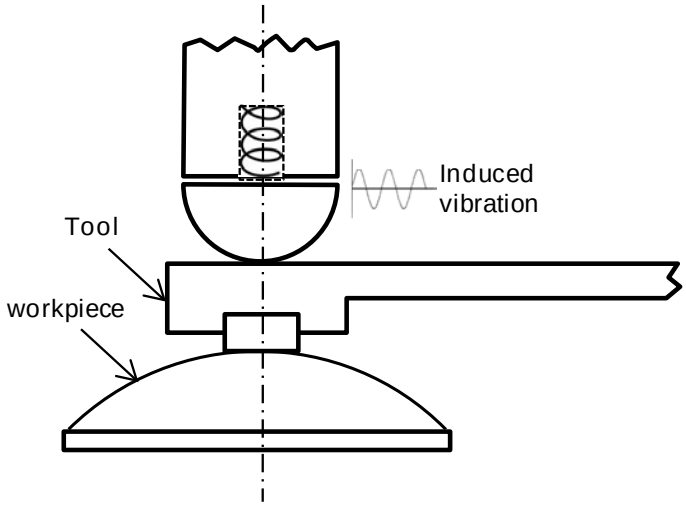

Figure 2-16: Schematic of one of the test configurations used in Mandina's patent [124]

A. R. Jones's [146] study on ultrasonic flow polishing used boron carbide abrasives on an aluminum workpiece. By analyzing the surface after polishing he realized that in the ultrasonic process the work piece material is removed by high frequency hammering of abrasive particles into the surface. However he also commented that more research is necessary to identify the optimum gap between tool and workpiece (i.e. vibration amplitude) for optimal hammering action.

W. J. Tomlinson et al. [137] examined the role of cavitation erosion when using aluminum oxide abrasives mixed with distilled water. Cavitation-erosion is a particular form of erosion caused by the implosion of bubbles on a workpiece surface [138, 139]. The bubble formation is often associated with sudden variations in pressure related to the hydrodynamic parameters of the fluid. Tomlinson results show that the linear erosion rates could be up to 10% of total removal (at 50μm peak to peak vibration amplitude with a frequency of 20 kHz).M. Y. Tsai [131] commented that ultrasonic vibration assisted polishing can enhance chemical action due to cavitation erosion.

R. Shen [140] explained the impact of ultrasonic vibration on the binding force of the ions. Ultrasonic vibrations transport energy between ions which weakens the binding forces and thus the ions can break away from the surface easily.

2.4.2 Impact of vibration on Surface Finish

Surface finishes are compellingly related to the vibration frequency and the relative speed between tool and workpiece. Y. Li et al. [120] performed both simulations and experiments (fused silica polished with CeO2) in both the presence and absence of ultrasonic vibrations. In presence of vibrations they found periodic structures on the machined surface, while no periodic scratches were observed after polishing without vibrations. This implies that the structure was induced by the externally induced vibrations. Their analysis indicated that the spatial wavelength of the periodic structures were regulated by the frequency of the induced vibrations and the relative velocity between the workpiece and the tool.

Vibration assisted processes have also been shown to induce mid-spatial frequency (MSF) errors [29, 153] on the finished surface. However these errors can be

reduced by giving careful consideration to the tool motion. The fast, high material removal VIBE^{TM} finishing introduced by M. P. Mandina [124, 149, 150] incorporated a short stroke, high-frequency random vibratory motion that can eliminate these MSF errors [26]. Chee [116, 117] utilized two a directional, low frequency vibration (2DLFV) assisted polishing system to reduce MSF surface error. Suzuki [132] and Liang [151] also observed vibration induced lateral tool marks and proposed two-axis vibration polishing that reduces the tool marks and improves the surface roughness.

2.5 Vibrations in Grinding Processes

While grinding is a higher material removal process than polishing, and its removal mechanism is predominately mechanical in nature (brittle fracture), is it still worth evaluating how vibrations affect the grinding process outcomes and considering if the information can be applied to the pitch polishing processes

It is no surprise that both externally induced and machine generated process vibrations have a significant impact on grinding outcomes [155-165]. Table 2-6 lists the range of vibrational frequencies and amplitudes reported in the grinding literature. Vibrations are considered to affect the removal rates and finishes by the following mechanisms; inducing reductions in the grinding force, promoting wheel dressing, reduction in process temperatures and altering the abrasive–workpiece contact mode (continuous to discontinuous contact).

Table 2-6: Range of frequency and amplitude in vibration assisted grinding process.

Reference	Workpiece	Grinding Wheel	Frequency (kHz)	Amplitude (μm)
J. Akbari et al. [160]	Al_2O_3 Ceramic	Diamond	17.5 - 28	2.5
Y. Wu et al. [161]	Fine-crystalline ZrO_2 Ceramics	Diamond	20	12
J. kim [155]	Sintered carbide	SD12000N100M	0.01 - 0.06	0.5 - 10
M. Alfares et al. [158]	Steel, Molybdenum, Niobium, Titanium	Silicon carbide	0.5 - 1.5	30 - 150
P. Chen et al. [159]	Mild Steel	Carborundum	0 - 3	7.5

J. Akbari et al. [160] studied ultrasonic vibration effects on the grinding process by utilizing finite-element (FE) analysis and he found that the machining rate increases with increases in the vibrational amplitude. The FE analysis showed that vibrations could reduce the grinding force up to 22% with 8% improvements in surface roughness. Vibrations are thought to promote further indentation of the abrasives into workpiece surface, causing more brittle fracture and thereby reducing the grinding force. He also thought that the vibrations enhance the self-sharpening action of the grinding wheel, i.e. self-dressing.

Y. Wu et al. [161] determined that the presence of ultrasonic vibrations in grinding promoted ductile mode abrasive-workpiece interactions. Due to the oscillations discontinuous contact between the workpiece and abrasive reduces both the grinding force and temperature. This results in improvements (factor of 2 improvements) in the grinding efficiency. In conventional grinding higher depths of removal typically re-higher surface roughness values, in contrast, during vibration assisted grinding the discontinuous contacts alters the chip formation mechanism and reduces the roughness while producing

higher removal rates. G. Bi et al. [165] performed grinding tests on an axisymmetric lens and found that the interference between the grinding wheel and the lens creates vibrations and that this interference vibration varies over the lens diameter. The vibrations at the center were lower than at the edge of the lens and that the surface quality was better in the regions of lower vibrations (i.e. better surface quality at the center of the lens than at the edge).

2.6 Conclusions

From the literature review it is clear that no paper is available in the public domain that considers the effect of process vibrations occurring during pitch polishing on process metrics. As listed in Table 2-5 and 2-6, researchers have considered the impact of vibrations in other finishing systems (CMP, vibration assisted abrasive polishing and grinding, etc.) where in most of the cases external vibrations (in the ultrasonic range) were imposed on the tool [126 - 135]. From the literature the vibrations are thought to affect the material removal and surface finish by the following mechanisms: enhanced mechanical abrasive-workpiece indentation, local micro-pumping, breaking-up of agglomerated particles, tool surface re-dressing, cavitation erosion, and weakening of the binding force of the ions.

It is reasonable to assume that the level (amplitude and frequency) of process vibration in pitch polishing machines will be lower than that in vibration assisted polishing systems (Figure 2-17), however as the material removal rates and surface roughness values are also lower than those produced by ultrasonic assisted processes the lower magnitude vibrations may still have an effect. This work will measure the level of

process vibrations occurring during pitch polishing and evaluate if they have any impact on material removal rates and surface finishes.

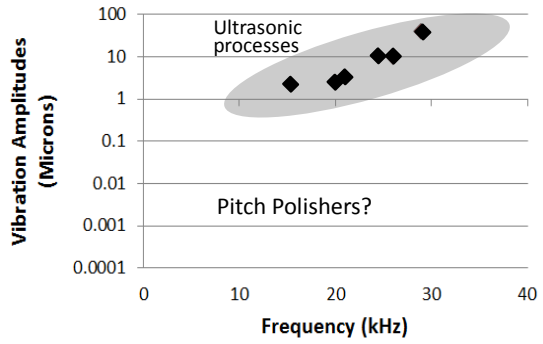

Figure 2-17 : Level of vibration in vibration assisted polishing process (see Table 2-5).

CHAPTER 3: DYNAMIC RESPONSE OF PITCH AND PITCH TOOLING

3.1 Introduction

Pitch is viscoelastic material and its dynamic behavior with respect to typical polishing vibrations is of interest, i.e. how does the pitch behave when subjected to process vibrations (up to 10 kHz). Are process vibrations amplified or attenuated when transmitted through the pitch? How do changes in pitch grade, type or tool geometry alter its response? Is it possible to completely attenuate the vibrational transmission? This chapter outlines both the procedures used to investigate the dynamic response of pitch and the main findings.

3.2 Frequency Sweep Test

The test involves using a signal generator to create a sine wave with continuously increasing frequency values (50 Hz-16 kHz) and using this varied output to drive a shaker table thus creating a vibrational input that varies across the frequency bandwidth over time (typically few second). The test is performed by transmitting the vibration from the shaker table to a pitch sample attached to the aforementioned. Two accelerometers, one attached to the bottom and other attached to the top of the pitch sample record the vibrations entering (Y) and exiting (X) the sample. The X/Y ratio describes how the output vibration magnitude varies to that entering the sample. X/Y values greater than one implies vibration amplification occurs, while values less than one implies attenuation takes place.

3.2.1 Experimental Setup and Test Procedure

The test setup consists of a shaker table (BK Vibration Exciter Type 4809) driven by a HP35639A dynamic signal analyzer (DSA) and a BK power amplifier (Type 2706). Two PCB accelerometers (352B10) that operate up 17 kHz record the system's vibrational input and output. The shaker table can vibrate up to 20 kHz with a maximum displacement of 8 mm, and it has first axial resonance at 20 kHz [174] which is out of the accelerometer range. The pitch sample under investigation is screwed onto the shaker table. The vibrations entering and exiting the sample are monitored by the two accelerometers (A1 and A2). See Figure 3-1 for a schematic of the set-up, Figure 3-2 illustrates photos of the shaker table and mounted sample.

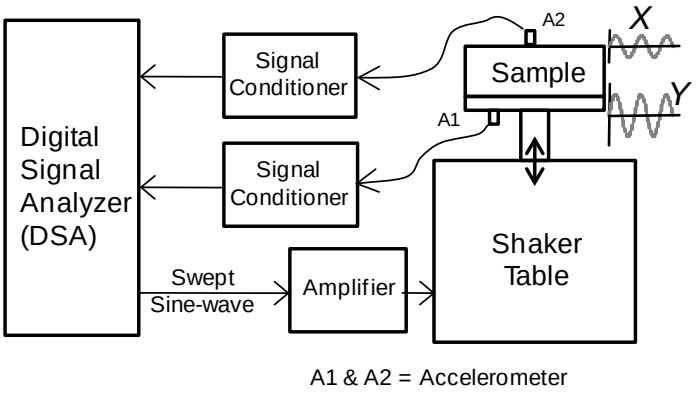

Figure 3-1: Block diagram of the test setup.

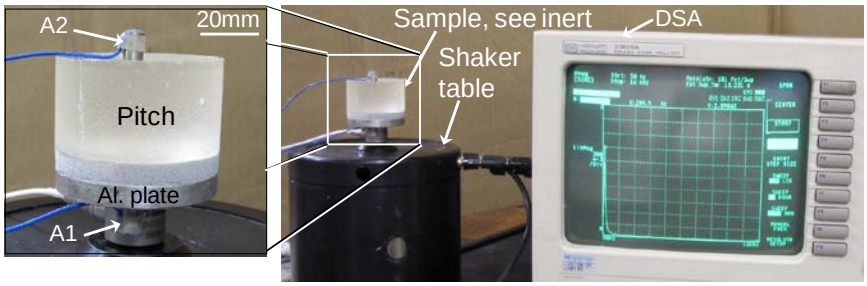

Figure 3-2: Close up of sample mounted on shaker table.

During testing the samples were subjected to a swept sine wave input (50 Hz to 16 kHz). Step increments were 39.875 Hz. Typical vibrational amplitudes range from 50 µm at 50 Hz to less than 1 nm above 10 kHz. The accelerometer marked ‘A1’ in Figure 3-2captures the values of Y, while accelerometer ‘A2’ captures the values of X. The ratio (X/Y) is plotted versus the input frequency. The initial focus is to determine if pitch grade (hardness) and type (natural or synthetic) have a significant impact on the vibrational transmission.

3.2.2 Vibrational transmission through Pitch and Pitch Tooling

Two pitch grades (hard and soft), and two pitch types (synthetic and natural) were evaluated. The geometry of the sample was also considered.

3.2.2.1 Sample preparation

Typically the pitch samples were generated by first heating the pitch over a water bath and then pouring a defined mass of pitch into silicon molds (diameter ≈ 50 mm) which contained 6mm thick aluminum base plates. All samples were allowed to cool for at least 24 hours before any testing took place. All samples were stored and tested in the temperature controlled lab with temperature range 21 °C ± 1 °C. Figure 3-3 depicts some sample tools.

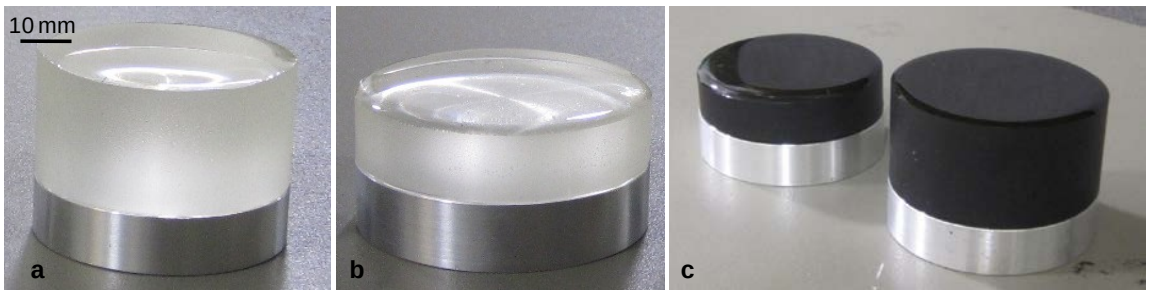

Figure 3-3: Sample tools (Ø = 50 mm) a. thick pitch, b. Thin pitch;
Pitch type: synthetic in a. & b., and natural in c.

Table 3-1 summarizes the properties of selected pitches and Table 3-2 describes the different samples tested. Two types of pitch are considered, Gugolz™, a natural pitch extracted from tree resin, and Acculap™, a synthetic polymer based pitch. Two different hardness grades are examined, Acculap™Soft (Asoft) and Gugolz55 (Gsoft) are soft pitch grades while Acculap™VeryFirm (Avf) and Gugolz73 (Gvf) are the harder pitch grades. These two grades have hardness values representing the lower and higher end respectively of commonly used pitches. The sensitivity of the results to the pitch layer thickness is also evaluated, this is achieved by doubling the mass of pitch used; 50 g of pitch produces a 22 mm thick layer, while 25 g produces an 11 mm thick sample.

Table 3-1: Material properties of the pitches that used in the test [7, 56].

Pitch Grade	Shore D Hardness	Approximate Shear Viscosity(GPa-s)	Natural Frequency, kHz
Acculap™Soft	60	0.1	7.3
Gugolz 55			5.7
Acculap™VeryFirm	80	8	8
Gugolz 73			6.4

Table 3-2: samples that used to evaluate the impact of pitch type and grade.

Sample Name (Ø = 50 mm)	Pitch Grade	Pitch Type: Synthetic: Acculap Natural: Gugolz	Pitch Layer Thickness
Asoft_22mm	Acculap Soft	Synthetic	Thick pitch layer = 22 mm (50 g weight)
Avf _22mm	AcculapVery Firm		
Gsoft _22mm	Gugolz 55	Natural	
Gvf _22mm	Gugolz 73		
Asoft_11mm	Acculap Soft	Synthetic	Thin pitch layer = 11 mm (25 g weight)
Avf_11mm	Acculap Very Firm		
Gsoft_11mm	Gugolz 55	Natural	
Gvf_11mm	Gugolz 73		

3.2.2.2 Test Results and Analysis

Initially a frequency sweep tests was performed on one of the aluminum base plates that had no pitch adhered to its surface. The response curve is presented in Figure 3-4, where the spikes at 7.8, 12.3, 12.8 and 14.7 kHz are assumed as the resonances of the test setup.

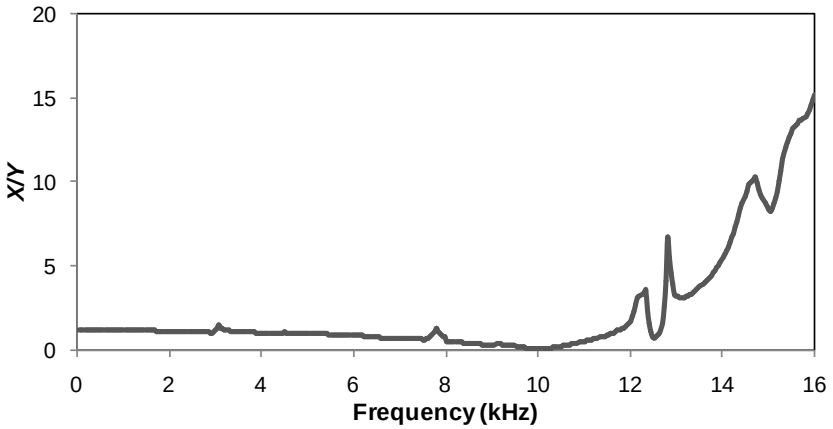

Figure 3-4 : Sample-platen response to swept sine wave.

Impact of pitch grade (soft versus hard pitch):

A total of twelve, 22mm thick pitch samples were tested. Six were composed of natural pitch (3 hard, 3 soft), and six used synthetic pitch (3 hard, 3 soft). The test results for all the samples are plotted in Appendix A. For simplification, only two typical response curves for the synthetic (Acculap) pitch grades are presented in Figure 3-5where the black and gray lines represent the Acculap soft and Acculap hard pitches respectively. From the response curves it is clear that up to 6 kHz both hard and soft pitches transmitted vibration in similar fashion with no attenuation but somewhat amplification (less than 2×). The spike at 8 kHz is due to system resonance [64]. Two synthetic pitch grades with similar tool geometry generated resonances at two distinctly different frequencies and the resonance peak for softer grade occurs at a lower frequency, but is

larger in magnitude than that obtained with this harder pitch (comparing three sets of test, see Appendix A for more results). This is reasonable as it is mentioned in the literature that the harder pitch has higher natural frequency and lower damping ratio, and is more resistant to deformation [7].

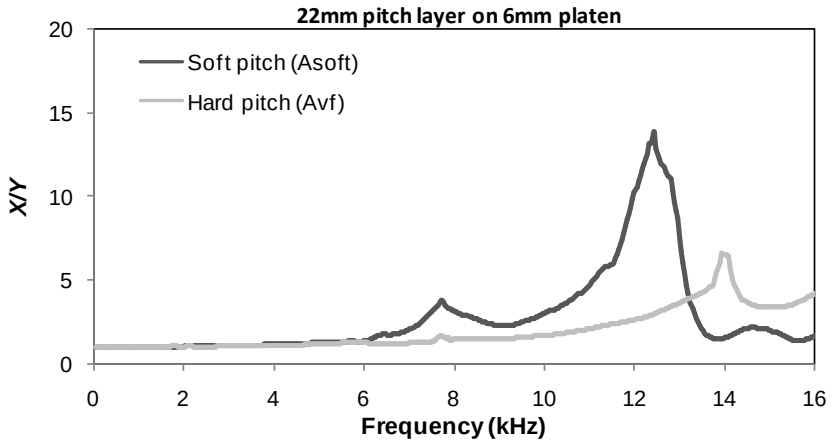

Figure 3-5: Vibration transmission in different pitch grades (hardness).

Impact of pitch types (natural versus synthetic pitch):

Figure 3-6(a) and (b) illustrate how different types of pitch, i.e. natural or synthetic, with the same hardness levels have differing responses to the vibrational input. Different pitch series with similar hardness has different dynamic stiffness [7]. That's why similar to that reported in section 2.3.3 of the lit review, each type of pitch has its own resonance characteristics.

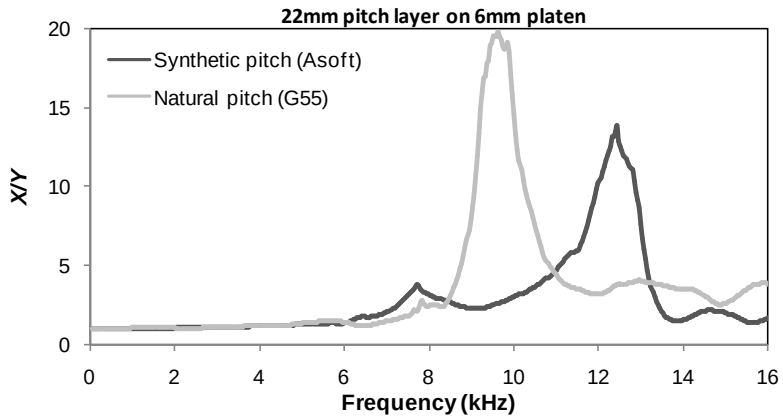

(a)

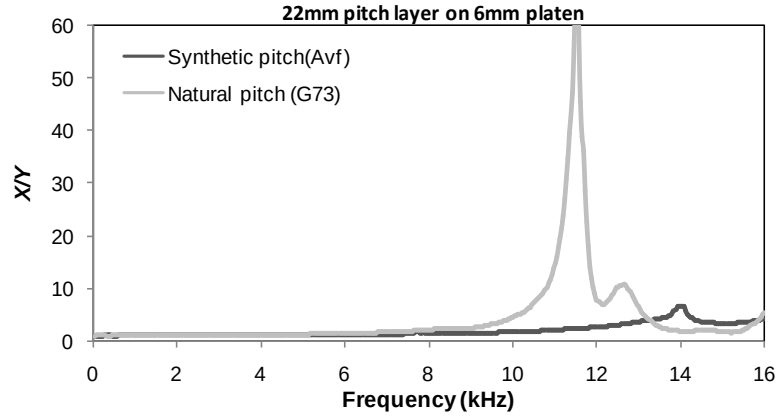

(b)

Figure 3-6:Impacts of pitch type, (a) soft grade, (b) hard grade; see Appendix A for more detail test results.

Impact of pitch geometry (thick versus thin pitch layer):

Additional tests were performed to evaluate the role of pitch thickness on the vibrational response. Two pitch layer thicknesses, 22 mm and 11 mm, are considered and the results are presented in Figure 3-7.When a thin layer of pitch is on the base plate, the response is quite different from that obtained with the thicker pitch layer. The response with the thinner pitch layer is very similar to the response obtained when testing with the aluminum base plate alone (Figure 3-4). The dynamic response of tool depends on its

stiffness [7] and the thicker pitch layer reduces the stiffness more than a thinner layer. This suggests that the dynamic response of polishing tools will be affected by both platen and pitch geometrical contributions

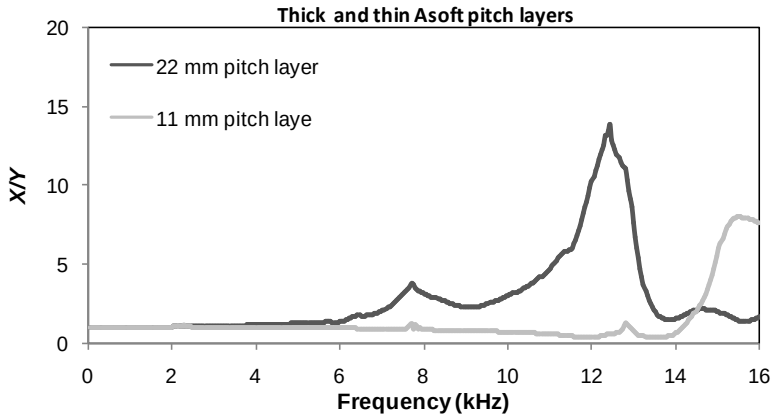

Figure 3-7: Impacts of pitch layer thickness.

3.3 Vibration Attenuation through Passive Damping Materials

This section determines if passive damping materials can be utilized in the tool construction to attenuate process vibrations. Nine different damping materials that are commercially available in the market are evaluated using the same frequency sweep test outlined above. The following sections provide more details about the damping materials, the experimental set up, and the test results.

3.3.1 Sample Preparation

The materials evaluated include: vinyl, gum, neoprene, viton, polyurethane, nitrile (Buna N), rubber, cork, and lead. Two different sample configurations are tested. The first configuration, Type-A, identifies the damping quality of different passive damping materials. It consists of the passive damping material adhered to an aluminum platen (6 mm thick and 50 mm in diameter), see Figure 3-8a. The second configuration, Type-B,

consists of Type-A samples with 50g of pitch poured on the damping material, see Figure 3-8b.

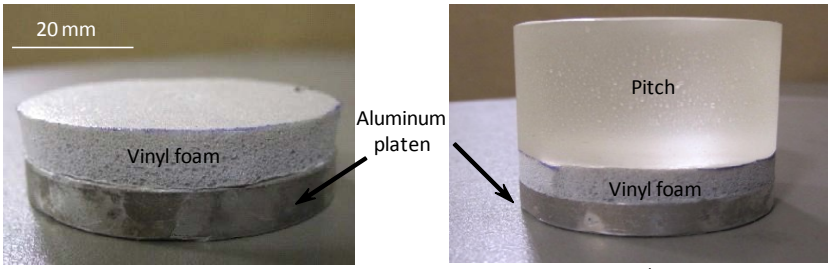

Figure 3-8:a. Type-A, and b. Type –B Sample.

Some of Type-A samples are listed in Table 3-3. While more materials than listed in Table were tested, the preliminary testing eliminated them from full testing. A parameter termed as Inverse Quality Factor, Q^{-1} [106] is used to identify the damping quality of different materials. Higher Q^{-1} value means higher damping ability. Appendix describes the method to quantify the Q^{-1} value.

Table 3-3: Evaluated Type-A samples.

Name	Damping material
A1	3.18 mm Vinyl Extra Soft
A2	3.18 mm Vinyl Soft
A3	3.18 mm Gum Extra Soft
A4	3.18 mm Cork
A5	3.18 mm Viton Extra Soft

3.3.1.1 Results and Analysis

In most cases multiple samples of each material were evaluated. Each curve in the graphs represents a samples' typical response. Samples were evaluated with respect to

the Q^{-1} factor, maximum vibration amplification, and the frequency at which X/Y< 0.5 (50% attenuation).

Figure 3-9depicts the response curves for samples A1 to A5. Calculation of the Q^{-1} factor from the experimental data revealed that sample A1 (Vinyl Extra Soft) has the highest Q^{-1} value (1.45), and 50% attenuation was attained at the lowest input frequency (540 Hz). While the Q^{-1} value for A2 (Vinyl Soft) was not as high (0.52), it did provide 50% attenuation at a similar frequency to A1 and from an application point of view A2 is preferred over A1 as it is considered more mechanically robust and not as compressive as A1.The robustness is very important so as to withstand the cyclic loading and unloading that will occur during an actual polishing process and thus the cork sample (A4), the most robust material among the tested sample, has higher interest. Though the Q^{-1} value for A4 (cork) is not as high (0.49) as vinyl foam, and the 50% attenuation occurs at 4 kHz, it damped out all the higher frequency (> 8 kHz) vibrations as plotted in Figure 3-6. The amplitude of resonance peak for A4 is also comparable to A2.

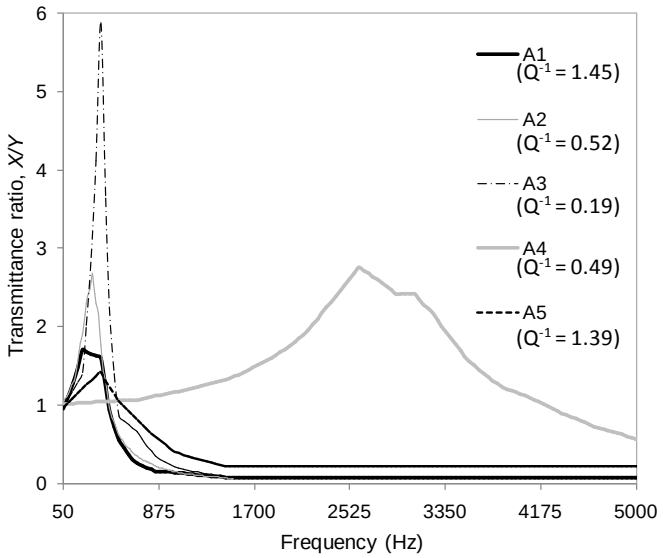

Figure 3-9: Vibrational transmission for different damping materials.

Sample A6 has a high Q^{-1} factor but is not considered further at this point for two reasons, firstly, 50% attenuation doesn't occur until 925 Hz and secondly, like Vinyl Extra Soft it is also considered too soft to withstand the cyclic polishing loading, i.e. the pitch layer will crack due to the lack of foundational support. Considering the robustness and evaluating other factors cork is used as a passive damper on an actual polishing tool, see chapter 4.

3.4 Impact Test: The Transient Response

The frequency swept tests detailed in section 3.2 evaluated vibrational transmission through sample tools and not an actual polishing tool as the latter are too heavy (16kg) to attach to the shaker table. To evaluate the dynamic response of an actual tool, impact tests were considered. An impact test measures the dynamic response of a system to transient vibrations. The measurement is accomplished in two steps. The system is excited by an impact force of known magnitude, and the system's response to the impact, i.e. the resulting vibrations sent through the sample, is measured by an accelerometer.

A mild-steel (MS) platen (Ø300 mm) and a pitch tool that made using the same platen are evaluated in this section. The pitch tool is prepared with a layer of soft synthetic pitch (22 mm) molded to the MS platen.

3.4.1 Impact Test: Evaluation of Tool Natural Frequency

The MetalMax test kit from Manufacturing Lab Inc. was used to conduct the impact testing. The accelerometer that used to measure the vibration operates in the 10 Hz to 10 kHz regime. The samples tested were on a foam bed to reduce the influence of any supporting structures during the impact test. Each sample was hit by a MetalMax

hammer (GK 3100) and the resulting vibrations were recorded by the accelerometer. Figure 3-10illustrates the pitch tool, the hammer hit site, accelerometer location. Figure 3-11presents a typical response. The red response curve is for hitting the MS platen, and the blue curve is for hitting the pitch tool that uses the same platen. The corresponding frequencies of the spikes (1, 2, 3 etc.) are the natural frequencies of the platen. Detailed of the test procedure and the measurement of the damping ratio are provided in the reference [61].

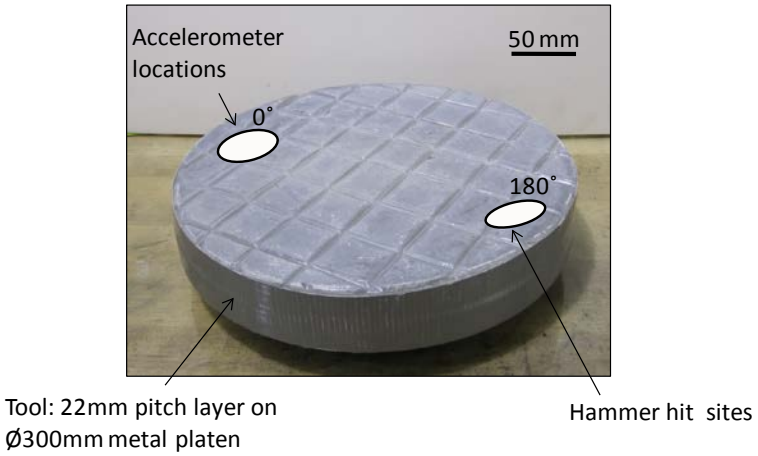

Figure 3-10: Pitch tool and accelerometer and hit locations.

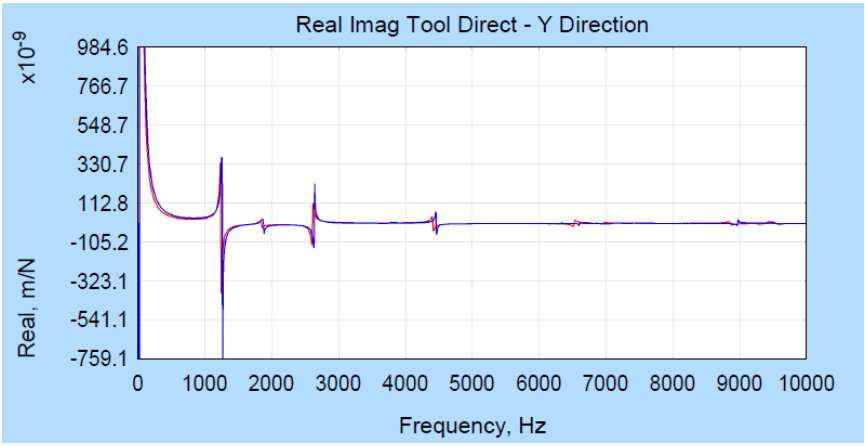

Figure 3-11: Test results (frequency response) for MS platen (blue) and the tool (red) made from MS platen.

3.4.2 Results and Analysis

The impact test results for MS platen and the pitch tool (pitch layer on MS platen) are presented in Table 3-4 (See Appendix A for detail).

Table 3-4: The resonance frequencies and spikes amplitudes for MS platen and pitch tool with MS platen.

MS Platen		MS Platen with Pitch	
MS Platen	MS Platen with Pitch	MS Platen	MS Platen with Pitch
Natural Frequency, Hz	Spikes Amplitude, nm	Natural Frequency, Hz	Spikes Amplitude, nm
1258	890	1258	890
1872	65	1872	65
2635	413	2635	413
4459	85	4459	85
6581	7	6581	7

The response of the polishing tool is dominated by the metal substrate, the pitch layer on platen slightly reduces the values of resonance frequency and reduces the corresponding peak values. Similar trend was observed in a previous test by Mullany [61] where a relatively thinner (10 mm) layer of pitch was applied. This is reasonable as because of applying pitch layer (1.8 kg) increased the overall total mass (m) and reduced the stiffness (k) and thereby reduced the natural frequency ($\omega_n = \sqrt{k/m}$).

3.5 Conclusions

The frequency sweep test results indicated that during polishing the machine process vibrations are transmitted through the pitch to the tool-workpiece interface without any attenuation. The tests demonstrated that the pitch type, grade and tool geometry can significantly affect the vibration transmission characteristics of small test

samples. Impact testing and frequency sweep tests also indicate that the metal substrates used in polishing tool fabrication will contribute more significantly to the dynamic characteristics of the finished tool than the choice of pitch used to coat the tool. The addition of additional damping material to the tool can effectively alter vibration transmittance. The damping material can damp out (transmittance ratio < 1) all the higher frequency (> 4 kHz) vibrations that amplified due to the pitch layer on the metal platen. Effect of damping material is further evaluated in chapter 4.

CHAPTER 4: POLISHING SYSTEM DYNAMICS AND POLISHING TEST

With the overall goal of determining if process vibrations have significant influence on polishing outcomes such as material removal rates and surface finish, the initial work focused on quantifying the amplitude and frequency content of vibrations generated by two typical over-arm polishing machines under typical operating conditions. Tests were conducted with different platens on two different polishing machines at two different platen speeds. Typical process vibrations were measured and the influence of platen, polishing parameters (platen speed), tool construction (damping materials) and the machine choices on the vibrations are presented. Numerous polishing tests are performed on two separate polishing machines under 'identical' polishing conditions and the resulting outcomes analyzed to understand the role of vibrations on polishing outcomes.

4.1 Quantifying Amplitude and Frequency Content

The vibration content (amplitude and frequency) associated with typical polishing processes were measured and evaluated in both the time and frequency domains. Tests were conducted with different tool constructions on two different polishing machines at different platen speeds. The amplitude and frequency content obtained on two different machines were compared and the differences are further analyzed for polishing test on both the machines.

4.1.1 Equipment

4.1.1.1 Strasbaugh Over-arm Polishing machine

Two machines evaluated in this work, both are Strasbaugh over-arm polishing machines (see Figure 4-1), and they are denoted as Machine 1 and Machine 2. Machine 1 is a Strasbaugh nFocus over-arm polishing machine featuring a variable speed drive and digital readouts for both the spindle rotation and the eccentric sweep. This machine has static and pneumatic features that allow for polishing pressure adjustment. Machine 2 is an older Strasbaugh polishing machine (model 6UR1) that has mechanical speed meter. The over-arm utilizes static loads to control the polishing pressure. Both machines can accommodate the same polishing tools. A separate pumping system is used to deliver polishing slurry to the tool.

Figure 4-1: Two Strasbaugh over-arm pitch polishing machines.

4.1.1.2 Polishing Tools and Tool Substrates

A pitch tool consists of a soft layer of pitch on a metal substrate called the platen. Platens are usually circular in shape, available in different diameters and thickness and in

different materials. Initially the influence of platen choice was evaluated. Three platens, each of similar geometry (diameter, Ø = 300 mm and thickness, T = 25 mm), but made from different materials, steel (ST), aluminum (AL), and cast iron (CI), were evaluated on the same machine while running at set speeds. Three pitch tools all using the same steel substrate, were also prepared. While details of how to fabricate pitch tools are provided in reference [70], two were made by pouring a 22 mm thick layer of Acculap™Soft pitch onto the steel substrate edged with a silicon band to contain pitch while it hardens, Tools A1 and A2. In the case of third, Tool B, a 6 mm thick layer of cork was adhered to the substrate prior to pouring a 22 mm thick layer of pitch. After pouring the pitch on the platen, the tool was placed on flat surface to allow the pitch layer to cool while keep the upper surface level. The pitch was allowed to cool overnight. After removing the silicon edging, the sharp edges of pitch layer were carefully chamfered to prevent further edge chipping. Substrate and tool names are presented in Table 4-1 and are illustrated in Figure 4-2. These tools were evaluated on both the machines.

Table 4-1: Platen and Tool notations and their approximate mass.

Platen		Mass (kg)
ST Platen	Steel platen	14.0
AL Platen	Aluminum platen	5.50
CI Platen	Cast-iron platen	15.0
Tool		
Tool A1 & A2	22 mm Acculap™Soft pitch on steel substrate	15.8
Tool B	6 mm cork in between Acculap™Soft pitch and steel substrate	16.0

Figure 4-2: a. Steel substrate (Ø=300 mm), and b. Tool A (22 mm pitch layer on steel substrate), c. Tool B (steel substrate, 6 mm cork layer and 22 mm of pitch).

4.1.2 Vibration Measurements and Analysis

4.1.2.1 Instrumentation

A PCB accelerometer (352B10) that operates up to 17 kHz is used to measure the vibration. The accelerometer is connected to a computer through a PCB signal conditioner (Model 482C), an analog to digital converter (ADC), and a National Instruments data acquisition card (DAQ card model 6036E). The location of the accelerometer on the polishing machine is illustrated in Figure 4-3(a). The schematic diagram of the instrumentation is given in Figure 4-3(b). The DAQ card has maximum sampling rate up to 200 kS/s. LabVIEW is use to record the accelerometer's response and to convert the recorded data from the time into the frequency domain producing a FT (Fourier Transform) plot. The LabVIEW diagram is presented in Figure 4-4. A typical measurement and the FT conversion are provided in Figure 4-5.

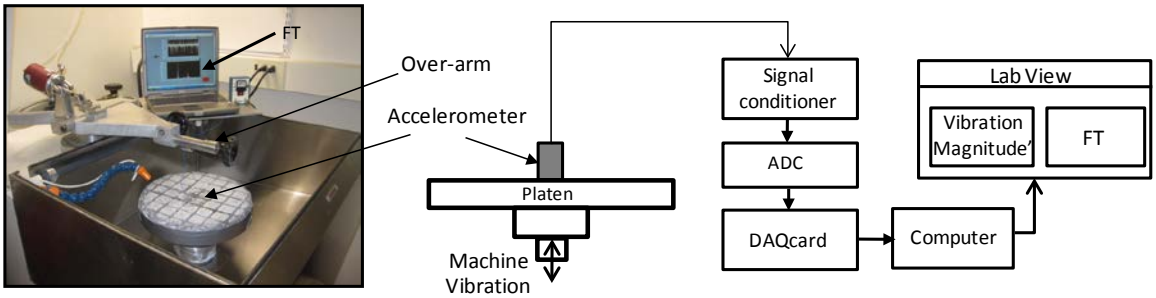

Figure 4-3: (a). An over-arm polishing machine, (b) Schematic of the instrumentation.

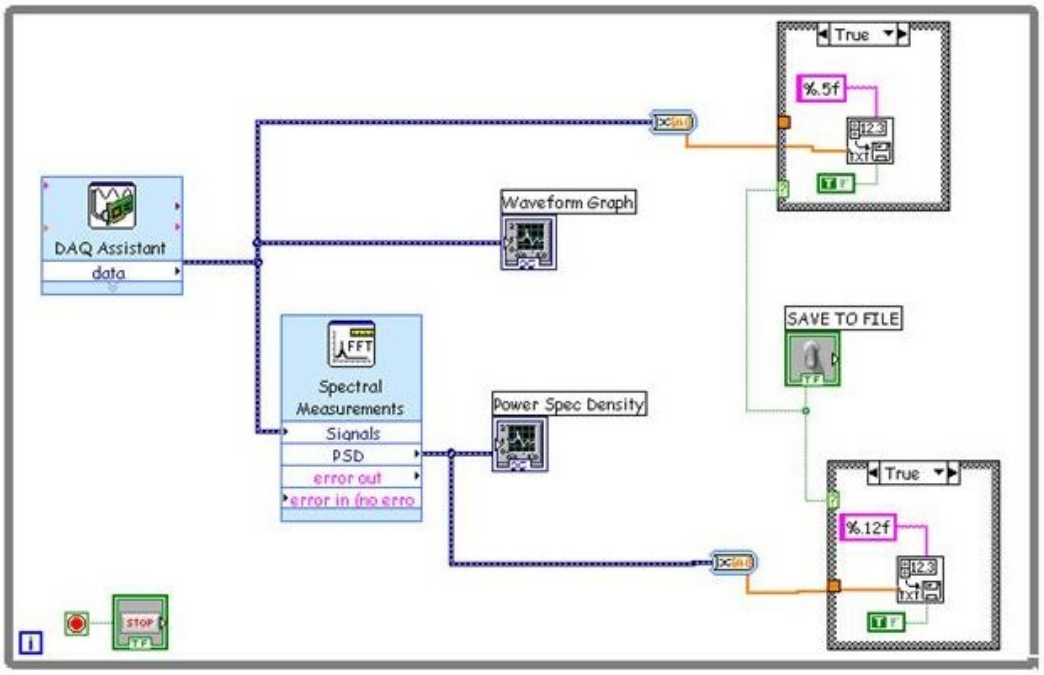

Figure 4-4: LabVIEW to process the accelerometer readings.

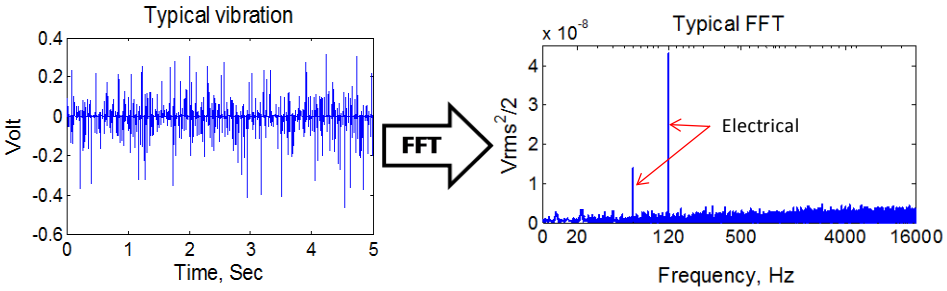

(a) (b)

Figure 4-5: (a) A typical process vibrations resulted with a PCB accelerometer, (b) LabVIEW generated Fourier transform (FT plot).

4.1.2.2 Vibration measurements

The measurement of machine vibrations was performed at the same time of day, i.e. when the workshop was quiet. Prior to assessing polishing vibrations, two initial sets of measurements were performed, (1) the accelerometer was attached to the polishing room floor to quantify background/building vibrations, and (2) the accelerometer is

attached to the machine spindle with the power switch turned on, but the platen not rotating. These tests were done to evaluate the vibrational response due to background environment. That said, the environmental vibrations are not significant. The only notable spikes were at 60 Hz, this one undoubtedly related to electrical noise.

As stated in section 4.1.1.2 the three different platens were tested on Machine 1, and the three different pitch tools were tested on both Machine 1 and 2. To investigate the influence of machine parameters on vibrations two platen speeds were investigated, 10 rpm and 20 rpm, while the over-arm was kept constant at 5 rpm. The accelerometer was placed on the center of the platen. The sampling rate was 100 kHz, and each test lasted five seconds.

4.1.3 Results Analysis

The vibrational characteristics obtained with different platens, tool constructions, and process speeds are presented and analyzed. In each case the vibrational signals were measured for more than once, however in the figures the FT plots represent only one typical measurement.

4.1.3.1 Platen Type: AL vs CI vs ST

Figure 4-6 provides sample FTs for the three platens running at 10 rpm on Machine 1. The peaks indicate the dominant frequency in the recorded vibrations. All the platens generated dominant peaks at approximately 53 Hz, harmonics are presents at 106 Hz for the AL platen. The peaks at 60 Hz, and subsequent integer multiples of it (120, 180 and so on), are undoubtedly related to electrical noise. Figure 4-6demonstrated that the vibrational responses recorded when using different platens do not significantly differ from each other.

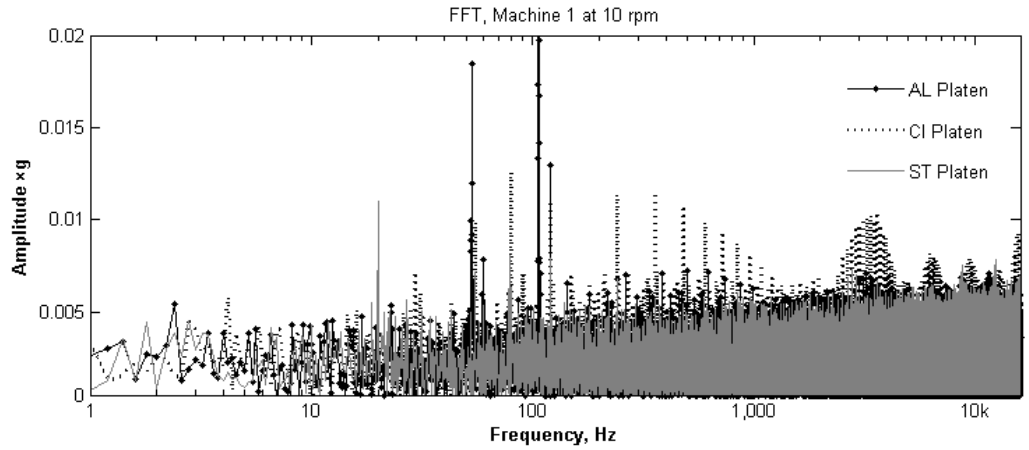

Figure 4-6: FTs of vibrations for three different platens at 10 rpm (g = 9.81 m/s^2, AL-> aluminum, CI-> cast iron, and ST-> Steel).

4.1.3.2 Pitch Tooling

Figure 4-7 illustrates the FTs of vibrational data obtained for a steel platen and the same steel platen coated with a 22 mm thick layer of pitch. The pitch layer did not significantly attenuate the vibrational transmission over the frequency bandwidth, though minor attenuation (≈ 5%) observed in higher frequency range. The transmission characteristics also support the previous sample test in Chapter 3 where pitch layer provided no attenuation over a wide range of frequencies.

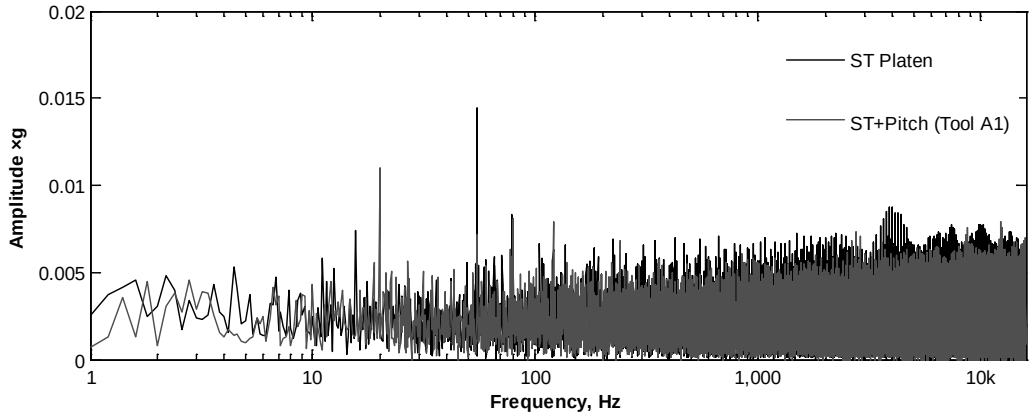

Figure 4-7: FTs of vibrations for a steel platen and pitch tools from the same platen.

Figure 4-8 compares the responses obtained when using Tools A1 and Tool B on Machine 1. Tool B has a 6 mm layer of cork between the pitch and the platen. As expected, Tool B attenuates the higher frequency vibrations up to 40%.

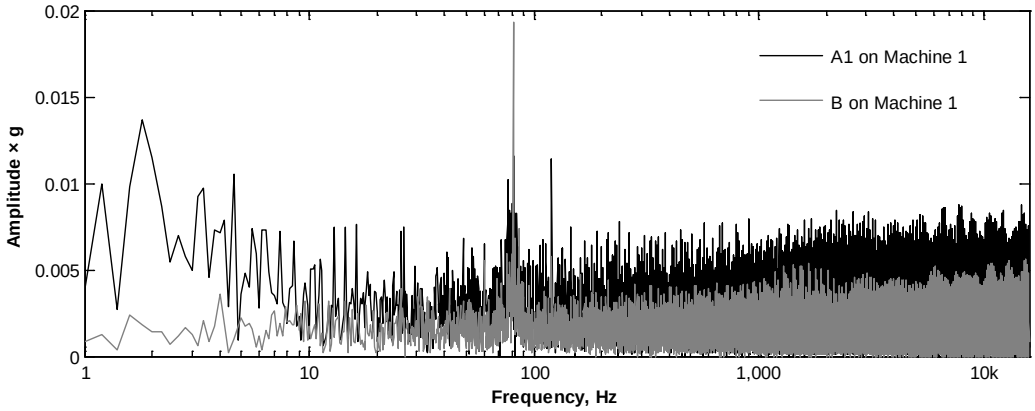

Figure 4-8: Tool B damped out the vibrational transmission.

4.1.3.3 Machine Parameter (platen speed)

Figure 4-9illustrated the vibration FTs obtained while operating at two speeds on Machine 1, 10rpm and 20rpm. At 20 rpm the response is dominated by vibration at 80 Hz while the dominant frequency while operating at 10 rpm is approximately at 55 Hz. Across all frequencies the response of the system when running at 10 rpm are lower in magnitude than when running at 20 rpm. That says the same machine running with different speeds can have different dynamic characteristics.

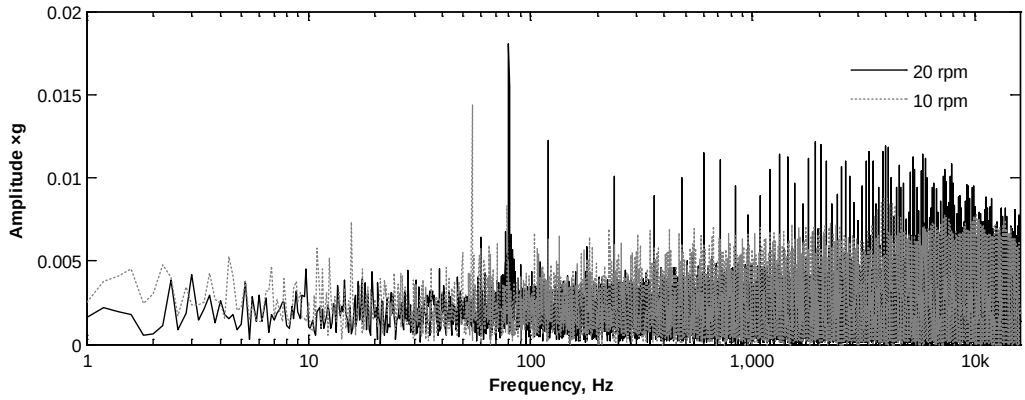

Figure 4-9: FTs for the pitch tool (ST + Pitch) platen at two speeds (log scale in x axis).

4.1.3.4 Different Polishing Machines

Two different Strasbaugh™ over-arm polishing machines, mentioned previously as Machine 1 and Machine 2, were equipped with Tool A1. The operating conditions were kept consistent while the tool swapped over between the machines (platen speed = 20 rpm and over-arm speed= 5rpm). It was recognised that these parameters may not provide the best polishing outcomes (removal and surface finish) however the main focus was to differentiate between the vibration signatures generated by the machines.

Figure 4-10 illustrates the FTs of measured vibrations obtained when Tool A1 was used on Machine 1 and Machine 2. The broken line on the graph depicts the frequency response of the Machine 1 when it is powered on but stationary, i.e. the base line accelerometer readings. Dividing the acceleration by square of corresponding frequency provides the associated displacement. Here the measured displacements are very small. For example, Machine 1 with Tool A1 has the displacements are on the order of 10 nm at lower frequencies (250 Hz) and are negligible (<1 Å) above 10 kHz. The diminutiveness of these magnitudes is even more noticeable when compared to the

vibrations in ultrasonic polishing. In ultrasonic polishing the typical vibrational amplitudes are in the range of several hundred nanometres up to 40 µm [126-135].

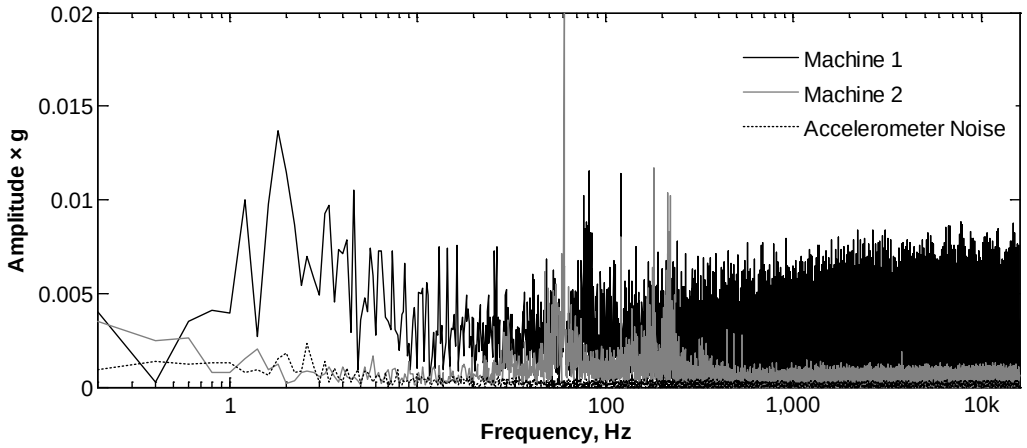

Figure 4-10: FT of the polishing vibrations for Machine 1 and Machine 2 with Tool A1 (g = 9.8 m/s^2, log in x axis).

In this test the difference in vibrations is of most interest, not the source of the differences. In Figure 4-10at higher frequencies (>500 Hz) the vibrational amplitudes are up to five times greater for Machine 1 than Machine 2, i.e. there is a significant difference in vibration signatures at higher frequencies between the two machines.

4.1.4 Vibration Quantification Summary

The previous test results (sections 4.1.3.1, 4.1.3.2 and 4.1.3.3) demonstrated that the machine running conditions and the tool construction can have an influence on the process vibrations. The presence of pitch on the platen slightly reduced (≈ 5%) the magnitude of variation. Further reduction in magnitude (≈ 30%) was obtained by using a cork layer in between pitch and platen. Different polishing machines operating under ‘identical’ conditions have significantly different vibrational characteristics. Process induced vibrations are in the nanometer range; this is far less than that in traditional ultrasonic polishing processes.

4.2 Polishing Tests

Fused silica samples were polished on both Machine 1 and 2 to evaluate the impact of process vibrations on pitch polishing outcomes. To analyze the polishing outcomes the following metrics were evaluated; material removal rate (MRR), surface finish (roughness), and sub-surface damage (SSD). The MRRs were evaluated by mass loss, the roughness values were measured using SWLI and AFM techniques, while chemical etching was used to evaluate the SSD. The details of tool, workpiece, slurry and polishing condition are presented in the following sections.

4.2.1 Pitch Tool

Before polishing the tools were conditioned and the final conditioned surfaces were evaluated using Talysurf profilometer and an AFM system.

4.2.1.1 Tool Preparation and Conditioning

Pitch tool requires conditioning to make it suitable for material removal. For better slurry circulation it is necessary to scribe grooves into the surface of the tool. Grooving also helps to removal polishing debris. Different possible grooving shapes are described in reference [11], while in this test a single sided razor blade was used to create “V” shape grooves. The grooves were approximately 5mm in depth and 20mm apart. Similar grooves were cut at right angles to first set making a square mesh pattern, as illustrated in Figure 4-12.

The slurry, 1 µm cerium oxide mixed with water (1:10) was used to condition the grooved tool. A magnetic stirrer continuously agitates the slurry to prevent the abrasive particles separating out from the water. A dummy glass workpiece (Ø = 200mm) is polished on the tool to embed the slurry particles into the pitch tool surface. The

embedded particles create a crust that makes it possible for the tool to remove material. More conditioning allows more particles to embed themselves thus providing higher removal rates. After conditioning for several hours the tool becomes saturated with ceria particles and the removal rate becomes consistent. To evaluate the saturation level of the crust, a number of polishing tests were performed after certain amount of conditioning work. Primarily the tool was visually observed and conditioning continued until a white crust of abrasives is visible on the tool surface. At this point, one hour polishing tests were performed between each hour of conditioning until a consistent removal is achieved. Relatively cheaper BK7 glass samples were used for these polishing tests. For Tool A1 eighteen hours of conditioning work were required to form a visually observable crust layer on the tool, and after that, hour long polishing tests started and continued until a consistent removal rate was obtained. Figure 4-11 presents the MRR obtained on BK7 workpieces during tool conditioning, error bars are the standard deviation of the material removal rates obtained on three samples. After approximately 30 hours of conditioning, the tool produced consistent removal rates. Figure 4-12illustrates a tool with such a crust.

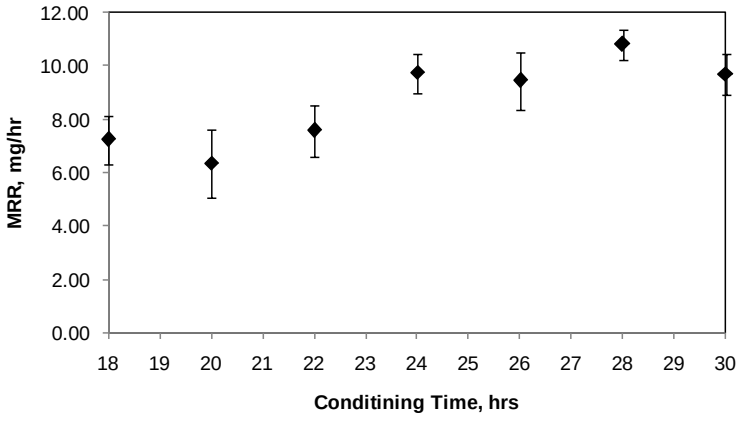

Figure 4-11: MRR obtained on BK7 during the tool conditioning period.

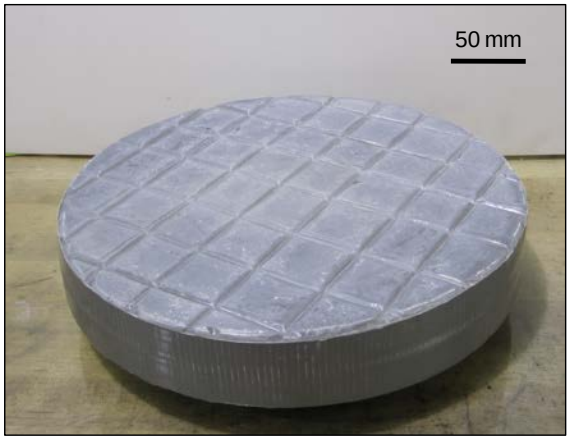

Figure 4-12: A grooved tool after 30 hours of conditioning work.

4.2.1.2 Tool Surface Evaluation

A closer examination of the tool surface topography was done for better understanding the possible contact mechanisms between tool and workpiece. The surface profile (topography), roughness and skewness of a conditioned tool that was used for polishing tests were evaluated. Directly after the final polishing test, approximately 45 hrs of conditioning and polishing, five 20 mm line profile scans were taken with a Taylor Hobson Talysurf profilometer (tip radius = 2 μm). For higher resolution analysis the crust was evaluated by an AFM machine. Immediately after Talysurf test suitably sized sections of crust samples were chipped off from the tool to fit within the DI 3100 AFM machine. Four 20 μm × 5 μm regions were examined. The resulting RMS roughness and skewness values are given in Table 4-2.

Table 4-2: Pitch tooling surface measurements.

Measurements	20 mm line scan (Talysurf)	5 µm × 20 µm area scan (AFM)
Average Roughness	R_q= 0.54 µm	S_q= 66.1 nm
Skewness±Stdev	-0.64 ± 1.54	-0.67 ± 0.16
Form removed / filters applied	Best fit line/ none	3rd order surface/ none

While Figure 4-13a shows three typical Talysurf profiles, Figure 4-13b shows three typical AFM line scans. To highlight the smoothness of the surfaces a 1 micron spherical particle is superimposed on the AFM measurements. The particle is distorted to reflect the different scales on the x (micron) and y (nanometer) axes. The scans and roughness data strongly support common place assumptions that during polishing the workpiece were primarily supported by the embedded abrasives and an intermittent fluid film.

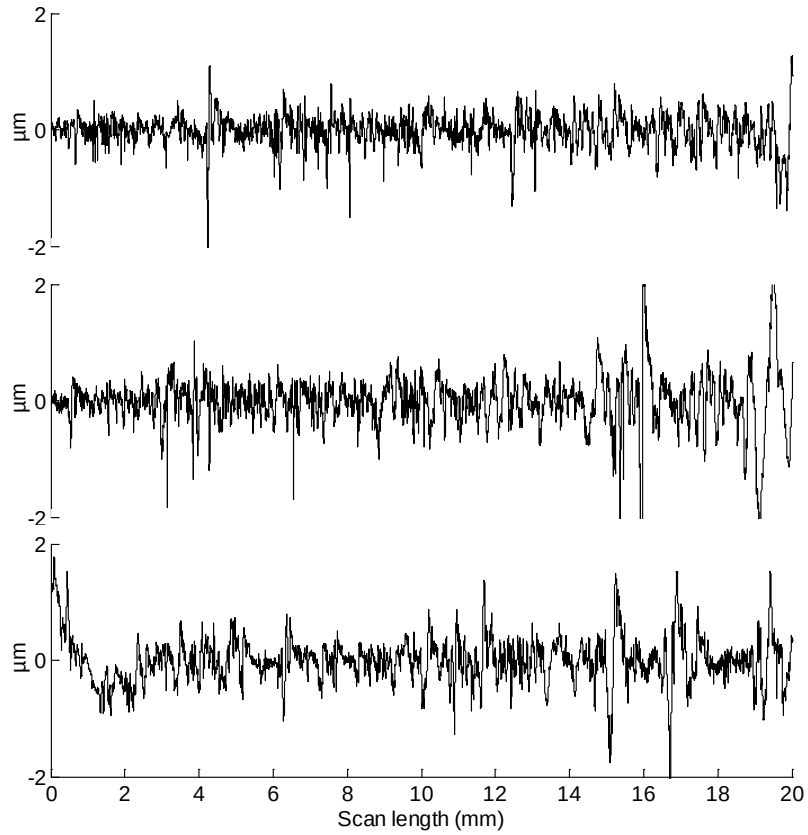

(a)

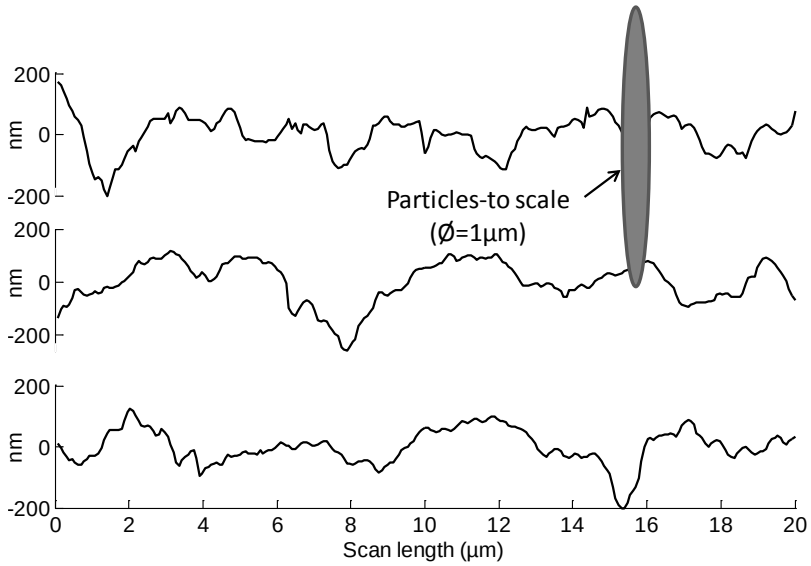

(b)

Figure 4-13: (a) Three Talysurf scans of the tool, (b) three AFM measurement of the tool.

4.2.2 Glass Workpiece

Fused silica glass samples were used in the polishing tests (Edmund Optics Glass Code: 7990 and Stock No: NT32-632-000, see Figure 4-12). The supplied samples consist of 99% of silica. Each sample came in the cylindrical form with a diameter of Ø =25 mm, and a flatness of 1/4 λ (λ = 632.8 nm). The physical properties of the samples are listed in the Table 4-3.

Figure 4-14: Fused Silica samples (Ø= 25 mm) used in the polishing tests.

Table 4-3: Properties of fused silica samples used in the polishing tests.

Parameter	Value and unit
Sample Diameter	25 mm
Sample Thickness	12.5 mm
Considered Surface	Single surface
Surface Flatness (PV_{rms}, λ = 632.8 nm)	1/4 λ
Density	2.2 g/cm^3
Coefficient of Expansion	5.5×10-7/°C
Young's Modulus	72.7 GPa
Knoop Hardness	522 kg/mm^2
Poisson's Ratio	0.16

4.2.3 Polishing Slurry

Fused silica samples were polished with a ceria slurry (Opaline). It consists of 1µm particles mixed with distilled water. The volumetric mixing ratio was 10 parts water, 1 parts ceria; water: ceria = 10:1 (in weight the ratio is ~ 7:1). Before each polishing test a half an hour conditioning was performed to allow the slurry to fully wet the tool. The slurry was delivered and recirculated with a variable speed peristaltic pump (Simon Manostate® 72-310-000). A magnetic stirrer used to stir the slurry and prevent settling of the slurry particles. Slurry pH was monitored using pH strips with four color points over a pH range of 1-14 where the slurry pH was 7.

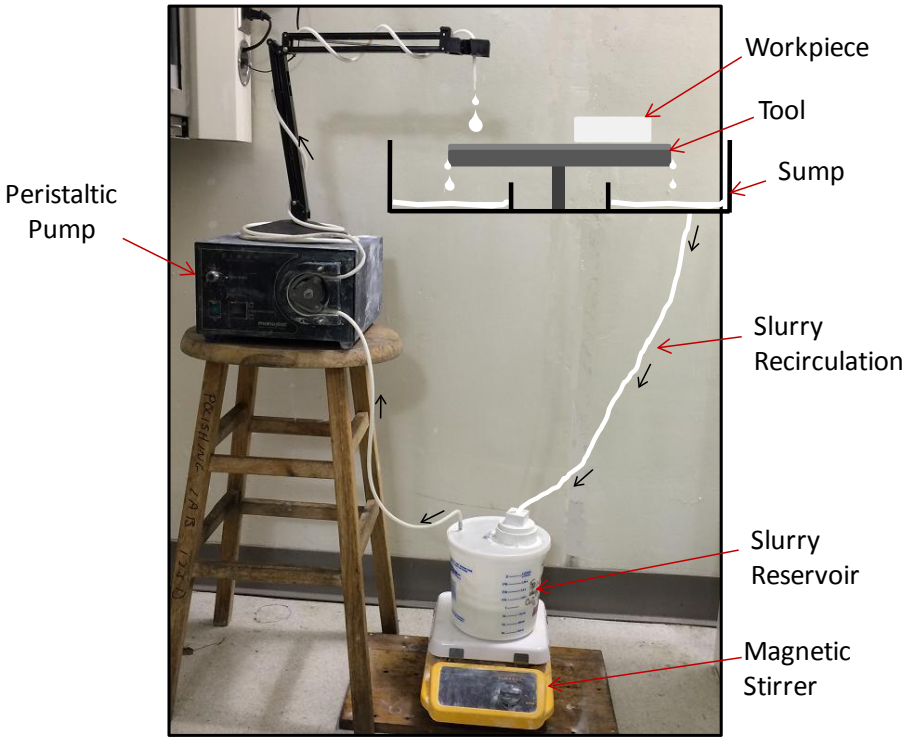

Figure 4-15: Peristaltic pumping and slurry recirculation system.

4.2.4 Test Conditions

To reveal the sensitivity of polishing outcomes to process vibrations a total of eighteen fused silica samples (Ø = 25 mm, t = 12.5 mm) were polished on the three tools (Tool A1, Tool A2 and Tool B, see Table 4-1). Each tool polished six samples, three on Machine 1, and three on Machine 2. For each tool the polishing tests alternated between machines, i.e. the 1st sample was polished on Machine 1 with Tool A1, the 2nd on Machine 2 with Tool A1, the 3rd sample on Machine 1 with Tool A1 etc. Similarly for the other two tools. An aluminum workpiece holder (Ø = 100 mm) with a 15 mm layer of Teflon/high density polyethylene (HDPE) on its one face was specifically machined to hold three samples simultaneously. The HDPE holder mounts a workpiece without the use of optical wax or adhesives. In the Teflon/HDPE layer the three glass pieces (workpiece) distributed equally with 120˚ apart and at mid radius from the center. In each test among the three samples one was fused silica and the other two were BK7. The polishing outcomes were evaluated only for the fused silica sample. The holder with the workpiece samples is illustrated in Figure 4-16a. Additional weight was attached to the holder so as to make it 3kg, see Figure 4-16b, so that each samples observed approximately 10N load on it.

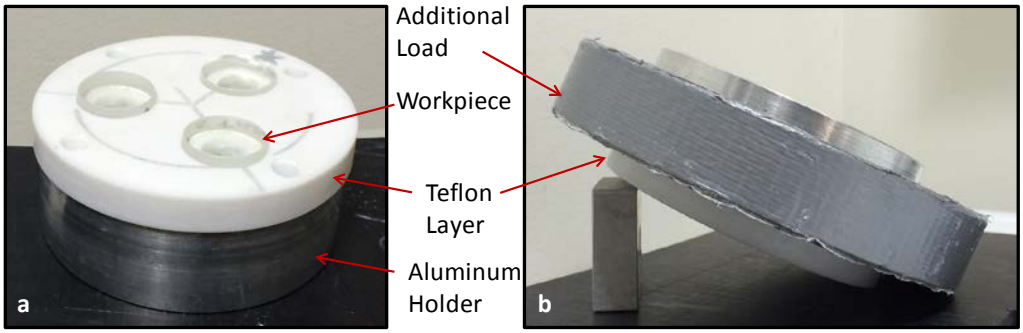

Figure 4-16: (a) Workpiece holder and (b) additional load (steel ring) attached to the holder.

The polishing process parameters and consumables are listed in Table 4-4. Both the MRRs and the surface finishes were evaluated after polishing. The mass of the glass was measured before and after polishing with an Ohaus-Adventurer analytical balance (Model AR0640) with a 250g capacity and a resolution of 0.1 mg. The weight loss method is subject to some potential errors such as cleanliness of the part after exposure to the slurry and water absorption by the workpiece and can fluctuate as a function of air humidity [24]. To address that concern, several steps were considered. After thoroughly rinsing the workpiece with soap and water and a final clean with an acetone soaked wipe, the sample was kept inside a low heat oven for several minutes to completely dry out the workpiece. The sample mass was recorded directly after removing it from the oven. A second set of measurements were performed to determine material removal rates based on the height difference of the workpiece before and after the polishing test. A micrometer with resolution of 0.1 μm was used to measure the height difference. Material removal rates obtained by both the methods were resulted in comparable values. The surface roughness values were measured by a scanning white light interferometer (Zygo NewView^{TM}5000 2.5× and 50× objectives), and by an AFM (Digital Instruments DI 3100). The range of instruments enabled comprehensive coverage of a wide spatial frequency range. Table 4-5 provides details on the measurement sizes, associated resolution. The same table also reported the bandwidth of machine vibrations that could be captured by the different measurement methods. The physical significance of these values are annotated below the Table 4-5.

Table 4-4: Process parameters used for vibration and polishing tests.

Machine kinematics	
Platen rpm	20 rpm
Over-arm swing rate	5 rpm
Additional details for the polishing tests	
Load	10N
Slurry composition	1 µm ceria: H_20 (1:10)
Slurry flow rate	6ml/min
Polishing time	60 min
Workpiece material	∅25 mm fused silica

Table 4-5: Surface roughness measurement methods, measurement sizes, and resolution.

		2.5× SWLI	50× SWLI	AFM
Measurement size		2.2mm×2.4mm	140 µm×110 µm	10 µm×10 µm
Approx. lateral Resolution		≈ 26 µm**	≈ 1.2 µm	≈ 0.16 µm
Form removed/filters		Cylindrical surface/ none	Cylindrical surface/ none	3rd order surface/ none
Machine vibrational frequency bandwidth* captured by instrument	Minimum Frequency	60 Hz	1 kHz	15 kHz
	Maximum Frequency	11 kHz	150 kHz	1 MHz

*The average velocity between tool and work piece, v = 150 mm/s. (evaluated in Appendix C). For this speed the minimum frequency corresponding to the average velocity (v) is the frequency which produce wavelength (λ) less than the length of field of view of the instrument ($f = v/\lambda$). The maximum frequency corresponding to the velocity is the frequency that produces wavelength greater than the minimum resolution of the instrument. That says, within the frequency bandwidth the corresponding wavelengths (λ) will be in within the range of minimum resolution and the length of maximum field of view.

** Based on Nyquist sampling theory (objective dependent)

4.3 Polishing Outcomes

4.3.1 Material Removal Rate (MRR)

Figure 4-17 shows how the MRRs varied between Machine 1 and 2 for the three tools. For each tool the ratio of the material removal rates obtained on the two machines is also reported. For all the tools the MRR is clearly higher on Machine 1.Though the removal rates vary for Tools A1, A2 and B, Tools A1 and A2 produced similar removal ratios between Machine 1 and Machine 2. The difference in MRRs between A1 and A2 could be attributed due to the quality of the crust formed on the tool. It was also noted that Tool A2 did not run as smoothly as Tool A1, there was additional workpiece chattering which was not present with Tool A1.

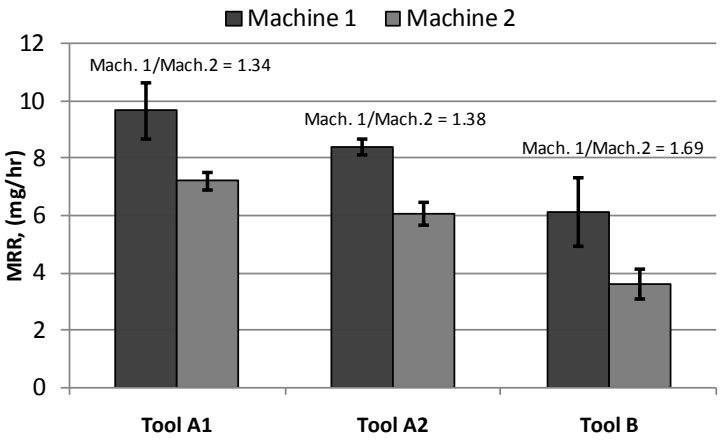

Figure 4-17: Variations in material removal rates between the machines for different tools.

The data in Figure 4-17 and Figure 4-10clearly demonstrate that differences in vibrational characteristics do have an impact on the removal rates. The question is how this difference in vibrational signatures affects the MRRs. The possible reasons are discussed in a later section, while Chapter 5 further analyzes the impacts of vibration on MRRs.

4.3.2 Surface Finish

Figure 4-18 depicts the averaged surface roughness values for all samples polished with Tools A1 and B on both machines. The error bars represents the standard deviations of nine measurements. For each of the tools, Machine 1 produced rougher surface than produced by Machine 2, though the observable differences are not significant for both the SWLI 50× and AFM measurements. The differences are only accountable for SWLI 2.5× measurements. That says the vibration has less impact on higher spatial frequency surface roughness values but has significant impact on lower spatial frequency roughness values. It is thought that high spatial roughness results from individual particle workpiece interactions while lower spatial roughness results from macro scale instabilities within the tool workpiece contact.

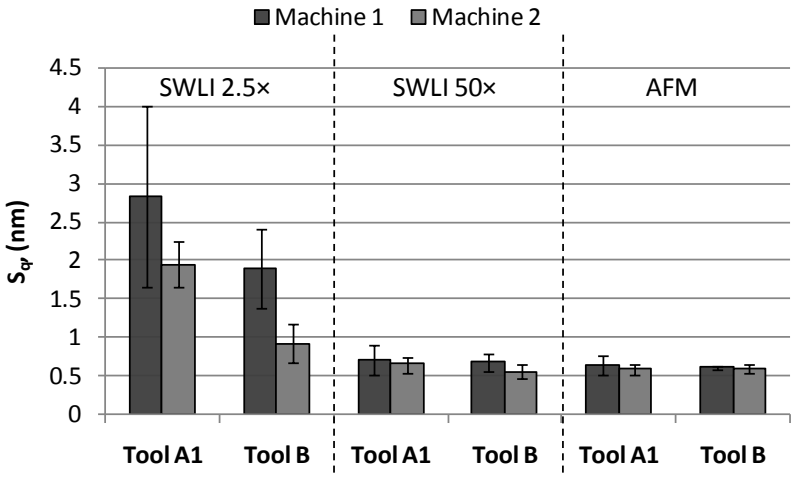

Figure 4-18: Fused Silica RMS roughness values obtained on two different machines.

4.3.2.1 PSD Analysis of Surface Finish

Power Spectral Density (PSD) of surface profile isolates periodic signals from the profile. The PSD transform generates a graph that plots periodic wavelength frequency (inverse of spatial distance) versus the strength of the signal at corresponding frequency. The PSD isolates the periodic marks on the surface corresponding to different spatial wavelengths. The bar chart in Figure 4-18 shows the distinctive differences in lower spatial surface roughness i.e. SWLI 2.5×. It is worth to looking at the corresponding PSDs to see if additional information can be extracted. According to the data presented in Table 4-5, the SWLI 2.5× and 50× can capture events resulting from machine vibrations in the 1 Hz – 16 kHz frequency ranges, the AFM cannot capture below 15 kHz. In this section the PSD analysis is only performed on the SWLI 2.5× measurements. The PSD analysis of the SWLI 50× measurements is recommended for future consideration.

Twenty separate line profiles were extracted from the SWLI 2.5× images, ten from samples polished on Machine 1, and ten from samples polished on Machine 2. The PSDs were generated using MATLAB code (see Appendix B) and the average PSD curves for both the machines are reported in Figure 4-19. The figure illustrates that for spatial frequencies >10 mm^{-1} the average PSD curves are not significantly different, while for spatial frequencies <10 mm^{-1} minute differences are evident. The PSD curves are zoomed in, in the lower spatial range (0 - 10 mm^{-1}) and presented in Figure 4-20.

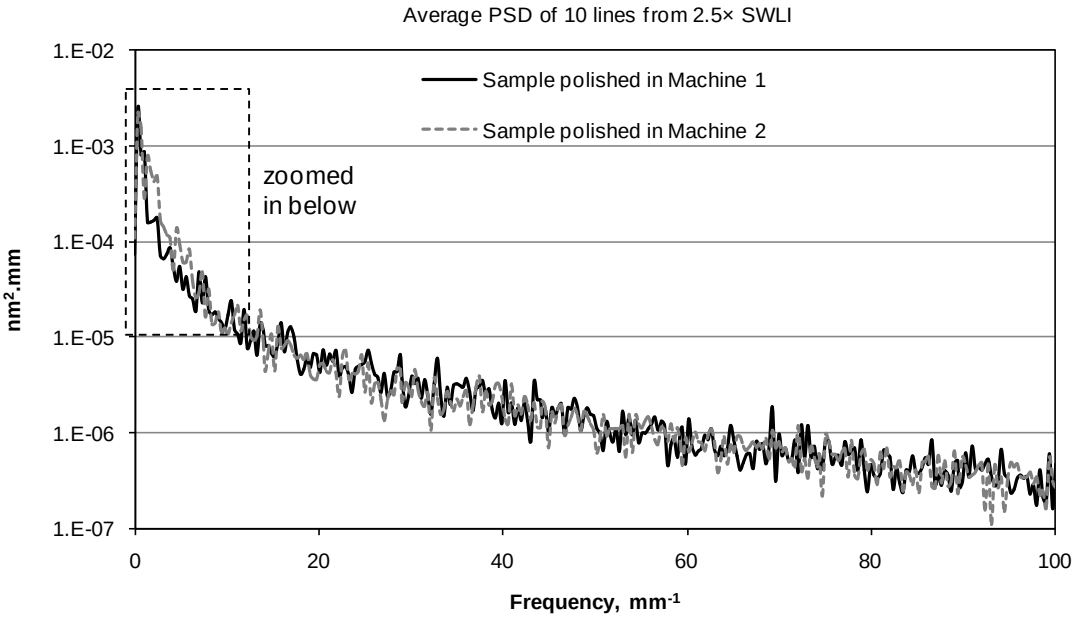

Figure 4-19: Average PSDs of glass surface between Machine 1 and Machine 2 (log in y axis).

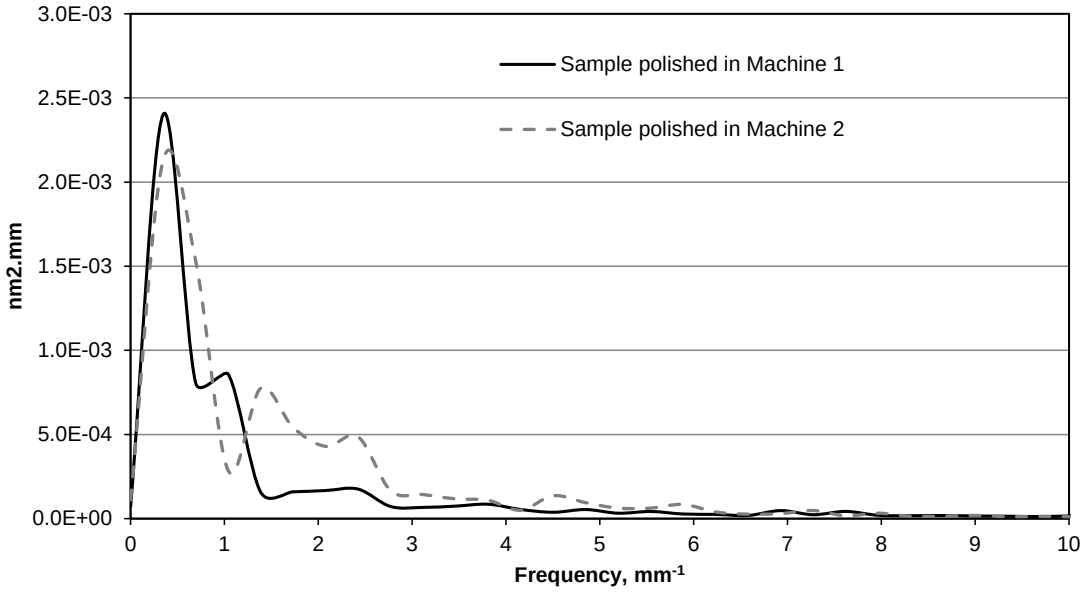

Figure 4-20: The lower spatial region is zoomed in from Figure 4-19(both axes linear).

In Figure 4-20 the average PSDs of samples polished in Machine 1 have two prominent spikes, 0.35 and 1.04 mm^{-1}, while for samples polished on Machine 2 the

noticeable spikes are at 0.39, 1.39 and 2.42 mm^{-1}. Each of the spikes corresponds to a spatial distance (λ, the inverse of the spike value) and for this λ there is a synchronous frequency (f) which correlates λ to the relative velocity (v) between tool and workpiece, see schematic in Figure 4-21a.

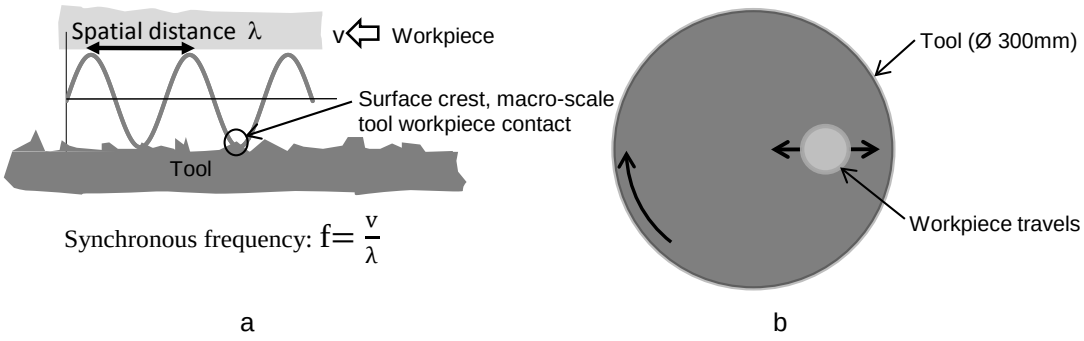

Figure 4-21: a. Synchronous frequency for spatial distance, b. Over-arm travel distance.

For a fixed polishing speed (tool speed = 20 rpm, over-arm speed = 5 rpm) the relative speed between tool and workpiece varies as the workpiece travels over the tool radius, see Figure 4-21b. In this polishing test the workpiece was set to travel back and forth between 40 mm and 120 mm of tool radius. The corresponding relative velocities between tool and workpiece over the radius are modeled in Appendix C and the approximate values range from 0.08 m/s to 0.2 m/s while the average velocity is 0.15 m/s. Table 4-6presents the synchronous frequencies for each of the spikes at these three velocities. The last column of Table 4-6 presents the dominant spikes in the FT of the process vibrations (Figure 4-10) within the synchronous frequency range. Defining the dominant spikes are the spikes which have amplitude not less than 60% of the largest spikes amplitude. Considering process vibrational peaks of 60, 120 and 180 Hz are due to the electrical noise, the largest spikes for Machine 1 and Machine 2 are 82.2 Hz and 215 Hz respectively.

Table 4-6: PSD spikes and corresponding synchronous frequency.

Machine	PSD spikes	Spatial distance, λ (mm)	Synchronous frequency, f = v/ λ (Hz)			Dominant spikes in the FT* (Hz)
			v = 0.08m/s	v = 0.15 m/s	v = 0.2 m/s	
Mc 1	0.35	2.86	28	51.45	73.5	38, 82.2, 158 and202
	1.04	0.96	83.2	152.88	218.4	
Mc 2	0.39	2.56	31.2	57.33	81.9	58 and 215
	1.39	0.72	111.2	204.33	291.9	
	2.42	0.41	193.6	355.74	508.2	

*FTs in Figure 4-10,the synchronous frequency bands are 28Hz – 218Hz for Machine 1 and 55Hz -508 Hz for Machine 2.

For the average velocity (v = 0.15 m/s) in Table 4-6, the synchronous frequency bands are 51.45 Hz - 152.88 Hz and 57.33- 355.74 Hz for Machine 1 and 2respectively. More generally the vibrational frequency band, 50 Hz - 350 Hz, is the bandwidth of interest for machine vibrational frequency in Figure 4-10. According to the PSD curves the process vibrations within this bandwidth could be expected to have an impact on the 2.5× surface roughness measurements. Moreover the area under the FT curve, represents vibrational energy, in this bandwidth is twice for Machine 1 compare to that of Machine 2.

From this PSD analysis, the general understanding is that the lower frequency response of the machines is responsible for the difference in the lower spatial frequency roughness values in Figure 4-18. However the PSD analysis performed above are based on sub-aperture measurements with a field of view of 2.2 mm × 2.4 mm (see Table 4-5), while the spatial distances in Table 4-6are in the range of 0.4 – 2.86 mm, which is close to the length of measurement area. That said, further measurements are required to

capture a larger area i.e. full-aperture measurements for better comments on the impact of vibration on very low spatial roughness.

4.3.3 Vibration-Induced Subsurface Damage

Dr. Wesley William performed etching tests to evaluate the impact of process vibrations on subsurface damage (SSD) levels. No significant difference was noticed between samples polished in Machine 1 and 2. Details of his evaluation techniques are presented in Appendix D.

4.4 Results Analysis and Discussion

While the exact reason why Machine 1 delivers higher MMRs is difficult to isolate from a limited number polishing tests, the most likely cause is the higher vibrational amplitudes for Machine 1 above 500 Hz, see Figure 4-10. The possible consequences of higher vibrational amplitudes include enhanced localized slurry circulation, higher cyclic loads, tool workpiece contact, and localized temperature increases due to the higher vibrational energy. Higher frequency vibrations could introduce enhanced micro pumping action of the slurry and therefore promote higher delivery rates of fresh slurry to the workpiece surface. Fresh slurry increases the surface modification rate and thus increases the MRRs. From mechanical point of view the cyclic loading could increase indentation depths by abrasive particles. In that case the removal increments should be closely proportional to the indentation depth [11] and thereby the higher removal rate would generate higher high-spatial surface roughness. However the resulted higher spatial roughness values are comparable between the machines. The conversion of vibrational energy in to temperature could change the viscoelasticity and hardness of pitch and consequently it’s expected polishing behavior [61]. The energy

conversion could result in localized heating at the particle scale and could reduce pitch stiffness locally. The particles could more easily embed in a locally softer pitch and this could enable easier crust formation and enhance the removal rates. While the evaluation of thin film slurry volume in between the tool and workpiece (calculated from Talysurf surface profile and 30% bearing contact) indicated that if the vibrational energy converts to heat the slurry temperature rise would be more than 100 ˚C which was undoubtedly not observed during polishing operation. In general the overall temperature was not increased significantly that could change the pitch grade. That says the increased MRR is more likely due to enhanced micro pumping of the slurry between the embedded particles on the pitch which accelerates the chemical activities.

In Figure 4-10 the ratios of vibrational amplitude above 500 Hz are over five times greater in Machine 1 than Machine 2. However none of the MMRs ratios in Figure 4-17 are even close to five, all are less than two. This suggests that the increased in removal is not due to the increase in mechanical indentation, if so the removal increments would be in the order of five times. This hypothesis is also supported by the AFM roughness measurements discussed below. However, to figure out the fundamental impact of vibration on removal rate it is necessary to isolate the impact of frequency and amplitude separately. This task would be difficult to perform on an actual polishing machine as there is no option to control the vibrations in a polishing machine. Thereby a separate test apparatus (test-bed) was built which facilitates testing at specified frequency and amplitude. A description of the test-bed, the experimental systems and the test results obtained are detailed in chapter 5.

The AFM surface roughness measurements in Figure 4-18 also supports the material removal mechanism. The similar roughness values in AFM measurements suggest that the increased MRRs is not due to an increase in the mechanical indentation depths that could result from higher amplitude vibrations, if this was true higher roughness values should be detected in the AFM measurements. Thus supports the argument that the increase in vibrations promotes localized micro pumping of the slurry and there by MRRs increase by increase in chemical activities. The arguments will further analyze in chapter 5.

4.5 Summary

Polishing machines operating under ‘identical’ workshop floor conditions have different vibrational characteristics. The amplitudes of the process induced vibrations are in the nanometer range. Fused silica samples polished with pitch tools on two different machines experienced different material removal rates and final surface roughness values. The machine with the greater vibrational amplitudes induced higher material removal rates and surface roughness values in the SWLI 2.5×. The most likely cause for higher MMRs is enhanced localized micro pumping of the slurry. Higher surface roughness values, which were most obvious in the lower spatial domain (SWLI 2.5×), are more likely caused by the difference in process vibrations in lower frequency range (50 Hz – 350 Hz).Further PSD analysis on a larger measurement area are suggested. The vibration analysis and the evaluation of polishing outcomes clarify that even minute levels of vibration can significantly increase achievable MRRs, while producing little to no effect on high-spatial surface roughness (i.e. AFM) and subsurface quality.

CHAPTER 5: TEST BED POLISHING

Analysis in previous chapters concluded that for polishing systems the magnitude of the process vibrations and their frequency content varied from machine to machine, and with process parameters such as platen speed and over-arm swing rates. Experimental test confirm that the different vibration signatures impact the process outcomes such as material removal rates (MRR) and surface finish. The question is how the process vibrations do impact on polishing outcomes, is it frequency or vibrational amplitude or combine of both? To get at the fundamentals it is necessary to isolate vibrations of different frequencies and amplitudes and directly measure their impact on the process outcomes. The task would be difficult to perform on an actual polishing machine as there has no control on its vibrations. This requires building a test-platform which can facilitate polishing with vibrations of distinct frequency and amplitude. First part of this chapter details the test-platform design, manufacturing and characterization. The later sections explain the test plans and polishing tests, presents the test results, and finally the results are explained with respect to the fluid and contact based models that developed by Professor Keanini. Comparisons of theoretical and experimental material removal rates show that the models proposed provide reasonable predictions of observed removal rates.

5.1 Platform Design and Fabrication

The set-up has two main components, a shaker table to excite the pitch tool, and a translation stage to provide relative motion between the sample and the tooling, see Figure 5-1. The stage is driven by a low friction, low vibration and precision ball screw mechanism. Two chrome-plated precision shafts and four self-aligning linear bearings support the stage. The translation distance is controlled by two SPDT push button switches on either side of the stage.

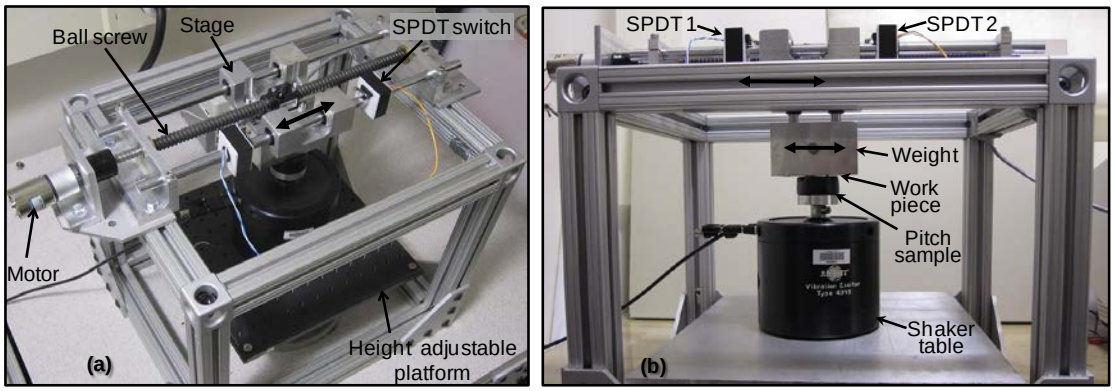

Figure 5-1: Photograph of (a) top and (b) side view of the test platform.

The stage is driven by a 12V DC motor with a maximum speed of 190 rpm. Motor power is supplied by a BK PRECISION DC voltage generator. The stage speed can be changed by changing the DC voltage to the motor. The maximum travel of the stage is 300 mm with a maximum velocity of 15 mm/sec. The stage changes its direction of movement when it hits the SPDT switch, see schematic in Figure 5-2 for clarity. When the stage hits the SPDT, the mechanical relay connections change the direction of the stage movement. The cycle continues until power supply turned off.

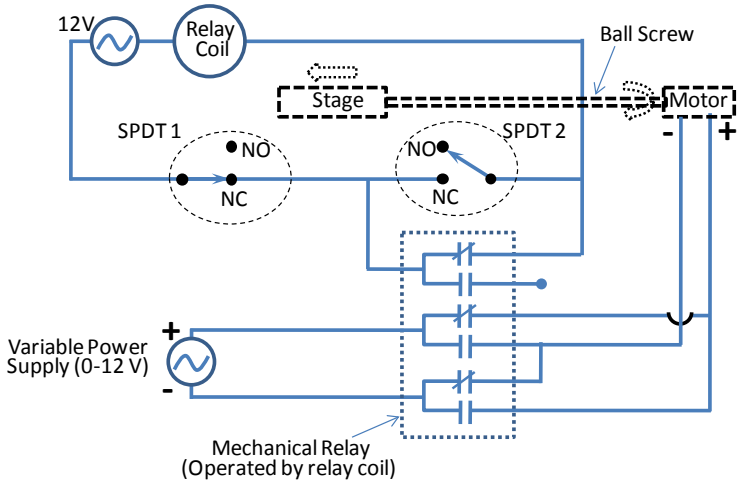

Figure 5-2: Mechanical Relay circuit that control the speed and travel distance of translational stage, relay coil circuit in closed position (SPDT = single point double through, NO = node open, NC = node close).

The workpiece attached to the stage using a specifically design workpiece holder. The workpiece holder consists of an aluminum block which is connected to the horizontal moving stage by two precision shafts, via linear bearings. The bearing allows smooth motion in the vertical direction while minimizing the tilt and tip of the sample as it moves across the pitch tool. The weight of the aluminum block (≈ 2kg) is selected such that the applied load on the workpiece is representative of polishing loads. Additional mass can be added if needed. A vinyl gasket between workpiece and holder (not shown in the picture) reduces any higher frequency vibrations being transmitted to the workpiece from the stage.

The pitch tool, a 22 mm thick layer of pitch on a 50 mm diameter aluminum platen, is screwed onto a shaker table (BK Vibration Exciter Type 4809). The shaker table, connected to a frequency generator and a vibration amplifier, can vibrate up to 20 kHz and at lower frequency the maximum possible displacement is 8 mm. The shaker table has resonance at 20 kHz. The shaker table shaft has maximum force rating 45N,

which is approximately 4.5Kg. For better understanding the stage movement and the polishing operation, a schematic of the test-platform is given in Figure 5-3. Polishing slurry is supplied to the polishing region by a separate delivery system. The delivery system is details in the tool preparation section.

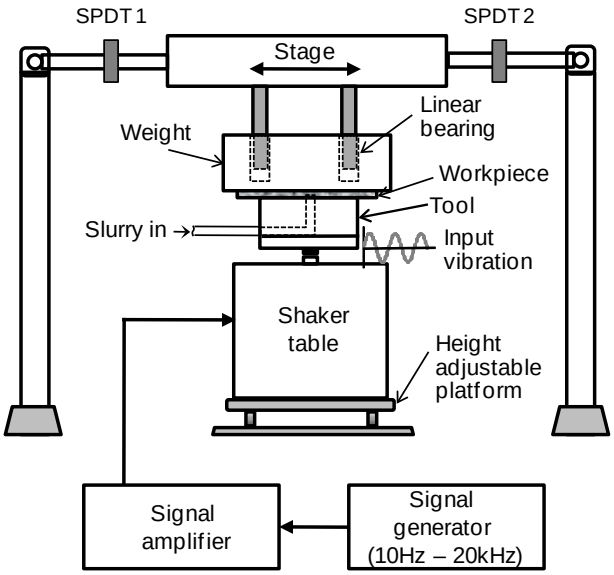

Figure 5-3: Schematic of the test platform.

5.2 Characterization of the Platform

The vibrations in the platform due to the stage movement are characterized for different running conditions. A PCB accelerometer (352B10) that operates up to 17 kHz is used to measure the vibration. The accelerometer attached to the workpiece is connected to a computer through a signal conditioner, an ADC converter, and a National Instruments DAQ card (6036E), which has a maximum sampling rate up to 200 kS/s. LabVIEW is used to record the accelerometer's response and to convert from the time into the frequency domain producing a FT plot. Ideally the vibration magnitude generated by the translation stage must be significantly less than that generated by a typical

polishing process. An initial goal was set at 80% less than that produced by the process. To assess the level of vibrations input into the workpiece by the mechanical translation of a glass workpiece over a pitch tool the vibrations were measured over 5 seconds while the stage ran at 0.5 m/min. The shaker table was not vibrating. Figure 5-4 shows the FT of the vibrations. The 60, 120 and 180 Hz spikes represent the electric noise of system power supply frequencies. Figure 5-4b. compares the results to the vibration signatures obtained from the Machine 1 and Machine 2. At frequencies above 500 Hz the platform and the Machine 2 have comparable signatures. These amplitudes are less than 20% of that generated by the Machine 1.

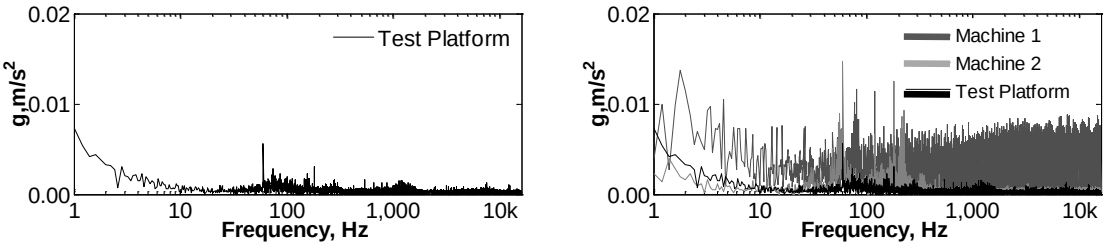

Figure 5-4: a. Platform vibration with no shaker table excitation, b. comparison with Machine 1 and 2 ($g = 9.81$ m/s^2, log in x axis).

The calculated peak displacement magnitudes for the Machine 2 at 250 Hz, 500 Hz and 1.2 kHz are 10 nm, 5 nm and 0.5 nm respectively. To generate these low levels of input vibrations using any mechanical system (here shaker table) is challenging. Of interest is to determine the best performance of the system at set frequency levels. To achieve this, the magnitude of the vibrations experienced by the workpiece as it translates over the vibrating pitch tool was recorded at tool frequencies of 250 Hz, 500 Hz, 1 kHz and 10 kHz. Figure 5-5 illustrates the accelerometer output over 0.04 s when the tool was vibrating at 250 Hz. This level of vibration corresponds to a peak to peak displacement

on the order of 500 nm. Figure 5-5 was obtained with the lowest shaker table drive voltage that produced a discernible sine wave. The peak displacements at 500 Hz and 1 kHz were 90 nm and 20 nm respectively. At 10 kHz displacements are in the order of 1 nm. As these values are all higher than the actual polishing process the test platform will not be able to directly replicate the polishing process. That said the achievable displacement with the test platform are still many orders of magnitude lower that those used in vibration assisted polishing processes and thus the test platform will enable an investigation into what affects the process outcomes more; amplitude of vibration, or frequency of vibration.

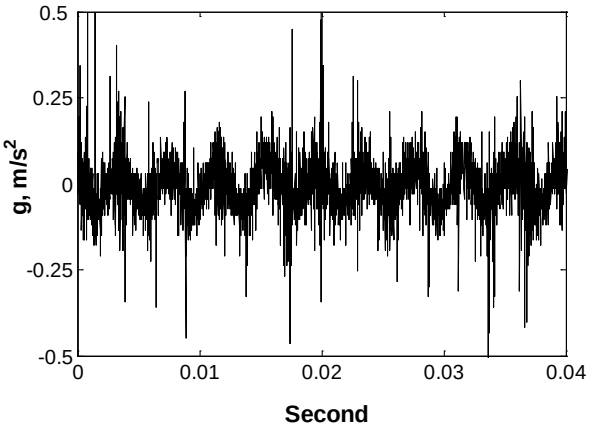

Figure 5-5: Vibrations measured on the workpiece as it translated over a vibrating pitch tool (250 Hz).

5.3 Special Tooling for Platform Test

The tools (Ø = 50 mm) specifically prepared for the platform testing were similar to the samples that used for dynamic test in chapter 3. Primarily Acculap™Soft pitch was considered for platform test which is denoted as soft tools.

5.3.1 Tool preparation

While the details of sample pitch tool making are provided in chapter 3, here the preparation of special tooling for the platform test are briefly described. As this is a non-conventional polishing configuration, the pitch tool required additional consideration with respect to slurry delivery. For stable operation the workpiece diameter (Ø=75 mm) was chosen greater than the tool diameter (Ø=50 mm), which hamper usual slurry delivery operation. A final design resulted in a silicon tube placed in the middle of the mold prior to pouring the pitch. After removing from the mold the final tool has the tube molded in the pitch layer, see Figure 5-6. The edge of pitch layer was carefully chipped off to create smooth and round edge which is less susceptive to tool chipping. The duct tape along the periphery prevents the pitch from long term flow and keeps the tool shape consistent over time. The top surface grooved in an 'H' shaped patterned to prevent hydroplaning of the workpiece over the tool. The grooving directly channeled the pumped slurry to the workpiece environment that allows slurry circulation with no pressure buildup in between the tool and workpiece. Prior to polishing, the tool was conditioned to develop a uniform abrasive crust on its topmost surface. The details of conditioning are presented in next section.

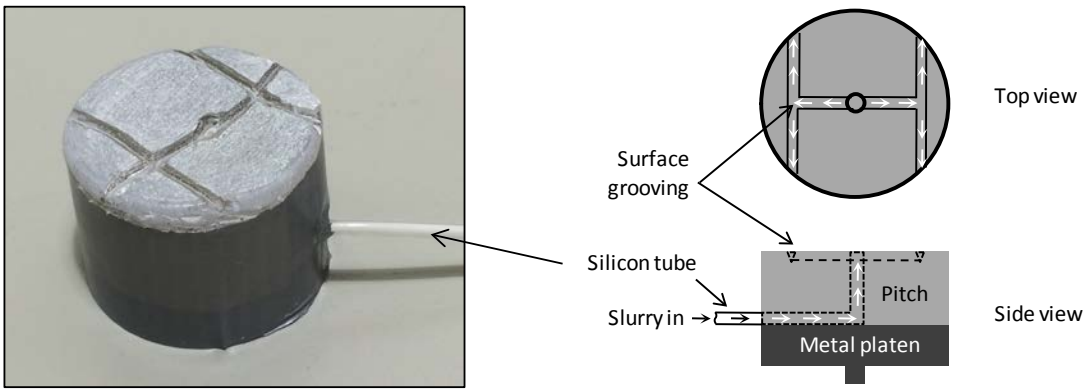

Figure 5-6: A conditioned tool, and the schematic of tool grooving and slurry circulation.

5.3.2 Tool Conditioning

In conditioning process the tool was slowly rubbed against a ground glass surface in presence of thick slurry solution (cerium: water = 1:1). The ground surface assists in embedding slurry particles into the tool more so than a smooth glass and therefore reduced the conditioning time. During conditioning the glass surface was kept lukewarm by supplying heated air to the substrate that used to hold the glass piece. That reduced pitch viscosity which resulted in flat tool surface and enabled more particles to embed in pitch. Flat tool allows better surface contact, reduces tip and tilted motion of workpiece, and provides smoother polishing operation. The embedded particles create a layer of slurry crust that is essential for polishing. The more conditioning allows more particles to embed and provides higher removal rates. Several hours of conditioning made the tool surface saturated with embedded particles and the removal rate became consistent. To evaluate the saturation in crust formation numbers of polishing tests were performed. Primarily the tool was visually observed and conditioning work continues until visible a crust layer covered the entire tool surface. Afterwards, hourly long polishing test were performed between conditioning periods. The test continued until a consistent removal rate was achieved. MRRs versus conditioning time are presented in Figure 5-7. The consistency in removal indicates the saturation in crust formation. The soft tool took six hours of conditioning to ensure saturation in crust formation. After conditioning the tools were characterized before the polishing test. Next section detailed the tool characterization techniques.

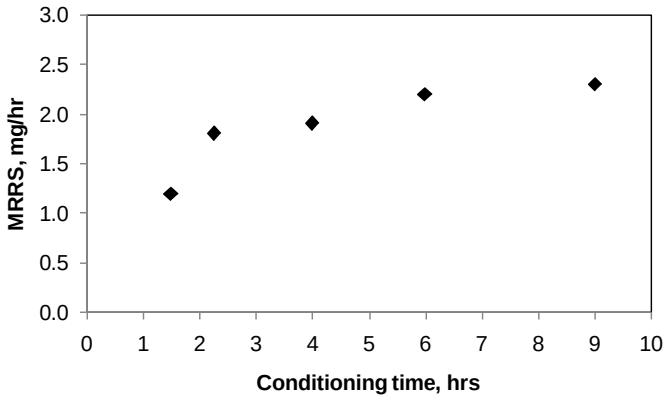

Figure 5-7: Soft tool conditioning and MRR stability check.

5.4 Tool Characterization

To characterize the topography of the conditioned tool surface roughness were evaluated. Visual observations clearly showed the white abrasive crust that built up its surface over time, see Figure 5-6. Directly after the final conditioning hours, three 20 mm line profile scans were taken with a Taylor Hobson Talysurf profilometer (tip radius = 2 μm). The RMS roughness and skewness values are given in Table 5-1.

Table 5-1: Pitch tooling surface measurements.

20 mm Talysurf scan	
Average R_q ± Stdev	0.18 ± 0.04
Skewness ± Stdev	-2.46 ± 0.48
Form removed/filters applies	Best fit line/ none

5.5 Testing Condition

In the frequency range of interest, 0-10k Hz, initially two distinctively different frequencies, 500 Hz as lower level and 8 kHz as higher level, were selected for the shaker table polishing test. For each of the selected frequency two amplitudes, higher and lower range, were considered. The subsequent sections described the factors considered for frequencies and amplitude selections.

5.5.1 Frequency Consideration

The frequency selections for the platform test are primarily based on the recorded vibration during actual polishing (Figure 4-10).The first attempt was to select two frequencies where one should be at lower and the other one at higher frequency regime in the specific frequency bandwidth of 0 to 10 kHz to identify the impact of low or high frequency on polishing outcomes. Initially the 80 Hz was thought as the lowest frequency for the platform test. However at reasonable platform speed, 7 mm/sec, the tool vibrating at 80 Hz cyclically hit the workpiece approximately at 88 µm apart. The cyclic hitting distance is defined here as the ripple wavelength [153], as illustrated in Figure 5-8.

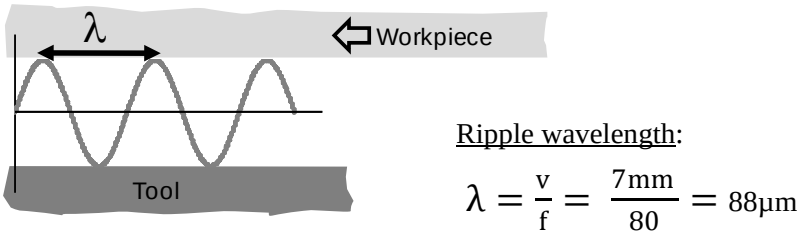

Figure 5-8: Schematic of ripple wavelength.

However, the field of views for SWLI 50× is 140 µm × 110 µm. That said the 88 µm ripple wavelength would be too long to visible in 50× objective, the best resolution objective available in the lab. The frequency 500 Hz which has ripple wavelength ≈ 15 µm, which is reasonable to observe under 50× interferometer and hence considered as lower frequency for the polishing test. The 8 kHz which is 100 times the initial lowest selection (80 Hz) was arbitrarily considered as a higher frequency. In final polishing test three additional frequencies in between the max and min were selected (1.5 kHz, 3 kHz and 5.5 kHz) for better understand the impact of vibrational frequency, see Table 5-3.

5.5.2 Amplitude Selection

At each frequency there is an amplitude limit to the minimum discernible sine wave that the shaker table can produce. Similarly at each frequency there is maximum amplitude limit that the shaker table can produce without mechanical failure. For shaker table the limiting displacements corresponding frequencies are provided in Table 5-2.

Table 5-2: Shaker table limiting frequency and amplitude.

Frequency	Minimum possible amplitude	Maximum possible amplitude
500 Hz	100 nm	35 µm
8000 kHz	4 nm	500 nm

The minimum amplitude considered for 500 Hz was 100 nm. To make possible comparison between frequencies with constant amplitude the 100 nm was also selected as the lower amplitude for 8 kHz. For actual polishing machine the ratio of vibrational amplitudes between the machines (Machine 1/Machine 2) was approximately 5 and hence 0.5 µm which is five times the 100 nm was considered as the higher amplitude for both of 500 Hz and 8 kHz. In final polishing test four additional amplitudes were selected (5 µm, 10 µm, 15 µm, 25 µm) for better understand the impact of vibrational amplitude at a set frequency, see Table 5-3.

5.5.3 Vibrational power Calculation

In addition to considering selected frequencies and amplitudes, the combined power of the input vibrations was also examined. Under single frequency input vibration the nominal vibrational power input can be approximated from a simplified schematic of power transmission (from the tool to workpiece) as illustrated in Figure 5-9.

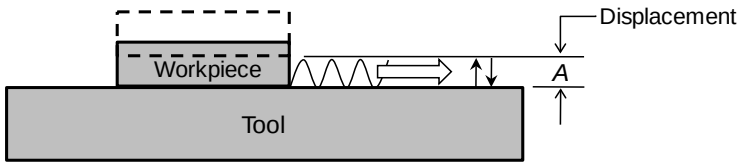

Figure 5-9: Schematic of vibrational power transmission from tool to workpiece

Since the forcing frequency is not near the natural frequency of the system the phase lag can be approximated to zero [168] and so the workpiece and tool have identical cyclic displacements. In a complete cycle the energy transmits in the first half of the cycle where the workpiece is forced to move upward against its weight (mg). For the second half of the cycle due to gravity the workpiece fall back along with the tool. According to the laws of motion, the transmitted power for the upward displacement against the work load is mgA. If the frequency of vibration is f, the total displacement in unit time is fA and the power transmission ismgfA, as provided in equation 5-1.

$$P_{in} = m \times g \times f \times A \qquad (5\text{-}1)$$

At 500 Hz the vibrational amplitude 1.6 µm generates power input which is equivalent to the power generated at 8 kHz with amplitude 100 nm. To evaluate the impact of equivalent power, the amplitude 1.6 µm was considered at 500 Hz. The equivalent powers were calculated from the relation $P=mgf_1 A_1= mgf_2 A_2$.

5.5.4 Polishing Test Conditions

Table 5-3 details the test conditions and process parameters selected for testing. Fused silica samples were polished with cerium oxide water-based slurry. An accelerometer attached to the workpiece confirmed the vibrational amplitudes and frequencies experienced by the workpiece during polishing tests. The right half of Table 5-3 provided the process parameters that used for the platform polishing test.

Table 5-3: Test conditions and process parameters.

Test conditions		Process parameters	
Frequency	Amplitude		
500 Hz, 8 kHz	100 nm	Tool speed	7 mm/sec
500 Hz, 8 kHz	500 nm	Load	10 kPa
500 Hz	1.6 µm	Slurry composition	0.2 µm ceria: H_2O = 1:10
1.5 kHz, 3 kHz, 5.5 kHz	500 nm	Slurry pH	7
		Polishing time	60 min
500 Hz	5 µm, 10 µm, 15 µm, 25 µm, 35 µm	Workpiece material	Ø75 mm fused silica
		Tool	Ø50 mm Acculap^{TM}Soft

5.6 Experimental Results and Discussion

The results from the test plan presented in Table 5-3 are utilized to evaluate the impacts of frequency, the impact of amplitude and the combine effect of both, the power of input vibration.

5.6.1 Impact of Vibrational frequency and Amplitude

All the test results with vibrational amplitudes of 500 nm and 100 nm are presented in Figure 5-10. At each condition three sets of test were performed and the values represent the average of three removals where the error bars represent the standard deviations. The frequency versus removal plots shows that for both of the frequency, 500 Hz and 8 kHz, the increases in vibrational amplitude (100 nm to 500 nm, i.e. five times) increases the MRRs. While at 500 Hz the five times increase in amplitude resulted in 27% higher removal rates, at 8kHz the same level of amplitude increments resulted in 75% higher removal rates. That says the higher frequency vibrations have more impacts compare to lower frequency. From the figure another visible difference is the removal rates versus frequency slope is higher (3.7×10^{-4} versus 1.4×10^{-4}) for 500 nm. The results

in Figure 5-10 clearly demonstrated that the removal rates depend on both frequency and amplitude of inputs vibrations i.e. the vibrational power. Although in this graph only two sets of amplitudes are considered, more analysis on higher amplitude input vibrations are provided in a later section.

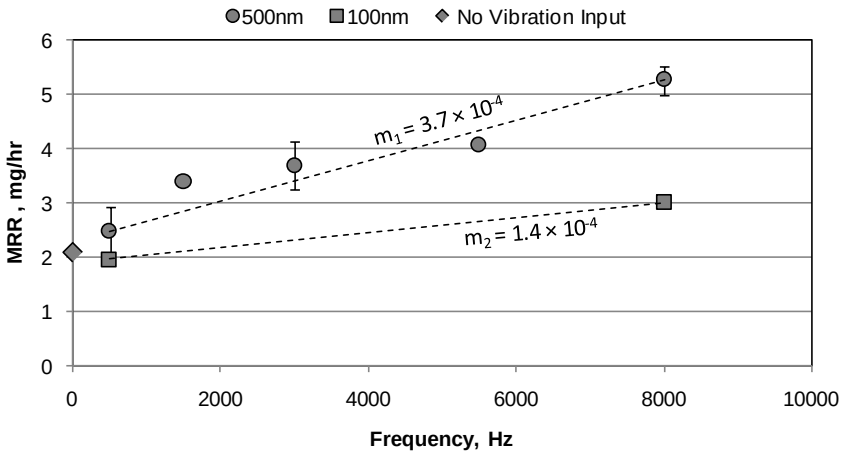

Figure 5-10: MRR versus vibrational frequency and amplitude.

5.6.2 Impact of Vibrational power

The same sets of test results that presented in Figure 5-10 are presented in Figure 5-11 where the removals are plotted against the vibrational power inputs, as calculated using equation 5-1. In addition two more data points are added. The first one denoted by the solid triangle, is the removal obtained when the input frequency and amplitude are 500 Hz and 1.6 µm, respectively. This testing condition provides the same power input (0.016 W) as testing at 8 kHz and 100 nm and consequently they have very similar MRRs. The second data point, denoted by the solid diamond, is obtained by polishing at a lower load, 1kg instead of 2kg, with vibrational conditions of 8 kHz and 500 nm. The reduction in load reduced the associated power by 50% while resulted in a 32% lower in removal rates and the resulting MRR falls along the same trend line as the other test

results. That says the MRRs follow the power of the input vibrations rather than individual amplitude and frequency. It is also noted that in Figure 5-11there is a linear relationship appears between the MRR and the vibrational powers. The question is how increasing in vibrational power increases removal rates? Does it enhance the chemical activity or increase the mechanical interaction?

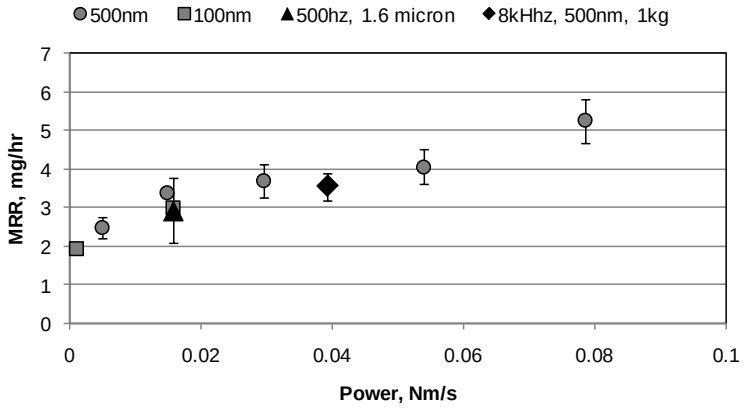

Figure 5-11: MRR versus input power.

5.6.3 Impact of Slurry pH

To verify the questions mentioned in previous sections number of polishing tests were performed with a chemically unfavorable slurry composition where slurry pH was reduced from 7 to 4 by the addition of HCl acid. The HCl chemically suppresses the chemical-mechanical removal, MRR_{cm}, see literature review for detail (section 2.4.2). Figure 5-12 compares the material removal rates obtained by polishing with slurries of pH 7 and pH 4 at higher (8 kHz, 500 nm) and lower (500 Hz, 500 nm) power input levels.

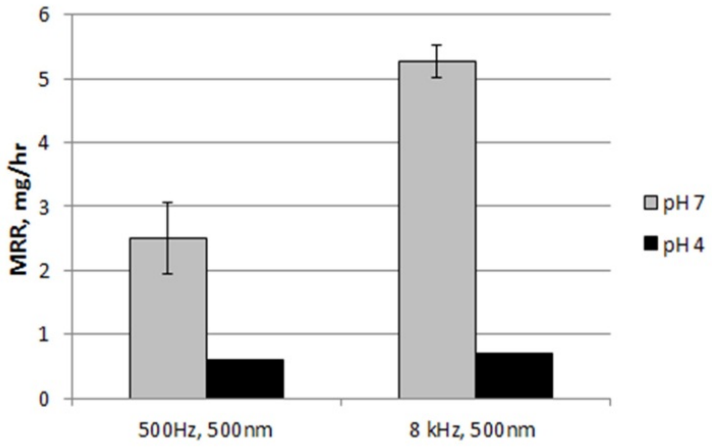

Figure 5-12: Impact of altering the slurry pH on the MRR.

As expected the MRR is lower with the pH 4, the slurry with acidic nature significantly reduces the formation of the hydrated layer [12], but most noticeably the MRR achieved with the lower pH slurry is independent to the vibrational input. These results confirmed that the increased in MRRs generates from the enhanced chemical activity produced by increased micro-pumping of the slurry or increased chemical reaction rates.

5.6.4 Results for Higher Vibrational Power Input

The interest of higher power input was to investigate if additional MRR could be achievable. As increase in input frequency was limited by the shaker table itself, the power input was increased by increase in vibrational amplitude while frequency was fixed at 500 Hz. Figure 5-13 depicts all the results performed under the condition of 500Hz input frequency while the amplitude varies from 0.1 µm to 35µm.

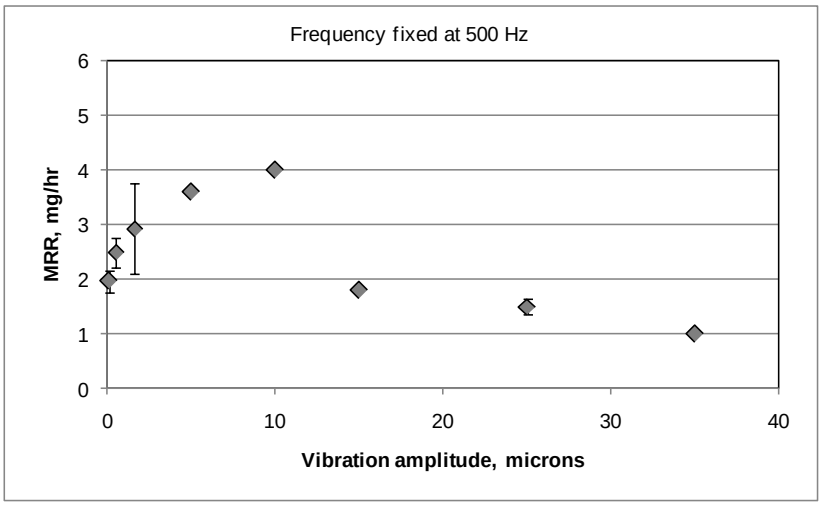

Figure 5-13: Vibrational amplitude at 500 Hz versus MRR

The plot shows, the MRR drops off sharply with vibrational amplitudes, A> 10 µm. To investigate the sharp drop off, accelerometers were attached to both the workpiece and tool to monitor the phase difference between tool and workpiece. Both accelerometers signals were measure simultaneously (sampling frequency 50 kHz) and the phase differences between the two signals were evaluated using xcorr function in MATLAB, see Appendix E. A zero phase lag indicates that both the workpiece and tool are synchronized thus are remaining in contact or a maintaining a constant fluid layer thickness. The existence of a phase lag indicates that the workpiece and tool are moving out of synchronization resulting in variation in the contact mode or fluid layer thickness. Table 5-4 details the recorded phase difference between the workpiece and tool accelerometer signals, and the corresponding maximum theoretical gap variation, G_{theory}, that could result from the phase difference. The latter is determined by subtracting two 500 Hz sine waves of the relevant amplitude separated by the corresponding measured phase lag from each other.

Table 5-4: Phase angle and maximum fluctuation in the fluid film thickness.

Input amplitude at 500 Hz, µm	Measured* phase lag,°	G_{theory}, µm
0.5	0	0
5	3.60	0.32
10	3.60	0.63
15	7.20	1.88
25	10.80	4.71

* Sampling frequency 50 kHz and shaker table frequency 500, i.e. sampling resolution 3.6 °, which indicates the phase lag in between is not possible to determine from this measurements.

The vibrational amplitude increases also increases the phase difference. A feasible consequence of this is thought to be intermittent contact between the workpiece and tool, or actual separation. Both scenarios will result in reduced contact between the abrasives and the workpiece surface resulting in lower material removal rates. The possibility of tool workpiece separation is supported by AFM roughness of tool surface. The AFM measurement found the root mean squared roughness, R_q, of a soft pitch tool crust to be approximately 66 nm. A general assumption, $3\times R_q$ value is approximately equivalent to the distance from the surface mean line to its highest peak, therefore when G_{theory} approaches $3R_q$, as it does when the input vibrations are $\geq$ 5 µm, results in complete separation of the workpiece from the tool. Under this condition the workpiece is supported by a slurry film that fills the gap. It is reasonable to assume that the complete separation will induce hydroplaning between tool and workpiece and allows only flow induced removals (MRR_{flow}). Based on the experimental results presented in this chapter, Professor Keanini proposed an analytical modeling that explained the influence of frequency and amplitude of process vibration in polishing mechanism. The full models

are provided in Appendix F while a short summary and model performance are presented in the next section.

5.7 Summary of Professor Keanini's Observations

According to the model, the total material removal in a polishing process, MRR_{tot} has two parts, the chemical-mechanical removal MRR_{cm} and the slurry flow-mediated removal, MRR_{flow}, as presented in equation 5-2. The chemical-mechanical removal mechanism assumes material removal takes place by a chemical tooth mechanism as outlined in Chapter 2. While the material removal by local shear and pressure gradient of local flow of the slurry is denoted as flow-mediated removal.

$$MRR_{tot} = MRR_{cm} + MRR_{flow} \tag{5-2}$$

Analysis of the slurry fluid dynamics between the tool and workpiece and the characterization of micro-topography of a conditioned tool led to a flow-mediated material removal model whereby the vibrations promote vertical and lateral accelerations of the fluid within the film. The pressure gradient and the shear forces associated with these accelerations and the flow-mediated material removals are considered as

$$MRR_{flow} \propto \sqrt{\frac{A}{d_o}}\omega \tag{5-3}$$

The model argued that for small amplitude input vibration ($A \leq 1.6\ \mu m$), the slurry film in between the workpiece and the tool is thin enough that the abrasives embedded in tool remain in contact with the workpiece. This is supported by AFM measurements of tool topography. In this condition the material removal takes place by both MRR_{cm} and MRR_{flow}, where the MRR_{cm} component is insensitive to small cyclic vibrations. The MRR_{flow} is sensitive to the vibrational frequency (f), amplitude (A), and

the thin gap between the tool and workpiece (d_o). Under this condition the removal model become

$$MRR_{tot} = MRR_{cm} + C_1\sqrt{\frac{A}{d_o}}\omega \qquad (forA \leq 1.6\ \mu m) \qquad (5\text{-}4)$$

where $\omega = 2\pi f$. Considering approximate proportionality between vibrational power (see eqn. 5-1) and removal rates the model proposed an alternative of equation 5-4 which is

$$MRR_{tot} = MRR_{cm} + C_2 mgA\omega \qquad (forA \leq 1.6\ \mu m) \qquad (5\text{-}5)$$

For higher amplitude input vibration ($A \geq 5\ \mu m$) the model argued that due to the larger gap in between tool and workpiece ($d_o \geq G_{theory}$ in Table 5-4), the workpiece loses contact and remain separated from the tool by a thin continuous film of slurry. This is supported by the gap measurement in Table 5-4 and the AFM roughness of tool topography. In this condition the MRR_{cm} being absent and the total removal become

$$MRR_{tot} = MRR_{flow} = C_3\sqrt{\frac{A}{d_o}}\omega \qquad (forA \geq 5\ \mu m) \qquad (5\text{-}6)$$

Equation 5-4, 5-5 and 5-6 dictates the removals presented in Figure 5-10, Figure 5-11 and Figure 5-13 respectively. The comparison between the experimental results and the theoretical model predictions are presented in Figure 5-14 a, b, and c. Considering MRR_{cm} = 2.1 mg h^{-1}, the removal at no input condition in Figure 5-10, constantC_1in equations 5-4 was calculated from the least square fit of data for A = 500 nm in Figure 5-10 and also used it to fit data for A = 100 nm. ConstantC_2in equation 5-5 were calculated from correlating equations 5-4 and 5-5, where $C_2 mgA\omega = C_1\sqrt{\frac{A}{d_o}}\omega$,while putting the values of C_1 from equation 5-4. The model predictions were determined by applying equation 5-4 where d_o= 200 nm (3×AFM roughness) is fixed, ω and A varies

accordingly. Constants C_1 and C_2 that calculated for A = 500 nm were also applied to A = 100 nm. In Figure 5-14 for $A \leq 1.6$ μm the theoretical material removals were calculated by applying equation 5-4 where both ω and d_o are fixed (500 Hz and 200 nm respectively) and A varies (0-1.6 μm). Constant C_3 of equation 5-6 was calculated from the least square fit of four data points for $A \geq 5$ μm in Figure 5-13. For these four points the theoretical prediction were calculated from $\omega = 500\,\text{Hz}$ while d_o and A varies accordingly as presented in Table 5-4. As illustrated in Figure 5-14 a, b, and c, for both small and large amplitude limits, the model provides reasonable predictions of experimental removal rates.

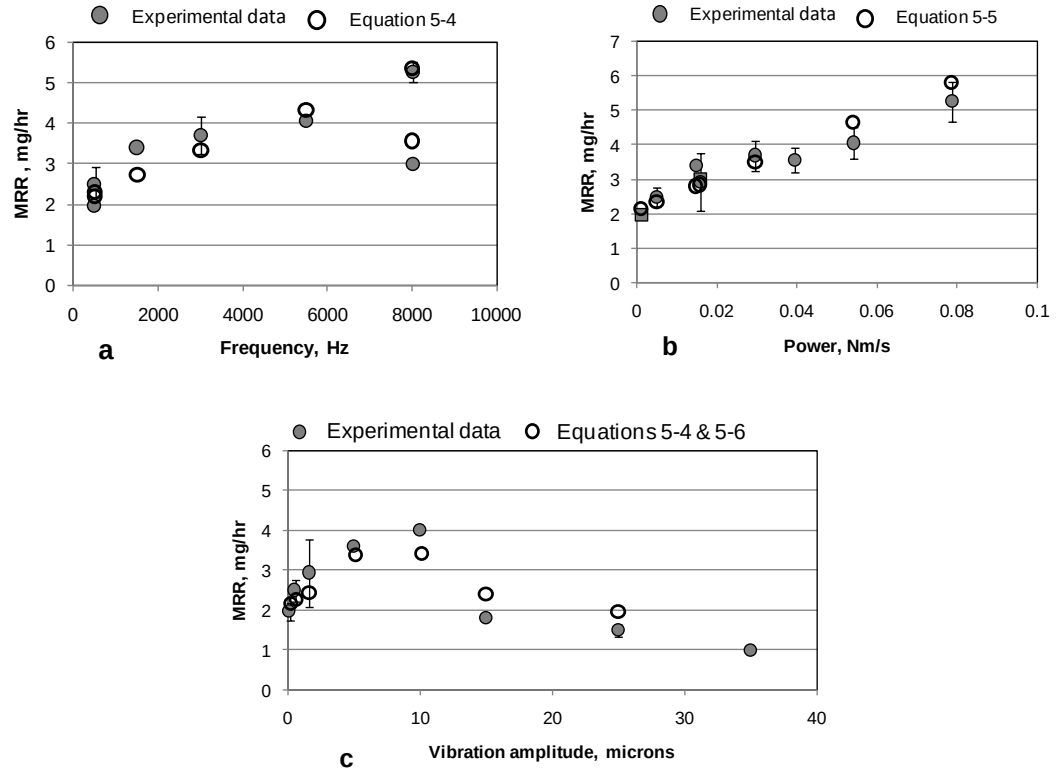

Figure 5-14: Comparison between the theoretical model predictions and the experimental results. a. between equation 5-4 and Figure 5-10, b. between equation 5-5 and Figure 5-11, and c. between equation 5-6 and Figure 5-13.

5.8 Conclusions

A test-bed was designed, fabricated and characterized to facilitate polishing under better defined vibrational amplitudes and frequencies. Polishing of fused silica samples demonstrated again that small amplitude vibrations affect polishing outcomes. Significant correlations are observed between the vibrational power and the material removal rates. For small amplitude input vibrations (A <1.6 µm), higher vibrational powers resulted in higher removal rates. The large amplitude input vibrations (A > 5 µm) generated a phase difference between the tool and the workpiece and is thought to lead to a separation between the tool and the workpiece (Table 5-4). This separation resulted in lower removal rates. The separation gap limits the effectiveness of increasing the amplitude past 5 µm. Keanini's model which considers both mechanical and fluid dynamics demonstrated that at small amplitudes the total material removal is determined by both a chemical-mechanical removal component, MRR_{cm}, and vibration driven flow induced removal component, MRR_{flow}, i.e.$MRR_{tot} = MRR_{cm} + MRR_{flow}$. While at large amplitudes the proposed separation of tool and workpiece by a fluid layer eliminates the MRR_{cm} component and under these condition, $MRR_{tot} = MRR_{flow}$. Comparison between theoretical and experimental removal rates demonstrated that the model can provide reasonable predictions for a wide range of input frequencies and amplitudes.

CHAPTER 6: PITCH GRADE (HARDNESS) AND MODEL PERFORMANCE

To evaluate how pitch grade (hardness) affects material removal rates and surface finish, tests similar to those conducted in chapter 5 are repeated with a tool fabricated from a harder pitch grade. Detailed physical and geometrical analysis of the tool surfaces are presented. The results are discussed with respect to those obtained for a soft tool and the MRRs predicted by Dr. Keanini's model.

6.1 Pitch Grades Evaluated

The tool in chapter 5 was made from Acculap^{TM}Soft pitch, while in this chapter Acculap^{TM}VeryFirm pitch was used to make a harder tool. The physical properties of the two pitch grades are summarized in Table 6-1.

Table 6-1: Basic comparison between hard and soft tool [2, 56].

Property	Soft Tool	Hard Tool
Pitch grade	Acculap^{TM}Soft pitch	Acculap^{TM}VeryFirm pitch
Shore D Hardness	60	80
Softening point °C	63	74
Approximate Shear Viscosity (GPa-s = 10^{10} poise)	0.1	8
Impact Test Natural Frequency (kHz) [7]	7.3	8

6.2 Tool Preparation

The preparation and conditioning process for hard a tool is similar to that used for the soft tool in Chapter 5. However in order for the hard tool to achieve a consistent crust of embedded abrasives the conditioning time was much longer, approximately 35 hours

versus only six hours for the soft tool. To check the consistency of the crust formation, polishing tests were performed during the conditioning period. MRRs versus conditioning time are presented in Figure 6-1 which shows after 35 hours of conditioning the material removal rate was reasonably consistent.

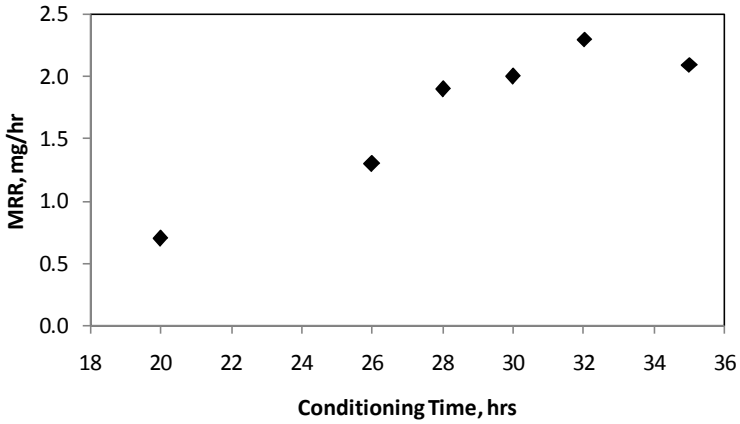

Figure 6-1: Hard tool conditioning and MRR stability check.

6.3 Tool Characterization

Results presented in chapter 3 suggest that the pitch grade does not have a significant influence on the magnitude of the vibrations transmitted through the pitch layer within the tested frequency range (1 Hz - 16 kHz), see Figure 3-5, and therefore the pitch's bulk properties are not considered to significantly affect the material removal rates. That said the interaction between the tool and workpiece depends on the formation of an abrasive crust on the tool's surface, a difference in crust formation could be expected to result in significantly different MRRs. To investigate this further both tool surfaces underwent fundamental analysis to quantify their basic surface topography. Atomic Force Microscopy (AFM), Scanning Electron Microscopy (SEM), and Energy Dispersive Spectroscopy (EDS) analysis were performed to create concrete blue prints of

the different tool surfaces, enabling tool quantification. These analyses provide required parameters mentioned in section 6.5.1, that utilized to verify the Keanini's model performance with respect to the pitch hardness.

The tools used in the polishing tests were approximately 30mm in thickness and were not thin enough to fit in either the SEM or AFM machine. To overcome this constraint, dummy hard and soft tools, which have thickness as of less than 10mm, were prepared and conditioned. The conditioning times for the dummy tools were similar to that performed on actual tools. Figure 6-2illustrates an actual tool used in the polishing test and a dummy tool. Though the dummy tool surfaces were not exactly the same as the actual tool surfaces, it is assumed that the dummy surfaces are sufficiently representative to facilitate comparison.

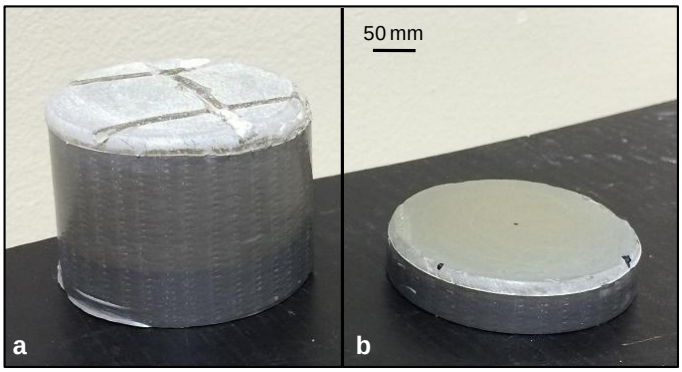

Figure 6-2: a. Actual tool and b. Dummy tool that used for AFM and SEM evaluation.

6.3.1 SEM and EDS Analysis

The SEM and EDS analysis were performed on both tools coated with 5 nm layer of gold (Au). Sample SEM images are presented in Figure 6-3. The images clearly show that abrasive particles are embedded in the pitch surface. The EDS analysis, presented in Figure 6-4, reinforces the visual impression that the topmost layer consists primarily of

cerium oxide particles (Ce and O peaks). Figure 6-4 represents the EDS results of a tool (Acculap™Soft) (a) before and (b) after conditioning. Top most surface of the conditioned tool is rich in cerium and oxygen where, no cerium or oxygen is present on the unconditioned tool's surface.

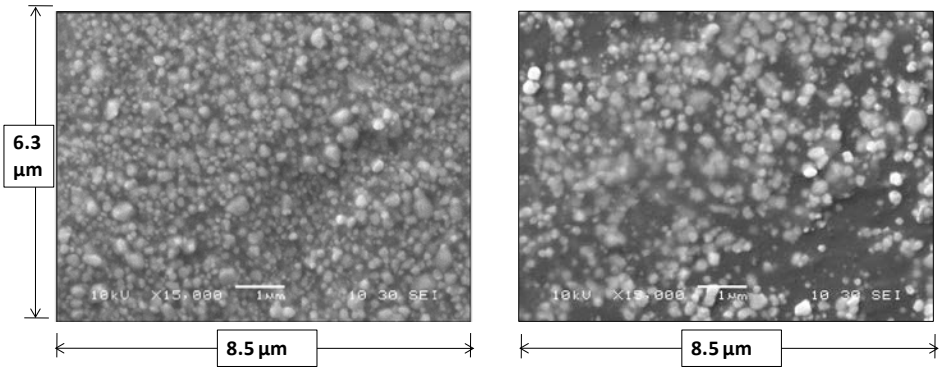

Figure 6-3: SEM images of two conditioned tools, (a) Acculap™Soft (b) Acculap™ VeryFirm (bright areas are embedded ceria particles).

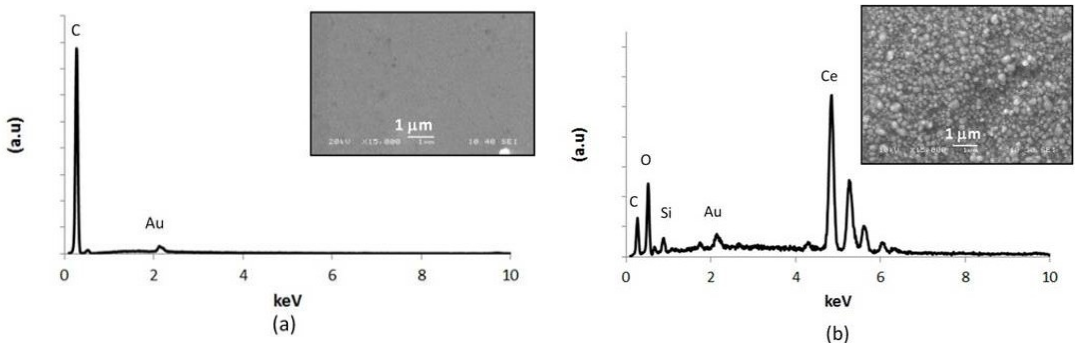

Figure 6-4: (a) EDS of an unconditioned, and (b) a conditioned tool (soft tool).

To evaluate and quantify the SEM images of the tool surfaces, MATLAB was used to process the images and identify the size and population of embedded particles in each tool type. The code utilizes a built in MATLAB function, the 'Strel' function, for disc counting and the program is available as 'Snowflakes Granulometry' [169].The details of how the code proceeds are provided in Appendix G. The program performance

was evaluated by applying it to analyze a number of control images generated in Microsoft Paint [170], which contain a known number of ‘particles’ of known size, see Figure 6-5. In the images the white circles represent the particles and the black region represents the pitch. The particles sizes are different in the two images, one has particles with a diameter of 0.25 µm while the other depicts particles with a diameter of 0.5 µm. Each image has 130 particles, i.e. the population is 2.65 particles/μm^2.A color gradient at the particle edge was selected to better replicate the SEM images in Figure 6-3, where it was observed that the edge of a particle has 50%lower grayscale values than at the center. In the control image the outer 30% of the particle radius contains a color gradient, i.e. for a particles with Ø = 0.25µm the diameter without color gradient is approximately 0.175 µm, (70%, as illustrated in Figure 6-5). For these two control images the program estimates the particles diameter to be 0.233 µm and 0.488 µm respectively and the associate populations were calculated to be 2.57/μm^2 are 2.61/μm^2. It is worth mentioning that for a control image, with particles Ø = 0.25µm and without any color gradient, the program particle diameter prediction was 0.24µm.The program predict values, with and without color gradient, which are reasonably close to the actual values (<10% error). Further analysis was performed with control images containing particles (Ø = 0.25 µm) that overlapped by 60% of their diameter, see reference [171] for images with overlapped particles. For these images the program’s estimation of particle diameter was 0.252 µm. As a final verification two SEM images, one of a soft tool and the other of hard tool were processed by hand. The numbers of particles in the images were manually counted. The results evaluated by manual and MATLAB approaches were comparable. It

found that the MATLAB calculated populations had true errors on the order of 10% error.

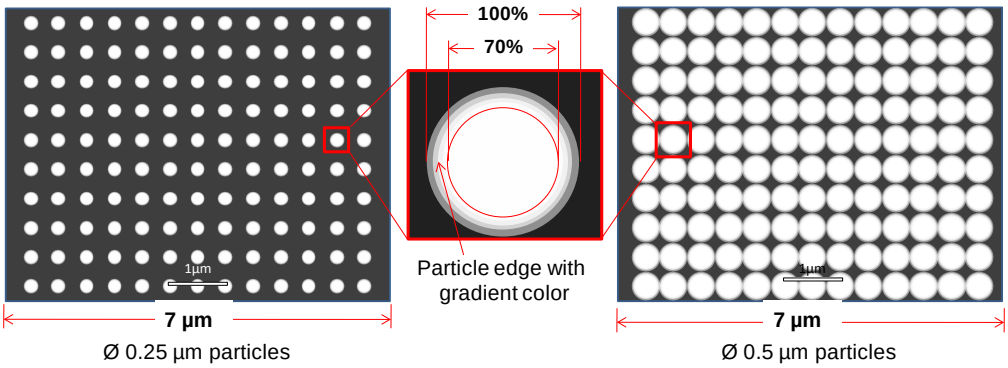

Figure 6-5: Sample images with known particle size and density, the zoomed in image of the particle.

Another MATLAB code (see Appendix H) was written to calculate the percentage of bright area in the SEM images based on threshold gray scale values. The threshold point was selected to be 128 (gray scale value) and grayscale values below this threshold value were considered as dark area. The bright areas represents the slurry crust formed by embedded slurry particles, while the dark areas represents the pitch with no embedded particles, see Figure 6-3. The performance of this code was verified by using the control images in Figure 6-5(known % of bright area) and found that the code can exactly predict the percentage of bright area.

Using the two MATLAB programs described above, the population of particles and the percentage of bright area were calculated for several SEM images. For each tool, twenty SEM images of the surface were evaluated and the results are reported in Table 6-2. The values in Table 6-2 represent the average values and the standard deviations of the measurements from the SEM images. Further analysis utilized the percentage of

bright area and the population values to calculate the lateral spacing between two particles, see Figure 6-6.

6.3.1.1 Lateral Spacing

One important parameter considered in Keanini's model is the lateral spacing between two embedded particles; this plays a role when determining the flow mediated component of the overall material removal. To estimate the lateral spacing between particles, l_p, see Figure 6-6, it is assumed that the embedded particles are uniformly distributed and the over the tool surface. The schematics of particle distribution and cross section of the soft tool surface are illustrated in Figure 6-6.

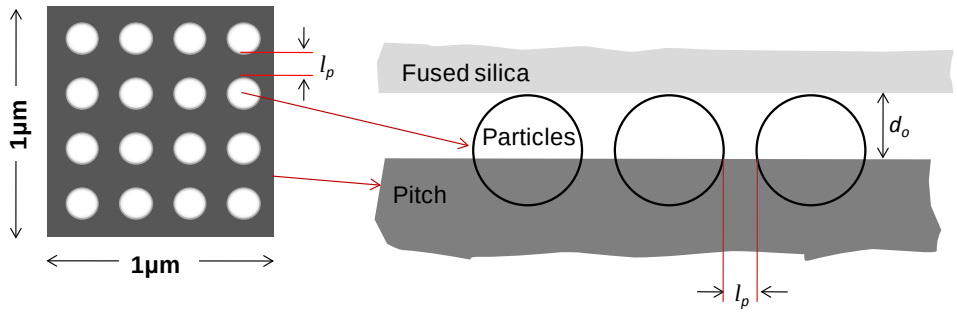

Figure 6-6: Schematic of embedded particles and lateral spacing (l_p) for uniformly distributed particles.

From SEM analysis, the number of embedded particles per unit area on a soft tool is estimated at $(17\pm3)/\mu m^2$, i.e. there are approximately 4 ± 0.5 particles uniformly distributed along a 1µm length as illustrated in Figure 6-6. While the percentage of bright area (slurry crust) for soft tool is 82 ±8.6%. Which means, if the diameter of the particles image for soft tool is $Ø_s$ then $17(\pi/4)Ø_s^2 = 0.82\ \mu m^2 \Rightarrow Ø_s = 0.24\ \mu m$. Thereby in a 1 µm length, as illustrated in the Figure 6-6, $4Ø_s + 4l_{ps} = 1\ \mu m$ where l_{ps} is the lateral spacing between two embedded particles. Thereby approximately the lateral spacing for soft

tool, $l_{ps} \sim \frac{1-4\times0.24\ \mu m}{4} \sim 10$nm. Similar analysis for the hard tool provided, $l_{ph} \sim \frac{1-3.5\times0.26\ \mu m}{3.5} \sim 26$ nm.

The approximate lateral spacing for hard and soft tools are reported in Table 6-2. The estimated values are also supported by the visual observation whereby it was observed that the soft tool has more area covered by embedded particles and thereby a higher number of particles per unit area compared to that of hard tool. For further verification two SEM images were printed out and the numbers of particles were manually counted and comparable values are noticed as reported in Table 6-2.

Table 6-2: Measurements from SEM image analysis, standard deviations (Stdev) are for twenty separate images of each tool.

Parameters	Acculap^{TM} Soft Tool	Acculap^{TM}VeryFirm Tool
Number of embedded particles per unit area, Particles density ±Stdev	17 ±3 /μm^2	13 ± 2 /μm^2
% of bright area, the area covered by slurry crust	82 ±8.6	69 ±6.6
Approximate lateral spacing between embedded particles, (nm)	10	26

6.3.2 AFM Analysis

The AFM roughness for the soft tool was presented in chapter 5. For hard tool four 20 μm × 5 μm AFM scans were taken using a DI 3100 AFM instrument. The RMS roughness and skewness values for both the tools are presented in Table 6-3.

Table 6-3: AFM roughness and skewness values for soft and hard tools.

5 µm × 20 µm scan (AFM)		
Parameters	Acculap^{TM}Soft Tool	Acculap^{TM}VeryFirm Tool
Average S_q	66.1± 11.98 nm (This is for tool A1)	112± 55.47 nm
Skewness ± Stdev	-0.67 ± 0.16	-0.23 ± 0.28
Form removed / filters applied	3rd order surface/ none	3rd order surface/ none

6.4 Polishing Test and Results Analysis

Polishing tests with the hard tool were performed on the same test-bed that was described in chapter 5. In addition to the initial base line test with no input vibration, tests were performed at three different vibrational frequencies, 500 Hz, 5.5 kHz and 8 kHz. For all selected frequencies the amplitudes were fixed at 500 nm. At each frequency three polishing tests were performed. The polishing process parameters were the same as those detailed in Table 5-3 in chapter 5.

6.4.1 Test Results: Comparison with Soft Tool Results and Discussions

The removal rates and surface finishes resulting from polishing with the hard and soft tools test are presented in Figure 6-7 and Figure 6-8. The values presented are the average over three polishing tests while the error bars represent the standard deviations.

The results in Figure 6-7 shows how increases in input vibrational frequency increase the MRR for both hard and soft tools, however the increment slope is higher for the soft tool (≈ 30%). For both the tools the base line tests with no input vibrations resulted in similar removal rates (≈ 2.1 mg/hr).

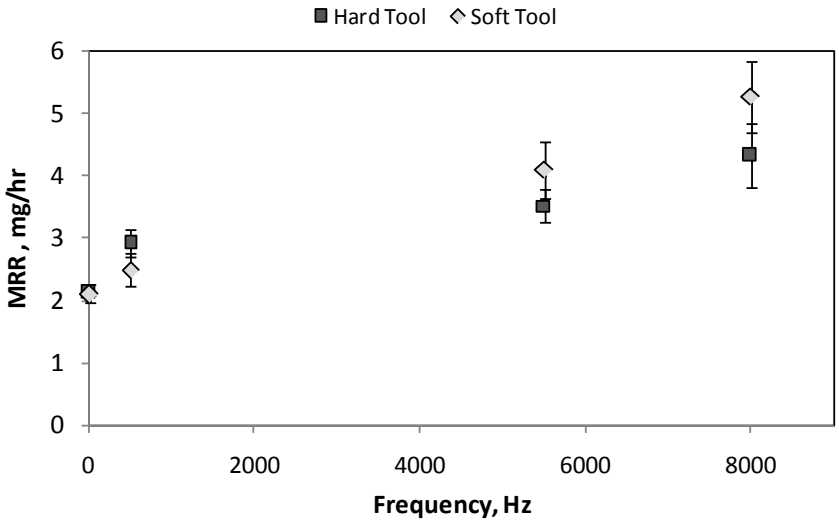

Figure 6-7: MRR versus vibrational frequency for both hard and soft tools.

The results in Figure 6-8 shows the high (SWLI 50×) and low (SWLI 2.5×) spatial roughness of workpieces polished on both soft and hard tools. In all the cases, the hard tool produced rougher surfaces when compared to that produced by the soft tool, however the differences are more noticeable in the lower spatial frequency domain and at vibrational frequency of 8 kHz.

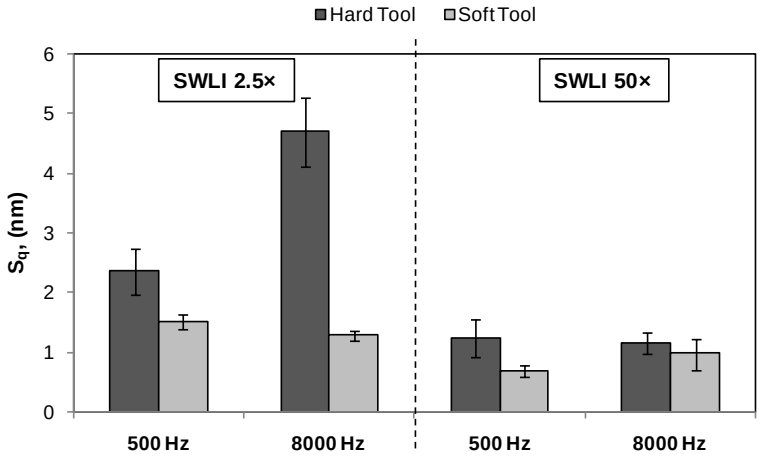

Figure 6-8: Surface finish, RMS roughness values for hard and soft tools (vibrational amplitude fixed at 500 nm).

6.5 Keanini's Model with respective to Hard Tools

The material removal model that was outlined in chapter 5 and presented in Appendix F is an analytic model, which takes the geometric characteristics of the tool surface into consideration. According to the model the MRR obtained while polishing in the presence of process vibration (MRR_{tot}), is the combined action of: 1) vibration-insensitive chemical-mechanical removal, MRR_{cm}, and 2) flow-induced removal, MRR_{flow}, whereby the later is produced by cyclic, vibration-driven acceleration of the polishing slurry film:

$$MRR_{tot} = MRR_{cm} + MRR_{flow} \quad (6\text{-}1)$$

In this section the influence of the tool's properties and surface characteristics on the polishing MRR is evaluated. Geometrical and mathematical analysis is performed to evaluate the ability of the model to accommodate different tools (pitch grades and tool topography). The following sub-sections evaluate the MRR_{cm} and MRR_{flow} components separately.

6.5.1 Chemical-mechanical Removal (MRR_{cm}) Aspect of the Model

According to the model, when polishing with sinusoidal vibrations, the average chemical-mechanical removal (MRR_{cm}) is independent of the vibrational frequency and amplitude (they average out to zero), while for non-sinusoidal vibrations, theMRR_{cm}term is sensitive to vibrations. Under cyclic loading the extremely thin slurry film ($\sim$200 nm, based on 3×AFM RMS roughness value of the tool surface) in between the tool and the workpiece generates a viscous damping force, $F_{viscous}$, and the contact between tool and workpiece generates as elastic contact force, $F_{elastic}$. Keanini estimated that the elastic contact force dominates the viscous force by a factor of $\sim 10^5$and this suggests that the

viscous force is negligible compared to the elastic force. That said the change in MRR_{cm} between soft and hard tools due to the change in pitch grade would be mainly influenced by the associate elastic force of the variation. In the model the elastic force is represented by:

$$F_{elastic} = \frac{E_{particle} \times \delta_c \times a^2 \times N_c}{S_q} \quad (6\text{-}2)$$

Where δ_c = the characteristic elastic deformation of tool-embedded polishing abrasives,

a = the characteristic radius of abrasive-workpiece elastic contact zones,

$E_{particle}$ = the polishing abrasive elastic modulus

$N_c = D_o^2 d_p^{-2}$ = total number of abrasive-workpiece contact points, where D_o is the workpiece diameter, and d_p = the characteristic diameter of the polishing abrasives

S_q = AFM roughness values of the tool crust.

In equation 6-2, $E_{particle}$ is same for both the tools, thereby the ratio of the elastic force between soft and hard tools become,

$$\frac{(F_{elastic})_{Soft}}{(F_{elastic})_{Hard}} \sim \frac{\delta_{cs}}{\delta_{ch}} \times \left(\frac{a_s}{a_h}\right)^2 \times \frac{N_{cs}}{N_{ch}} \times \frac{S_{qh}}{S_{qs}} \quad (6\text{-}3)$$

The subscripts ‘s’ and ‘h’ denote soft and hard pitch respectively. Equation 6-3 represents the ratio of elastic forces between the soft and hard tool. Following sections analyze and estimate each of the ratios on the right side of Equation 6-3.

6.5.1.1 The ratio of elastic deformation, $\frac{\delta_{cs}}{\delta_{ch}}$

The elastic deformation of tool-embedded particles under polishing pressure depends on the elasticity of pitch, slurry particles and workpiece material. According to the theory [11], the deformation (Δ) is inversely proportional to the elastic modulus of the

material ($\Delta \propto \frac{1}{E}$). However, the elastic modulus of the glass and slurry particles is much higher than that of pitch (30 to 80 times) [11, 75, 85] and the displacement due to pitch deformation dominants the other two. Therefore the total displacement can be approximated by the Equation 6-4.

$$\delta_c = \Delta_{pitch} \propto \frac{1}{E_{pitch}} \tag{6-4}$$

Using Equation 6-4 the ratio of total elastic deformations become,

$$\frac{\delta_{cs}}{\delta_{ch}} = \frac{\frac{1}{(E_{pitch})_{Soft}}}{\frac{1}{(E_{pitch})_{Hard}}} = \frac{(E_{pitch})_{Hard}}{(E_{pitch})_{Soft}} \tag{6-5}$$

As estimated from reference [56], the hard and soft Acculap™ pitches are equivalent to Gugolz73 and Gugolz55 respectively [Table 2-1], thus the elastic modulus for hard and soft pitch are taken as those reported [11] for Gugolz73 and Gugolz55 respectively.

$$(E_{pitch})_{Soft} = 2.055 \times 10^9 Nm^{-2} \text{ and } (E_{pitch})_{Hard} = 2.455 \times 10^9 Nm^{-2}$$

where the estimation of the modulus for the soft pitch is obtained by extrapolation of the data presented in table 6 in reference [11]. By putting these values into equation 6-5 the ratio becomes,

$$\frac{\delta_{cs}}{\delta_{ch}} \sim \frac{(E_{pitch})_{Hard}}{(E_{pitch})_{Soft}} \sim 1.2 \tag{6-6}$$

That implies for the same applied polishing pressure the resulting deformation is higher for a soft pitch when compared to a hard pitch.

6.5.1.2 The ratio of Abrasive-workpiece Elastic Contact Zone, $\left(\frac{a_s}{a_h}\right)^2$

Two separate methods were applied to calculate this ratio, and both methods produced similar values.

Method 1:

From Cook's [12] analysis, the elastic contact radius between a particle and the workpiece is given by:

$$a = \left\{\frac{3}{4} p \left(\frac{d_p}{2}\right)\left[\frac{1-v^2}{E} + \frac{1-v'^2}{E'}\right]\right\}^{\frac{1}{3}} \quad (6\text{-}7)$$

Where d_p is the characteristic diameter of the polishing abrasives, v and v' are the poison's ratio and E and E' are the modulus of elasticity for glass and particles respectively. All the parameters in right side of Equation 6-8 is same for both hard and soft tool except the pressure (p) on a single particle, which is different and depends on the particle concentration (K) in tool surface. From Equation 6-7,

$$\left(\frac{a_s}{a_h}\right)^2 = \left(\frac{p_s}{p_h}\right)^{\frac{2}{3}} \quad (6\text{-}8)$$

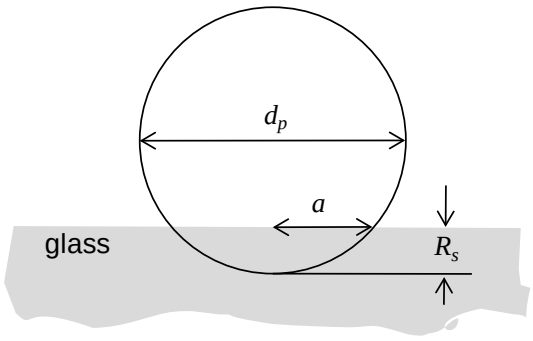

Figure 6-9: Particle scratching workpiece [12].

Cook stated that, the bearing load on a single particle (p) depends on the total load per unit area (P) on the tool, particle diameter (d_p) and the concentration of embedded particles (K) as defined by the Equation 6-9:

$$p = \frac{3Pd_p{}^2}{2K} \tag{6-9}$$

From equation 6-8 and 6-9

$$\left(\frac{a_s}{a_h}\right)^2 = \left(\frac{K_h}{K_s}\right)^{\frac{2}{3}} \tag{6-10}$$

The SEM analysis determined the percentage of area covered by particles on tool surface (see Table 6-2), which is equivalent to the particles concentration. Therefore the values of particles concentration for hard and soft tools are $K_h = 69 \pm 6.6$ and $K_s = 82 \pm 8.6$ respectively. This means the ratio defined in equation 6-10 can be rewritten as

$$\left(\frac{a_s}{a_h}\right)^2 = \left(\frac{69-6.6}{82+8.6}\right)^{\frac{2}{3}} \text{ to } \left(\frac{69+6.6}{82-8.6}\right)^{\frac{2}{3}} = 0.78 \text{ to } 1.02 \tag{6-11}$$

Method 2:

Brown [11] and Cook [12] analyzed the penetration depth caused by particles into the workpiece. For particles abrading the workpiece under pressure (P), where the elastic modulus of workpiece is E, and the concentration of embedded particles is K, the depth of penetration (R_s) can be represented by,

$$R_s = \frac{3}{4}\left[\frac{P}{2KE}\right]^{\frac{2}{3}} \tag{6-12}$$

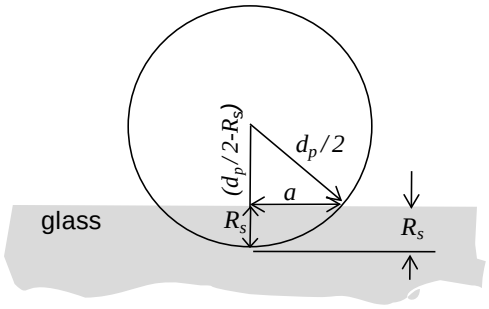

$$a^2 + \left(d_p/2 - R_s\right)^2 = \left(d_p/2\right)^2$$

$$\Rightarrow a^2 = R_s(d_p - R_s)$$

Figure 6-10: particle workpiece interaction, scratching depth R_s.

For a particles abrading the workpiece with depthR_s, from the geometrical analysis as provided in Figure 6-10, $a^2 = R_s(d_p - R_s)$. Considering the hard and soft tools produce different depth of penetration, R_{ss} and R_{sh} respectively, the ratio becomes

$$\left(\frac{a_s}{a_h}\right)^2 = \frac{R_{ss}(d_p - R_{ss})}{R_{sh}(d_p - R_{sh})} \qquad (6\text{-}13)$$

where d_p is on the order of 200 nm (from analysis of particle sizes for both hard and soft tool SEM images) and from Cook analysisR_s is in the order of 0.2nm [12].As R_s>>d_p, it can be considered that$(d_p - R_{ss}) \sim (d_p - R_{sh})$which simplifies the Equation 6-13 in to,

$$\left(\frac{a_s}{a_h}\right)^2 = \frac{R_{ss}}{R_{sh}}. \qquad (6\text{-}14)$$

Replacing R_s from Equation 6-12 in Equation 6-14, the ratio becomes $\left(\frac{a_s}{a_h}\right)^2 = \left(\frac{K_h}{K_s}\right)^{\frac{2}{3}}$ which is exactly similar to Equation 6-10 that obtained from a different approach in Method 1.

6.5.1.3 Number of abrasive-workpiece contact points, $N_c = D_o^2\, d_p^{-2}$

From Table 6-2 the estimated total number of particles per unit area is $N_{cs} = 17 \pm 3$ and$N_{ch} = 13 \pm 2$for soft and hard tool respectively. The ratio of contact points

$$\frac{N_{cs}}{N_{ch}} = \frac{17-3}{13+2} \text{ to } \frac{17+3}{13-2} = 0.9 \text{ to } 1.8 \qquad (6\text{-}15)$$

6.5.1.4 AFM roughness of the particles-embedded tool surface, S_q

The AFM roughness from Table 6-2 for soft and hard tools are S_{qs} = 66nm and S_{qh} = 112nm respectively, the roughness ratio becomes

$$\frac{S_{qh}}{S_{qs}} \sim \frac{112}{66} \sim 1.7 \qquad (6\text{-}16)$$

Substituting the high and low approximate ratio values from equations 6-6, 6-11, 6-15 and 6-16 into Equation 6-3 gives a range of elastic force ratio values between soft and hard tool.

$$\frac{(F_{elastic})_{Soft}}{(F_{elastic})_{Hard}} \sim (1.2 \times 0.78 \times 0.9 \times 1.7) \text{ to } (1.2 \times 1.02 \times 1.8 \times 1.7) \sim 1.4 \text{ to } 3.7 \qquad (6\text{-}17)$$

So the ratio of the elastic forces between soft and hard tool are ranges from 1.4 to 3.8. However, the chemical mechanical removal, MRR_{cm} is proportional to the contact stress [112,8]:

$$MRR_{cm} \propto \frac{F_{elastic}}{A_{contact}} \qquad (6\text{-}18)$$

$$\frac{(MRR_{cm})_{Soft}}{(MRR_{cm})_{hard}} \sim \frac{(F_{elastic})_{Soft}}{(F_{elastic})_{hard}} \times \frac{(A_{contact})_{Hard}}{(A_{contact})_{Soft}} \qquad (6\text{-}19)$$

Assuming uniform contact between tool crust and workpiece, the contact area is the area of abrasive crust which is represented by the percentage of bright area in Table 6-2. So, the ratio of contact area between hard and soft tool is,

$$\frac{(A_{contact})_{Hard}}{(A_{contact})_{Soft}} \sim \frac{69 \pm 6.6}{82 \pm 8.6} = \frac{69-6.6}{82+8.6} \text{ to } \frac{69+6.6}{82-8.6} = 0.68 \text{ to} 1.03 \qquad (6\text{-}20)$$

Putting the values from Equation 6-17 and 6-20 in to equation 6-19, the ratio of removal rates become,

$$\frac{(MRR_{cm})_{Soft}}{(MRR_{cm})_{hard}} \sim 1.4 \times 0.68 \text{ to } 3.7 \times 1.03 = 0.95 \text{ to } 3.8 \qquad (6\text{-}21)$$

The ratio of chemical-mechanical removal rates between hard and soft tools is in the range of 0.95 to 3.8. From the experimental test the removal rate obtained with no external vibrational input represents the MRR_{cm}component i.e., the MRR at x = 0 in Figure 6-7.For both hard and soft tools the MRR_{cm} component is 2.13 mg/hr and 2.1 mg/hr respectively which give a ratio of approximately 1. This is within the expected range.

6.5.2 Flow Induced Removal Aspect of the Model (MRR_{flow})

In the analytical model the cyclic vibration-driven acceleration of the fluid between the tool and the workpiece generates flow-induced removal, MRR_{flow}. Flow-induced removal is the combined effect of three individual removal mechanisms; the viscous-shear-driven removal, MRR_S, the suction/blow driven removal, MRR_P, and the inertia driven removal, MRR_I. However analysis shows that the first two mechanisms dominate the inertia-driven removal and thereby MRR_{flow} correspond to the following sum:

$$MRR_{flow} = c_1 MRR_S + c_2 MRR_P \qquad (6\text{-}22)$$

Where,

$$MRR_P \propto \sqrt{\frac{A}{d_o}}\omega \text{ and } MRR_S \propto \sqrt{\frac{A}{l_p}}\omega \qquad (6\text{-}23)$$

where d_o represent the estimated gap thickness between tool and workpiece,l_p represents the lateral spacing between embedded abrasives, andω and A are the frequency and amplitude of the vibration. Combining equations 6-22 and 6-23 the flow induced removal becomes,

$$MRR_{flow} \propto \left(\sqrt{\frac{A}{d_o}} + \sqrt{\frac{A}{l_p}}\right)\omega \qquad (6\text{-}24)$$

From equation 6-24 the ratio of flow induced removal between soft and hard tool is

$$\frac{(MRR_{flow})_{soft}}{(MRR_{flow})_{hard}} = \frac{\left(\sqrt{\frac{1}{d_{os}}} + \sqrt{\frac{1}{l_{ps}}}\right)}{\left(\sqrt{\frac{1}{d_{oh}}} + \sqrt{\frac{1}{l_{ph}}}\right)} = \frac{\sqrt{d_{oh}l_{ph}}\left(\sqrt{d_{os}} + \sqrt{l_{ps}}\right)}{\sqrt{d_{os}l_{ps}}\left(\sqrt{d_{oh}} + \sqrt{l_{ph}}\right)} \qquad (6\text{-}25)$$

The AFM roughness value,R_q, of the tool roughness at the tool surfaces are used to approximate the gap thickness, whereby d_o is approximated as $3R_q$. For soft and hard tools the corresponding d_o values are, $d_{os} = 3 \times 66$ nmand $d_{oh} = 3 \times 112$ nm. The SEM image analysis estimated the lateral distance between two particles for both soft and hard tools (l_{ps} andl_{ph}). The values are presented in Table 6-2.

Putting all the values into equation 6-25, provides the approximate ratio of expected for the MRR_{flow} component:

$$\frac{(MRR_{flow})_{soft}}{(MRR_{flow})_{hard}} = \frac{\sqrt{3\times112\times26}\left(\sqrt{3\times66} + \sqrt{10}\right)}{\sqrt{3\times66\times10}\left(\sqrt{3\times112} + \sqrt{26}\right)} \sim 1.55 \qquad (6\text{-}26)$$

Table 6-4details values of the MRR_{flow} term obtained from experiments on both hard and soft tools, while also showing the calculated MRR_{flow} ratios at each test condition. The ratio of experimentally obtained MRR_{flow} values lies between 1.4 and 2.07. This is comparable to the theoretically predicted approximate ratio of 1.55 in equation 6-26.

Table 6-4: Experimental flow induced removal ratio between soft and hard tools

Frequency (Hz)	MRR_{total}, (mg/hr)		$MRR_{flow} = MRR_{total} - MRR^{*}_{cm}$ (mg/hr)		Ratio = $\frac{(MRR_{flow})_{soft}}{(MRR_{flow})_{hard}}$
	Soft Tool	Hard Tool	Soft Tool	Hard Tool	
500	2.93	2.5	0.83	0.4	2.07
5500	4.1	3.53	2	1.43	1.40
8000	5.27	4.33	3.17	2.23	1.42

* MRR_{cm} ($\approx$ 2.1 mg/hr) is taken as the removal at no vibrational input, i.e. the 'y' axis intercepts for all tests in Figure 6-7.

6.6 Conclusions and Discussion

MRRs of fused silica obtained by polishing with hard and soft tools are compared. A similar MRR trend was noted for both pitch grades whereby higher vibrational powers resulted in higher MRRs. At any vibrational power input, the removal rate obtained with a soft tool is higher than that obtained with a hard tool. The difference is more significant at higher vibrational frequencies. At a higher vibrational input frequency (>500 Hz) a140% higher flow induced removal rate was obtained using the soft tool (Table 6-4).Soft tools produced better surface finishes as when compared to that achieved with a hard tool. Up to 200% difference is observed in the lower spatial roughness (SWLI 2.5×) values.SEM and AFM evaluations of the tool surfaces provided insights in to the difference between the abrasive crusts formed on hard and soft tools, and found more particles (over 30% more).Material property differences between hard and soft tools can be incorporated into Keanini's model, with the alteration providing reasonable predictions with respect to the MRR expect with the different tools. Each segment of total removal rate, MRR_{cm} and MRR_{flow}, individually comply with the experimental results.

CHAPTER 7: VIBRATION ADDED FROM EXTERNAL SOURCES

Most of the published research on vibration assisted polishing processes utilizes high frequency (> 20 kHz) ultrasonic vibrations with amplitudes greater than one micron to enhance the polishing outcomes [126 - 135]. However, it has been shown that low amplitude vibrations (< 10 nm) up to 16 kHz can have significant impact on the material removal obtained during pitch polishing process [Chapter 4]. Polishing on two machines with identical process parameters but significantly different vibrational content resulted in different polishing outcomes [Chapter 4, 172]. Further investigations revealed an approximate linear relationship between the removal rate and nominal vibrational power input [Chapter 5], where higher input powers produce higher removal rates. This chapter considers the power input associated with two different polishing machines, and investigates the possibility of applying external vibration sources to the polishing process so as to induce higher removal rates.

7.1 Vibrational Power versus Removal Rate from Previous Test

In case of polishing on the test-bed with single frequency input vibrations (chapter 5), the nominal vibrational power input, W (Watt = Nm/s) was approximated by eqn. 1.

$$W = \text{force (mg)} \times \text{displacement(fA)} = mgfA \qquad (7\text{-}1)$$

Where m is the applied load, g is gravity, and f and Aare the frequency and amplitude of the input vibration. The product f×A represents the displacement of workpiece in unit time. However on an actual polishing machine the workpiece is

subjected to vibrations across multiple frequencies and the total displacement is considered to be the summation of all the individual displacements ($\sum f_i A_i$). The Fourier Transform (FT) of measured accelerometer output provides information on the frequency and amplitude content within the frequency bandwidth. Thereby the input power for a polishing machine within the frequency range 10 to16 kHz can be calculated by equation 7-2.

$$\dot{W} = mg \sum_{f=10\ Hz}^{16k\ Hz} f_i A_i \qquad (7-2)$$

Applying equation 7-2 to previously collected data enables power values to be calculated for the polishing machines detailed in chapter 4 when using two different pitch tools (tools A1 and A2). The results are summarized in Table 7-1. The corresponding removal rates are also presented in the same table. Figure 7-1graphically presents the data listed in Table 7-1. Referring to the material removal model outlined in chapter 5 and presented in Appendix F, the total removal, MRR_{tot}, is described by the following equation:

$$MRR_{tot} = MRR_{cm} + MRR_{flow} \qquad (7\text{-}3)$$

According to the model the chemical-mechanical removal component, MRR_{cm}, is insensitive to vibrations while the flow mediated removal, MRR_{flow}, is sensitive to vibrations. In Figure 7-1a the y axis intercept represents the MRR_{cm}term and is determined to be 5.92 and 4.8 mg/hr for tool A1 and A2 respectively. The MRR_{cm} and MRR_{flow} term are also presented in Table 7-1.Figure 7-1b illustrates the input power versus the MRR_{flow} component.

Table 7-1: Vibrational powers and corresponding removals for tests in chapters 4.

Vibrational power of actual polishing test in Chalper 4, $\dot{W} = mg \sum_{f=10\,Hz}^{16k\,Hz} fA$				Total removal rates from chapter 4, $MRR_{tot} = MRR_{cm} + MRR_{flow}$ (mg/hr)			
FT measured for different Tools and Polishing Machines		Power, Nm/s	Stdev*	MRR_{tot}	MRR_{cm} (Fig. 7-1a)	MRR_{flow}	Stdev*
Tool A1	Machine 1	0.2	0.03	9.67	5.92	3.75	0.97
	Machine 2	0.07	0.009	7.23		1.31	0.31
Tool A2	Machine 1	0.17	0.035	8.4	4.8	3.6	0.26
	Machine 2	0.06	0.015	6.07		1.27	0.4

*Standard deviation for three separate measurements.

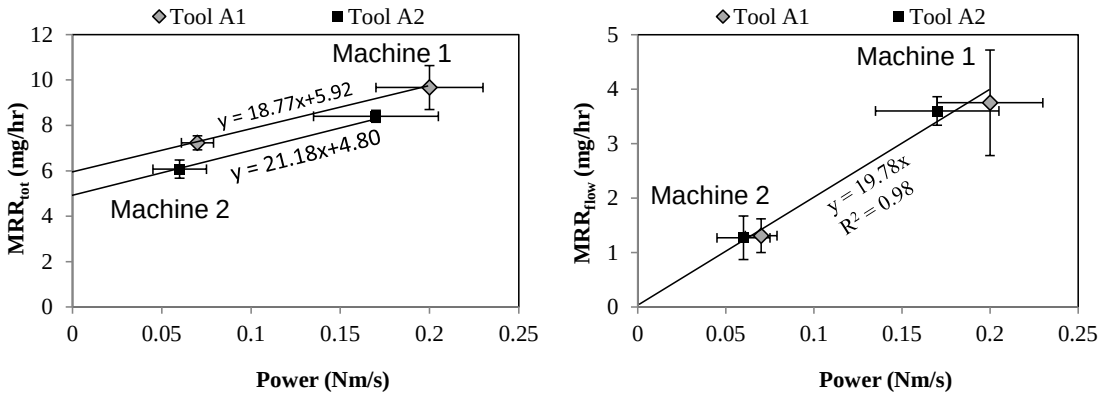

a b

Figure 7-1: a. MRR_{tot} b. MRR_{flow} versus power input for two different tools on the two polishing machines.

The high R^2 value (0.98) of the best fit line through all data points in Figure 7-1b strongly supports that the MRR_{flow} term is proportional to the input power. Thereby equation 7-3 becomes

$$MRR_{tot} = MRR_{cm} + c \times \text{Vibrational power} \qquad (7\text{-}4)$$

where c is constant and can be determined from experimental test results. Following from these results it is not unreasonable to propose a polishing system where external vibrational sources could be attached to the polishing system to increase the power input and hence the material removal rates.

7.2 Addition of External Vibrations

There are a number of possible ways to induce vibrations in a polishing tool, such as using a shaker table, piezoelectric vibrating disc, or using a mechanical unbalanced motor attached to the underside of the tool. In the case of smooth polishing (nm – roughness) the desired amplitude of the excitation should be very low (nm – μm level) while the frequency should be such to produce certain input power from the nm level of vibration amplitude. To impart additional vibrations the research utilized a low cost system consisting of high speed (11 and 13krpm) unbalanced motors, which usually find application in mobile phone. The next sections analyze the feasibility of using these unbalanced motors to impart additional vibrations to the platen to increase the process vibration and thereby the removal rates on fused silica samples.

7.2.1 Design and Implementations/Characterization

Four high speed DC motors were obtained, three 3 volt motors (Ø ≈ 6 mm Radio Shack model number: 273-047), and one 9 volt motor (Ø ≈ 15 mm Radio Shack model number: 273-107). The smaller motors came with a 0.5 g eccentric mass attached to the spindle, while for the larger motor a 4 g eccentric mass was prepared and attached to the spindle. The small motors can run at ≈ 13 krpm, while the larger motor can run at ≈ 11 krpm and the unbalanced rotating mass generates the required vibrations. Each motor is securely fixed to an aluminum holder that was glued to either the polishing tool platen or

the workpiece holder depending on the test conditions. The three small motors were connected in series to a 9 volt battery, while the larger motor was connected to a separate 9 volt battery. The use of batteries allows the motors to be attached to the rotating platen without consideration to wiring concerns.

The extent of vibrations existing at the tool surface were investigated under three different conditions, 1) under normal operating conditions with no external vibration sources, 2) all four motors are placed on the underside of the polishing platen, and 3) the larger motor remains on the underside and while the other three are placed on the workpiece holder. Figure 7-2 provides the schematic of condition 2 and condition 3 while Figure 7-3is a photograph of condition 2.The natural frequency of the tool platen and the workpiece holder were evaluated using SolidWorks simulation, FFEPlus Solid Mesh iterative solver [173]. The results in Table 7-2corresponding to the first five frequency mode shapes [106].

Table 7-2: Natural frequencies of tool platen and workpiece holder.

Parameters	Steel Tool Platen					Aluminum Workpiece Holder				
Mode Shape	1	2	3	4	5	1	2	3	4	5
Natural Frequency, kHz	0.57	0.66	0.67	1.3	1.59	4.6	6.2	6.5	9.95	13.75

Since the frequencies of the smaller and larger motors (0.22 and 0.18 kHz respectively) are much lower than the natural frequency of the tool and workpiece holder, the arrangement of vibrators relative to each other will not significantly impact the vibration generation. However for uniformity, the three smaller motors were arranged with equal distribution (120˚ apart) at 2/3rd of the radius from the center, for both tool and workpiece holder. While the larger motor was placed at 2/3 of the tool radius in

between two of the smaller motors and remained in this position for both test conditions2 and 3.‘Normal operating’ conditions were those detailed in chapter 4 for the fused silica polishing test; platen speed = 20 rpm, over-arm sweep = 5 rpm and polishing load = 10 N (see Table 4-4).

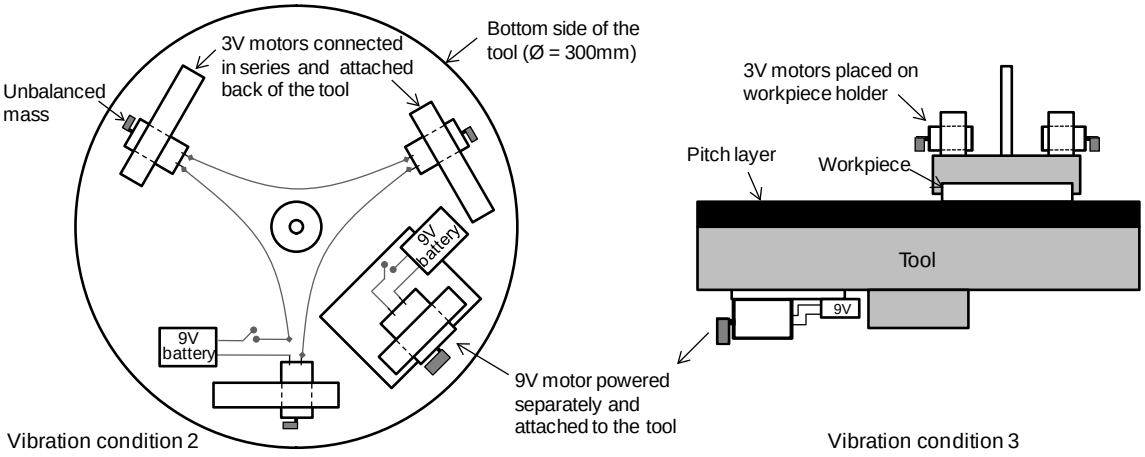

Figure 7-2: Schematic of condition 2 and 3; 9V motor fixed at bottom for both the conditions while 3V motors switched from tool to workpiece.

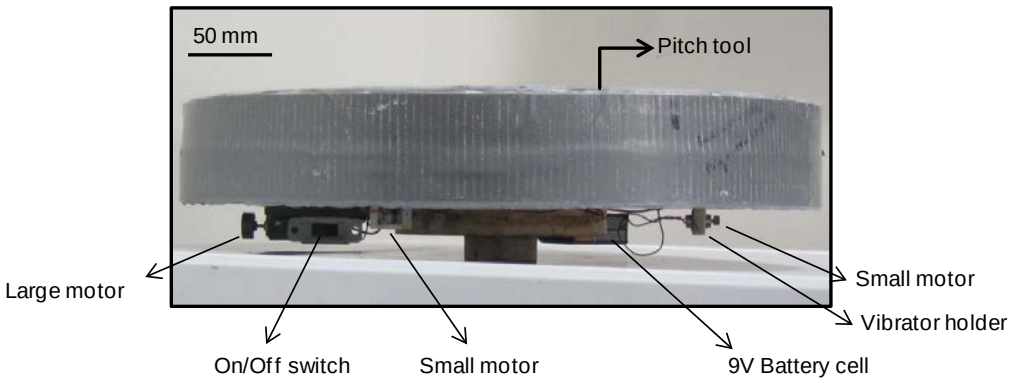

Figure 7-3: Picture of condition 2, the vibrators attached to the bottom of the substrate (Tool A3).

An accelerometer mounted onto the top of the tool surface measured the vibrations occurring under each set of conditions. The FT of the accelerometer signal provided the frequency and amplitude content of the measured vibrations, see chapter 4

for details on vibration measurements. The FTs for the three conditions are plotted in Figure 7-4. The corresponding power inputs determined by equation 7-2 are also reported in Figure 7-4.

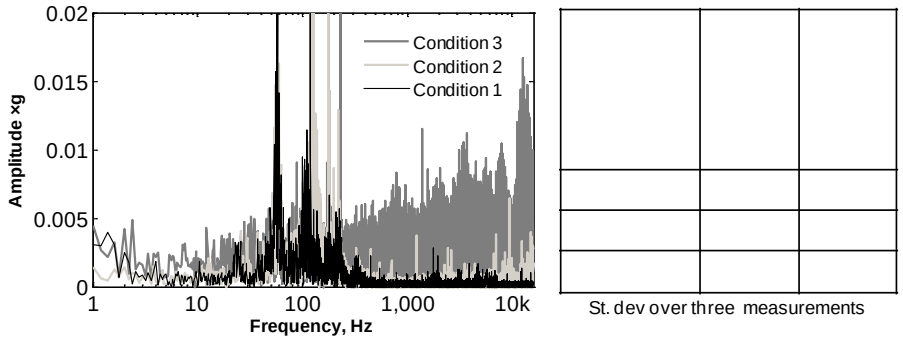

Figure 7-4: FTs of the measured vibrations on Machine 2 using tool A3. (g= 9.81 m/s^2) and calculated power at three conditions.

As the polishing platen consists of a 16 kg steel substrate coated with a 25 mm thick layer of Acculap™Soft pitch the external vibration sources make minimal impact when attached to the underside of the platen, increasing the power input from 0.07 W (no excitation) to 0.12 W, with over 90% of the power increase attributed to the three smaller motors (three smaller motor separately run to estimate their contribution). Attachment of the motors to the workpiece holder (a 3kg Aluminum block with a polyurethane liner) increased the power input to the tool surface up to 0.22 W. In this arrangement the larger motor on the underside of the plate has minimal (<5%) contribution to the power increase.

7.3 Polishing Test and Result Analysis

Fused silica samples were polished under all three vibrational conditions listed in Figure 7-4. The tool named A3 is the same tool as A1 used in chapter 4, however since the time lapsed between tests was over six months and the tool was extensively

reconditioned before reusing, the tool is renamed as A3. The process consumables are similar to those detailed in chapter 4.Figure 7-5a details the material removal rates obtained on Machine 2 with the different power inputs. The slope of the best fit line through the data (m= 20.3) is similar to the slopes obtained using tools A1 (m=18.8) and A2 (m=21.2) on polishing Machines 1 and 2, see Figure 7-1a. The y axis intercept represents the MRR_{cm}component which is 3.05 mg/hr. Figure 7-5b plots the MRR_{flow}component along with the equivalent data for tools A1 and A2 (seen in Figure 7-1b). The addition of the three extra data points induces minor changes to the slope (m=19.8 increases to m=20) and the R^2 value (0.98 versus 0.87) which further emphasizes the correlation between the power input and the material removal rates, $MRR_{tot} = MRR_{cm} + c \times$ Vibrational power.

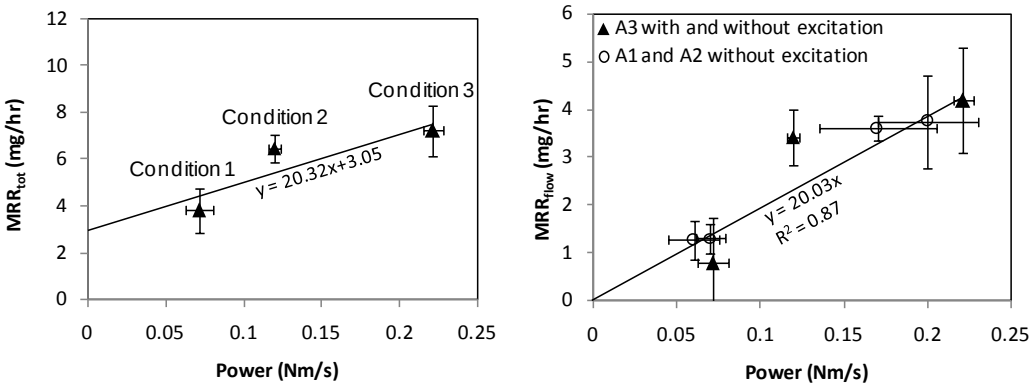

a b

Figure 7-5: a. MRR_{tot} versus power inputs for three conditions plotted in Figure 7-4, b. MRR_{flow} for A1, A2 and A3.

The surface roughness values of the workpieces are also evaluated before and after each of the polishing test. A scanning white light interferometer (Zygo NewView5000) is used to measure the surface roughness for low (2.5×) and high (50×) spatial resolutions. Figure 7-6a and b depict the average surface roughness values and

associated standard deviations before and after polishing test for three different conditions.

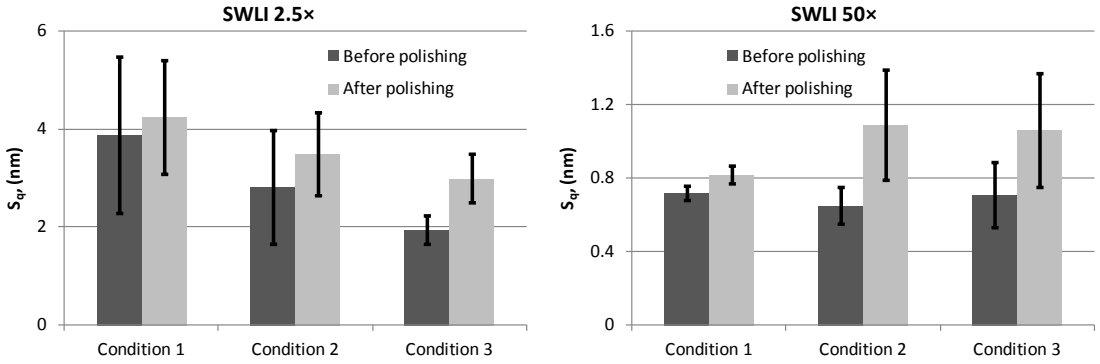

a b

Figure 7-6: a. SWLI 2.5× and b. SWLI 50× RMS surface roughness values for three conditions Figure 7-4.

For both the 2.5× and 50× roughness values, two significant trends are observed; 1) for each of the conditions the one hour polishing operation slightly increased the roughness values, with increases being larger when the external vibration sources are activated, 2) comparing condition 2 and 3, where the external vibrations sources are activated, the polished samples have comparable final surface roughness values even though there was a 85% difference in the power input and 12% increase in MRRs. Although for most of the conditions the roughness values error bars overlap between the before and after polishing results, the external vibration sources can potentially deteriorate the final surface finish quality. Further investigation required to ascertain if this negative impact on finish can be overcome by additional polishing step with the external sources turned off.

7.4 Summary and Discussion

Small, low cost, battery operated, high speed unbalanced motors generating lower frequency vibrations (<20 kHz) were used to impart nanometer level vibrations into the polishing system. These additional vibrations induced up to an 80% increase in the material removal rate. This increased removal rates does result in higher surface roughness values. This offers new opportunities for those involved in polishing optical materials to increase their productivity and throughput.

These results suggest that the analytic model, which correlates the input vibrational power to material removal rate, (outlined in chapter 5 and provided in Appendix F) is also applicable in the case where external vibrational sources are used to increase the power input. The data in Figure 7-5supports the linearity of the relationship between power input and material removal rates irrespective of the power input sources.

CHAPTER 8: CONCLUSIONS AND FUTURE WORK

Throughout this dissertation, the experimentally based research intends to explore the role of vibrational dynamics in pitch polishing process by investigating the correlation between process vibrations and polishing outcomes such as material removal rates and surface finish. While the literature studies support the preposition that vibrations affect the polishing outcomes, this dissertation strongly answered some follow up questions and identified new thoughts for future work. This chapter summarizes the conclusions, discusses the findings and ends up by highlighting future work areas.

8.1 Conclusions

The main findings of the dissertation summarized below:

Polishing system vibrations were measured in the 1 Hz to 16 kHz range and were found to have amplitudes ranging from several nanometers at lower frequencies down to several Angstroms that the higher end of the frequency bandwidth. Factors found to affect the vibrational response of the system include; the polishing machine itself, process speeds, and tool construction.

Fused silica polishing tests were conducted on two different machines and with two different tool constructions. The tool–machine combination with the highest vibrational content (power input) produced higher material removal rates (30%) than that of the lower power input combination.

The higher level vibrations were also found to have a negative impact on the surface finishes obtained in the lower spatial domains. The PSD analysis of the polished surfaces at lower spatial domain indicated that the lower frequency response of the machines is responsible for deteriorate the lower spatial frequency roughness values.

A test bed was designed and fabricated (Figure 5-1) that facilitated a more controlled investigation into the role of process vibrations on the material removal rates. Multiple polishing tests carried out under a wide range of vibration frequencies and amplitudes, demonstrated that up to a limit a linear correlation exists between the power input and the material removal rate. In this case the limit was controlled by the vibrational amplitude, i.e. above 10 microns a decrease in the material removal rate was observed. This was attributed to a possible separation between the tool and the workpiece. The effect of increase the frequency above 8 kHz was not investigated (limited by the shaker table).

Methods of altering the process vibrations were presented; vibration attenuation was achieved through the addition of a layer of cork in the tool construction, and amplified by the addition of external vibrational sources to the machine. As expected higher material removal rates (80%, see Figure 7-5) were achieved when vibration amplification was implemented.

Limited dynamic testing of pitch samples and tools indicate that while different grades of pitch have different dynamic properties, they do not provide significant process vibration attenuation or amplification. The tests also indicate that the response of the polishing tool is dominated by the metal substrate used in polishing tool fabrication over the choice of pitch used to coat the tool.

The experimental results provided the basis for a new combined contact-fluid dynamics based model developed by Dr. Keanini that considers both nano-scale tool topography and thin film fluid flow components.

Extensive analytical analysis considering the surface topography of hard and soft pitch tools demonstrated that Dr. Keanini's model can be take tool changes into consideration.

8.2 Future Work

There are many areas of this research that can be extended in the future. The future work is branched up into two broad parts; process monitoring and control, and further investigations into how to minimize the potential degradation of the surface finish with increasing vibrational power input.

8.2.1 Process Monitoring and Control

The research has clearly demonstrated that there is a correlation between process vibrations and polishing outcomes. This offers the potential to introduce fairly simple process control to the workshop floor. Accelerometers could be mounted to the polishing machine and over time the vibrational response of the machine could be mapped to the process outcomes. This would enable the user to develop an optimal process control window. Deviations outside of the window would alert the users to potential issues and shorten trouble shooting time frames.

Similarly the vibrational response of many machines within a facility can be compared to each other and characteristics of the 'good' polishing systems quantified. This may provide suggestions on how to alter lower performing polishing systems, i.e.

adjust the driving belt, greasing or replacing the gear box, change the tool substrate material, optimize the tool running speed etc.

Opportunities also exist to alter existing vibrational characteristics by addition of external vibration source. A simple turn on turn off product can be developed such as unbalance mass motor system (as used in chapter 7), piezoelectric vibrating pad etc. so that in can be attached to a polishing system to amplify the vibrations and there by optimize the polishing outcomes. The knowledge can incorporate in machine or tool design to obtain optimal process vibration.

8.2.2 Surface Finish Aspects

While the work demonstrated that the material removal rate increases with vibrational power input, it also indicated that the lower spatial frequency roughness values can deteriorate. Further works is required to better isolate the factors affecting the surface roughness quality, i.e. is it just the presence of the additional vibrations or does poor tooling management and/or lack of precision polishing expertise play a role. As the polishing tests performed for this research considered mainly the roughness of the part and not the part form, it would be of interest to determine if the same surface roughness values would be obtained should the parts be polished by an expert, i.e. under optimal tooling conditions and process kinematics. If the same trends are observed, then it would be of interest to determine the length of additional polishing time required under lower vibrational power conditions to reverse any negative impacts of polishing with additional vibrations, i.e. is the overall combined polishing time shorter than polishing without inducing any additional vibrations within the process.

In chapter 4 the PSD analysis performed is based on sub-aperture measurements with a field of view of 2.2 mm × 2.4 mm, it is realized that the measurements should be expanded further to include larger areas, i.e. full-aperture measurements, so as to better understand the impact of vibration on low spatial roughness values.

REFERENCES

1. I. Newton, “Opticks”, Reprint of the 4th edition. 104, 1931.

2. B. E. Gillman, F. Tinker “Fun facts about pitch and the pitfalls of ignorance” SPIE 3782:72-79, 1999.

3. S. Sutton, “Development of new synthetic optical polishing pitches”, OSA Technical Digest Series Optical Society of America, 2004.

4. W. N. Findley, J. S. Lai, K. Onaran “Creep and relaxation of nonlinear viscoelastic materials”, Introduction to linear viscoelasticity, 1976.

5. A. J. Leistner, “Fabrication and testing of precision spheres”, Metrologia, 28: 503-506, 1992.

6. C. Brecher, M. Esser, S. Witt, “Interaction of Manufacturing Process and Machine tool”, Annals of the CIRP 58 (2):588-607, 2009.

7. B. Mullany, S. Turner, “Optical Polishing Pitches: Impact Frequency Responses and Indentation Depths”. Appl. Opt. 49(3):442- 449, 2010.

8. F. W. Preston, “The theory and design of plate glass polishing machines”, J. Soc. Glass Technol. 11, 214–256, 1927.

9. T. Izumitani, “Polishing rate of optical glass”, Paper TuB-A1, Tech. Digest, Topical Meeting on the Science of Polishing, Optical Society of America, 17 April 1984.

10. T. Izumitani, S. Harada, S Adachi, “Polishing mechanism of optical glass”, Journal of Japan Society of Lubrication Engineering, Vol. 33 Issue 4 (p267-273), 1988 (Technical report HGW-0-3E, Hoya Glass Works 1971).

11. N. J. Brown, “Optical polishing pitch” Preprint of a paper prepared for submission to the Optical Society of America workshop on Optical Fabrication and Testing. San Mateo, CA, preprint UCRL 80031, 1977.

12. L. M. Cook, “Chemical processes in glass polishing”, Journal of Non-Crystalline Solids 120:152-171, 1990.

13. C. Evans, E. Paul, D. Dornfeld, D. A. Lucca, G. Byrne, M. Tricard, F, Klocke, O. Dambon, B. A. Mullany, “Material removal mechanisms in lapping and polishing”, Annals of the CIRP 52(2):611-633, 2003.

14. J. E. DeGroote, A. E. Marino, J. P. Wilson, A. L. Bishop, J. C. Lambropoulos, and S. D. Jacobs, "Removal rate model for magnetorheological finishing of glass" APPLIED OPTICS, Vol. 46, No. 32. 10 November 2007.

15. F. Vega, N. Lupon, J. A. Cebrian, F. Laguarta, “Laser application for optical glass polishing,” Optical Engineering. 37(1): 272-279, 1998.

16. Y. Namba, H. Tsuwa, "Ultra-Precision Float Polishing Machine", Annals of the CIRP, Vol 36/1, 1987.

17. S. R. Wilson, J. R. Mcneil, “Neutral ion beam figuring of large optical surfaces”, Proc. SPIE 818: 320-324, 1987.

18. W. J. Rupp, “Conventional optical polishing techniques”, Optica Acta. 18(1): 1-16, 1971.

19. H. Jing, X. Qiao, L.X. Yang, Z. L. Shu, Z. Q. Hua, W. Jian, “Removal function of computerized numerical controlled chemical polishing based on the Marangoni interface effect,” High Power Laser and Particle Beams, 17(4): 555-558, 2005.

20. J. N. Desai, "Advances and Processes in Precision Glass Polishing Techniques" M.Sc. Thesis, University of Florida, 2009.

21. G. W. Wang, "Small Pitch Tool for Removing Middle Spatial Frequency Errors", Key Engineering Materials, Volume 552, 2013.

22. A. E. Amin, "Fluid Jet Polishing of Glass Material", MSc Thesis, Blekinge Institute of Technology, Karlskrona, Sweden, 2013.

23. Y. F. Xing, “Study on the technology of the ultra-precision machining for the large-aperture optical flats,” Optical Technique. 30(1): 27-29, 2004.

24. “Factor Influencing Material Removal and Surface Finish of the Polishing of Silica Glass”, M.Sc. Thesis by A C Landis, University of North Carolina at Charlotte, 2006.

25. A. A. Tesar, B. A. Fuchs, and P. Paul Hed, “Examination of the polished surface character of fused silica” APPLIED OPTICS / Vol. 31, No. 34 / 1 December 1992.

26. W. Silvernail, Paper WB1-1, Tech. Digest, Topical Meeting on Optical Fabrication and Technology, OSA, 1982.

27. A. Kaller. “Neuere Erkenntnisseuber die VorgangebeimPolieren des Glases”, Mschr. Feinmech, Opt. 79, p135, 1962.

28. Available at- http://www.optimaxsi.com/PDFs/SurfaceRoughnessRevA.pdf

29. J. R. Harvey, A. Kotha, “Scattering effects from residual optical fabrication errors”, Proc. SPIE, 2576, pp.155-174, 1995.

30. A. J. Leistner, E. G. Thwaite, F. Lesha, and J. M. Bennett, N. Belkhira, D. Bouzida, V. Herold "Polishing study using Teflon and pitch laps to produce flat and super smooth surfaces" Applied Optics, Vol. 31, No. 10, 1992.

31. M. J. Cumbo, D. Fairhurst, S.D. Jacobs and B. E. Puchebner "Slurry particle size evolution during the polishing of optical glass" LLE Review, University of Rochester, Volume 61, Page 25-39, 1994.

32. C. J. Walsh, J. A. J. Leistner, J. Seckold, B. F. Oreb, and D. I. Farrant, "Fabrication and measurement of optics for the Laser Interferometer Gravitational Wave Observatory" Vol. 38, No. 13 y APPLIED OPTICS, May 1999.

33. T. I. Suratwala, P. E. Miller, P. R. Ehrmann, and R. A. Steele, "Polishing Slurry Induced Surface Haze on Phosphate Laser Glasses" Journal of Non-Crystalline Solids, March 1, 2004.

34. A. A. Elshwain M. Sc. Thesis, “A Study of Lapping Parameters to Reduce Polishing Time of Optical Glass”, Universiti Teknologi Malaysia, 2007.

35. N. Belkhira, D. Bouzida, V. Herold "Correlation between the surface quality and the abrasive grains wear in optical glass lapping", Tribology International 40, 498–502, 2007.

36. T. V. Vorburger, “Measurements of Roughness of Very Smooth Surfaces”, Annals of CIRP, 36/2: 503-509, 1987.

37. P. M. Lonardo, H. Trumpold, L. D. Chiffre, “Progress in 3D Surface Microtopography Characterization”, Annals of CIRP, 45/2: 589-598, 1996.

38. R. Komanduri, D. A. Lucca, and Y. Tani, “Technological advances in fine abrasive processes” Annals of the CIRP 46(2):545-596, 1997.

39. O. Sakata, A. Nikulin, H. Hashizume, “XRay Evaluation of Microroughness of Mechanochemically Polished Silicon Surfaces”, Japan. Journal of Appl. Phys., 32: L616-L619, 1993.

40. L. D. Chiffre, H. N. Hansen, A. Bronstein, “Investigation on the Surface Topography in Polishing Using Atomic Force Microscopy”, Annals of CIRP, 45/1: 523-528, 1996.

41. D. J. Whitehouse, “Handbook of Surface Metrology”, Inst. of Physics, Bristol, UK, 1994.

42. D J Whitehouse, "Surface metrology" Meas. Sci. Technol. 8 955, 1997.

43. D. Golini, and S.D. Jacobs, "Physics of loose abrasive microgrinding", Appl. Opt. 30, 2761-2777, 1991.

44. Y. Ahn, N. Cho, S. Lee and D. Lee, "Lateral crack in abrasive wear of brittle materials" JSME Int. J. Series A 46, 140-144, 2003.

45. Y. P. Chang, M. Hashimura, and D. A. Dornfeld, "An investigation of material removal mechanisms in lapping with grain size transition" J. Manuf. Sci. Eng. 122, 413-419, 2000.

46. R. M. Wood, “Laser-induced damage of optical materials” Institute of Physics publishing series in optics and optoelectronics, Bristol and Philadelphia, 2003.

47. H. Campbell, "Damage resistant optical glasses for high power lasers: A continuing glass science and technology challenge" UCRL-JC-149843, 2002.

48. P. E. Miller, T. I. Suratwala, L.L. Wong, M.D. Feit, J.A. Menapace, P.J. Davis, and R.A. Steele, "The distribution of subsurface damage in fused silica" Proc. SPIE 5991, 599101, 2005.

49. T. Suratwala, L. Wong, P. Miller, M. D. Feit, J. Menapace, R. Steele, P. Davis et al., "Sub-surface mechanical damage distributions during grinding of fused silica" J. Non-Crystal. Solids 352, 5601-5617, 2006.

50. Z. Wang, Y. Wu, Y. Dai, and S. Li, "Subsurface damage distribution in the lapping process" Appl. Opt. 47, 1417-1426, 2008.

51. P. P. Hed, and D.F. Edwards, "Relationship between surface roughness and subsurface damage’’ Appl. Opt. 26, 4677-4680, 1987.

52. Y. Li, J. Hou, Q. Xu, J. Wang, W. Yang and Y. Guo, "The characteristics of optics polished with a polyurethane pad" Opt. Express 16, 10285-10293, 2008.

53. “A Novel Fluorescence Based Method of Assessing Subsurface Damage in Optical Materials” PhD Dissertation by Wesley. B. Williams, University of North Carolina at Charlotte, 2009.

54. W. Williams, B.A. Mullany, W.C. Parker, P. Moyer, and M. H. Randles, ‘’Using quantum dots to evaluate subsurface damage depths and formation mechanisms in glass’’ CIRP Annals- Manuf. Technol. 59, 569-572, 2010.

55. J. Wang, Y. Li, J. Han, Q. Xu, Y. Guo "Evaluating subsurface damage in optical glasses" Journal of the European Optical Society - Rapid Publications 6, 11001, 2011.

56. https://www.salemdist.com/precision/pdf/tech/polish/e_Pitch/TECH_ACCULAP.pdf.

57. M. Mainuddin, B. Mullany, "Vibration Attenuation in optical pitch," ASPE 25th annual meeting, Atlanta, GA, USA, October, 2010.

58. B. Mullany, M. Mainuddin, E. Browy "CAREER: An Innovative Look at Precision Polishing", NSF CMMI Research and Innovation Conference, Atlanta, GA 2011.

59. F. Twyman “Prism and Lens Making”, Hilger Watts, 1952.

60. J. E. DeGroote, S.D. Jacobs, L.L. Gregg, A.E. Marino, J.C. Hayes, "Quantitative Characterization of Optical Polishing Pitch", Proceedings of SPIE Vol. 4451, 2001.

61. B. Mullany, E Corcoran "An Innovative Look at Precision Polishing Tools", Proceedings of the 3rd CIRP International Conference on High Performance Cutting, Dublin, Ireland, June 12-13, ISBN 978-1-905254-32-3, pp 589-598, 2008.

62. B. Mullany, E Corcoran, “New Metrics for Polishing Pitch”, Topical Meeting of the Optical Fabrication & Testing (OF&T) Topical Meeting, Rochester, NY, Oct 2008.

63. B. Mullany, E. Corcoran, “Frequency response of polishing pitch samples”, Technical Digest, Optifab 2009, Rochester, TD06-04, May 2009.

64. B. Mullany, J. Beaman. “The Response of Pitch to Higher Frequency Vibrations”. Topical Meeting of the Optical Fabrication & Testing (OF&T). Jackson Hole, WY, OThB5, June 2010.

65. V. L. Streeter, E. B. Wylie “Fluid Mechanics”, First SI metric edition, (1983).

66. S. Timoshenko “Strength of materials” Part-I, Krieger Pub Co. ISBN: 0898746213, 1980.

67. R. S. Lakes Viscoelastic Solids, CRC Press, 1999.

68. R. D. Sudduth, "Evaluation of the Characteristics of a Viscoelastic Material from Creep Analysis Using the Universal Viscoelastic Model. I. Isolation of the Elastic Component Designated as the “Projected Elastic Limit”", Journal of Applied Polymer Science, Vol. 89, 2923–2936, 2003.

69. Meller Optics Inc., Online: http://www.melleroptics.com.

70. Available at-http:// www.asterism.org/ tutorials/tut43%20 Making %20A%20 Mirror % 20 Polishing %20 Tool.pdf

71. The Amateur Telescope Making (ATM's) Workshop, Online at-http://www.atm-workshop.com/pitch-lap.html.

72. http://home.comcast.net/~kevin.mccarthy137/Pitchlaps/instruct.html.

73. https://stellafane.org/tm/atm/polish/pour-lap.html.

74. T.S. Izumitani, Optical Glass, English Translation from American Institute of Physics, New York, NY: 1-3, 1986.

75. Corning 7940 fused silica, courtesy of L. Sutton, Corning Inc. Canton. NY 13617.

76. Schott BK7 (borosilicate crown) and Schott SF6 (dense flint), courtesy of A. Marker. Schott Glass Technologies Inc., Duryea, PA 18642.

77. H. Bach, N. Neuroth, "The Properties of Optical Glass" Second Corrected Printing, ISBN 3-540-58357-2, 1998.

78. S. G. Quartz, Spectrosil® Optical Fused Silica, Technical Publication MAR 06-GR-A4-EN, March 2006.

79. Saint-Gobain Quartz, June 2005, Fused Quartz & Fused Silica, Material Properties Data Sheet, Technical Publication JUN 05-GR-A4-EN.

80. "Corning Premium-Quality Fused Silica Low Expansion Material Code 7940." Corning Inc., Corning, NY 14830.

81. W. L. Silvernail, N. J. Goetzinger, "Use of Rare Earths in Glass Polishing" AEC, Tech Inf Cent (CONF-730402-P2), p 652-661, 1973.

82. H. H. Karow, “Fabrication Methods for Precision Optics” John Wiley & Sons, Inc. New York, 1993.

83. W. H. Lowdermilk, D. Milam, "Laser-induced surface and coating damage," IEEE J. Quantum Electron. QE-17, 1888- 1903, 1981.

84. A. A. Tesar and B. A. Fuchs "Removal rates of fused silica with cerium oxide/pitch polishing" SPIE Vol. 1531 Advanced Optical Manufacturing and Testing 11, 1991.

85. M. Mogensen, N. M. Sammes, and G. A. Tompsett. "Physical, chemical and electrochemical properties of pure and doped ceria", Solid State Ionics 129(1), 63, 2000.

86. B. T. Kilbourn, “Cerium, A guide to its role in chemical technology, Molycorp, Inc. White Plains NY, 1992.

87. Lord Rayleigh, "Polish," Trans. Opt. Soc., 19(1): 38-47, 1917.

88. G. T. Beilby, “Aggression and Flow of Solids”, Macmillan, London, Sec. V p. 81, 1921.

89. H. Yoshikawa, “Brittle-Ductile Behavior of Crystal Surface in Finishing”, Journal of JSPE, 35: 662-667, 1967.

90. Leal-Cabrera, I. and A. Cordero-Davila, "Analytical and numerical classification of wear profiles produced with different-shape oscillating tools". Opt. Eng., 48: 103401-1-103401-9, 2009.

91. M. Buijs and K. Korpel-van Houten, “A model for lapping of glass,” J. Mater. Sci. 28, 3014–3020, 1993.

92. G. Fu, A. Chandra, S. Guha, and G. Subhash “A Plasticity-Based Model of Material Removal in Chemical–Mechanical Polishing (CMP)” IEEE Transaction on Semiconductor Manufacturing, Vol. 14, No. 4, 2001.

93. M. Nogami and M. Tomozawa, "Effect of stress on water diffusion in silica glass", J. Amer. Ceram. Soc., vol. 67, no. 2, pp. 151–154, 1984.

94. T. Izumitani, “Polishing lapping and diamond grinding of optical glasses,” in Treatise on Materials Science and Technology, M. Tomozawa and R. H. Doremus, Eds. New York: Academic, vol. 17, pp. 115–172, 1979.

95. T. Izumitani and S. Harada, “Polishing mechanism of optical glasses,” Glass Technol. 12, 131–135, 1971.

96. D. Cornish and L. Watt, Br. Sci. Instr. Res. Assoc. Rep. R295, 1963.

97. W. Silvernail and N Goetzinger, Glass Ind. 52, 130, 1971.

98. M. J. Cumbo, “Chemo-mechanical interactions in optical polishing,” Ph.D. dissertation, University of Rochester, 1993.

99. K. B. Doyle "Design Strength of Optical Glass", Proceedings of SPIE - The International Society for Optical Engineering, Vol. 5176, p 14-25, 2003.

100. Y. Shu, Y. Dai, Z. Zheng, S. Li, "The Ultra-Precision Polishing of Large Aperture Reaction Bonded Silicon Carbide Mirror" American Journal of Nanotechnology 1 (2): 45-50, 2010.

101. F. Grieser, R. N. Lamb, G. R. Wiese, D. E. Yates, R. Cooper, and T. W. Healy, "Thermal and radiation control of the electrical double layer properties of silica and glass," Radiat Phys. Chem. 23, 43-48, 1984.

102. A. A. Tesar, N. Brown, J. R. Taylor, and C. J. Stolz, "Subsurface polishing damage of fused silica: nature and effect on damage threshold of coated surfaces" Laser-Induced Damage in Optical Materials, 1990.

103. H. E. Bennett, L. L. Chase, A. H. Guenther, B. Newman, and M. J. Soileau, “Laser Induced Damage in Optical Material”, Proc. Soc. Photo-Opt. Instrum. Eng. 1441, 154-172, 1990.

104. A. A. Tesar et al. "Subsurface polishing damage of fused silica" Proc. Opt Mat High power laser SPIE, Vol. 1441, 1990.

105. Y. Liu, Z. You, “Simulation of cyclic loading tests for asphalt mixtures using user defined models within discrete element method”, Proceedings of Sessions of Geo Congress 2008 – Geo Congress 2008: Characterization, Monitoring, and Modeling of Geo Systems, n 179, pp 742-749, 2008.

106. D. J. Inman, “Engineering Vibration” Prentice Hall, 1994.

107. J. H. Harlow "Electric power transformer engineering" CRC Press, ISBN 978-0-8493-1704-0.2004.

108. A. J. Leistner “Teflon polishers: Their manufacture and use” Appl. Opt. 15(2) 1976.

109. H. Shan, C. Wei, X. Xu, H. He, S. Liu, Y. Li, K Yi, and J. Shao, "Effect of Polishing Plane Vibration on Large-Size Optical Workpieces in Continuous Polishing", Proc. of SPIE Vol. 8884, 2013.

110. S. Yin, T. Shinmura, "A comparative study: Polishing Characteristics and its Mechanisms of three Vibration modes in Vibration-assisted Magnetic Abrasive Polishing", Int. Journal of Machine Tools and Manf 44, 383-390, 2004.

111. E. Brinksmeier, O. Riemer, H. Schulte, "Material removal mechanisms in abrasive vibration polishing of complex molds" Proc. of SPIE Vol. 7655 765502-1, 2010.

112. B. Mullany, M. Mainuddin, W. Williams, and R. Keanini "An experimental and analytical investigation into the effects of process vibrations on material removal rates during polishing", J. Appl. Phys. 113, 224902, 2013.

113. W. Lin, S. K. Chee, H. Suzuki, T. Higuchi, "Polishing Characteristics of a Low Frequency Vibration Assisted Polishing Method", Advanced Materials Research, Volume 797, 2013.

114. F. J. Shiou, H. S. Ciou, "Ultra-precision surface finish of the hardened stainless mold steel using vibration-assisted ball polishing process", International Journal of Machine Tools & Manufacture 48, 721–732, 2008.

115. S. K. Chee, H. Suzuki, M. Okada, T. Yano, T. Higuchi, W. Lin, "Precision Polishing of Micro Mold by Using Piezoelectric Actuator Incorporated with Mechanical Amplitude Magnified Mechanism", Advanced Materials Research, Volume 325, 2011.

116. S. K. Chee, H. Suzuki, J. Uehara, T. Yano, T Higuchi, W. Lin "A Low Contact Force Polishing System for Micro Molds that Utilizes 2-Dimensional Low Frequency Vibrations (2DLFV) with Piezoelectric Actuators (PZT) and a Mechanical Transformer Mechanism", Int. J. of Automation TechnologyVol.7No.1, 2013.

117. S. K. Chee, H. Suzuki, J. Uehara, T. Yano, T. Higuchi "Preliminary Studies for Precision Polishing of Micro Structured Mold by Using Three-Dimensional Low Frequency Vibration Utilizing Piezoelectric Actuator Incorporated with Mechanical Amplitude Magnified Mechanism", Advanced Materials Research, Volume 565, 2012.

118. J. Guo, H. Suzuki, T. Higuchi, "Development of micro polishing system using a magnetostrictive vibrating polisher", Precision Engineering 37, 81– 87, 2013.

119. J. Guo, S. Morita, M. Hara, Y. Yamagata, T. Higuchi, "Ultra-precision finishing of micro-aspheric mold using a magnetostrictive vibrating polisher", CIRP Annals - Manufacturing Technology 61, 371–374, 2012.

120. Y. Li, Y. Wu, L. Zhou, M. Fujimoto, "Vibration-assisted dry polishing of fused silica using a fixed-abrasive polisher" International Journal of Machine Tools & Manufacture 77, 93–102, 2014.

121. Y. Li, Y. B. Wu, L. Zhou, H. Guo, J. Cao, M. Fujimoto, M. Kemmochi, "Investigation into Chemo-Mechanical Fixed Abrasive Polishing of Fused Silica with the Assistance of Ultrasonic Vibration", Key Engineering Materials, Volumes 523 - 524, 2012.

122. Y. Li, Y. Wu, J. Wang, Q. Xu, W. Yang, Y. Guo "Precision Manufacturing of Fused Silica Glass by Combining Bound-Abrasive Polishing with Ultrasonic Vibration" , Proc. of SPIE Vol. 8416, 841606, 2012.

123. Y. Li, Y. Wu, J. Wang, W. Yang, Y. Guo, Q. Xu, "Tentative investigation towards precision polishing of optical components with ultrasonically vibrating bound-abrasive pellets", OPTICS EXPRESS, Vol. 20, No. 1, 2012.

124. M. P. Mandina, Patent assignee “Optimax System, Inc, Ontario, NY”, Patent No.: US 6,942,554 B1, Sep 13, 2005.

125. N. Kobayashi, Y. Wu, M. Nomura, T. Sato, "Precision treatment of silicon wafer edge utilizing ultrasonically assisted polishing technique", journal of materials processing technology 2 0 1, 531–535, 2008.

126. H. Suzuki, S. Hamada, T. Okino, M. Kondo, Y. Yamagata, T. Higuchi "Ultraprecision finishing of micro-aspheric surface by ultrasonic two-axis vibration assisted polishing" CIRP Annals - Manufacturing Technology 59 347–350, 2010.

127. H. Wang, F. Zhang, H. Zhao, D. Luan, Y. Chen, "Study on Optical polishing of optical glass by means of ultrasonic magnetorheological compound finishing", Proc. of SPIE Vol. 6722 67221P-1, 2007.

128. W. Xu, X. Lu, Guoshun Pan, Yuanzhong Lei, Jianbin Luo "Ultrasonic flexural vibration assisted chemical mechanical polishing for sapphire substrate" Applied Surface Science 256 3936–3940, 2010.

129. W. Xu, X. Lu, G. Pan, Y. Lei, J. Luo, “Effects of the ultrasonic flexural vibration on the interaction between the abrasive particles; pad and sapphire substrate during chemical mechanical polishing (CMP)” Applied Surface Science 257 2905–2911, 2011.

130. E.J. Weller, "Nontraditional Machining Processes", Society of Manufacturing Engineering, Dearborn, Michigan, USA, 1983.

131. M. Y. Tsai, W. Z. Yang, "Combined ultrasonic vibration and chemical mechanical polishing of copper substrates", International JournalofMachineTools&Manufacture53, 69–76, 2012.

132. H. Suzuki, T. Moriwaki, T. Okino, Y. Ando "Development of Ultrasonic Vibration Assisted Polishing Machine for Micro Aspheric Die and Mold" Department of Mechanical Engineering, Kobe University, Rokkodai, Nada, Kobe, Japan. Techn. 55/1, 385, 2006.

133. U.S. Kim, J. W. Park, "Vibration-assisted Electrochemical Polishing for Extremely Smooth Surface Generation", Advanced Material Research, Vol. 813, p475-478, 2013.

134. W. Xu, X. Lu, G. Pan, J. Luo, and C. Zhang, “Experimental Study of Ultrasonic Vibration Assisted Chemical Mechanical Polishing for Sapphire Substrate” , Advanced Tribology, edited by J. Luo, Y. Meng, S. Tianmin, and Q. Zhao, p. 464, Springer, Berlin, 2010.

135. J. DeGroote, B. Light, D. Savage, B. Wiederhold, and M. Mandina, “VIBE™ finishing to remove mid-spatial frequency ripple” International Optical Design Conference and Optical Fabrication and Testing, OSA Technical Digest (CD) (Optical Society of America), paper OWE2, 2010.

136. J. Xu, A Murakami, T Shigematsu, "Development of a Novel Vibration Polishing Method for Fiber Protrusion in Multi-fiber Connectors", Compiled from Trans. JSME, Category-C, Vol.67, No.662, pp3317~3322, 2001

137. W.J. Tomlinson, N. Kalitsounakis, G. Vekinis, “Cavitation Erosion of Aluminas” Ceram. Int. 25, 331, 1998.

138. T. J. C. V. Terwisga, P. A. Fitzsimmons, L. Ziru and E. J. Foeth "Cavitation Erosion – A review of physical mechanisms and erosion risk models" Proceedings

of the 7th International Symposium on Cavitation– Paper No. 41, Ann Arbor, Michigan, USA, August 17-22, 2009.

139. Z. Li “Assessment of Cavitation Erosion with a Multiphase Reynolds-Averaged Narier-Stokes Method” PhD thesis, Delf University of Technology, 2012.

140. R. Shen, J. Zhong, “Ultrasonic Applied in Super Precision polishing of Magnetic Recording Heads”, Proceedings of the 8th International Conference on Electronic Packaging Technology—ICEPT 07, 454, 2007.

141. G. Amza, G. Dumitrescu, A. Petrescu, “Contribution of Ultrasonic Finishing Process Modeling Lens of Optical Devices Using Finite Element Analysis”, Proceedings of the 3rd WSEAS Int. Conference on FINITE DIFFERENCE-FINITE ELEMENT-FINITE VOLUME-BOUNDARY ELEMENTS, April 20-22 168-173, 2010.

142. Y. S. Liao, Y.P. Yu, C.W. Huang, "Ultrasonic Vibration Assisted Mechanical Chemical Polishing (MCP) of Silicon Carbide", Advanced Materials Research, Volume 565, 2012.

143. H. Hocheng, K.L. Kuo, “Fundamental Study of ultrasonic polishing of mold steel” International Journal of Machine Tools & Manufacture,” 42 7- 13, 2002.

144. M. T. Cuberes, “Ultrasonic Machining at the Nanometer Scale” Journal of Physics: Conference Series 61 219-223, 2007.

145. F. Dinelli, S. K. Biswas, G. A. D. Briggs, and O. V. Kolosov, “Ultrasound induced lubricity in microscopic contact” Applied Physics Letters / Volume 71 / Issue 9 Appl. Phys. Lett. 71, 1177, 1997.

146. A. R. Jones and J. B. Hull, “Ultrasonic flow polishing” Ultrasonics 36, 97, 1998.

147. Z. G. Huang, Z.N. Guo, X. Chen, Z.Q. Yu, T.M. Yu, W.B. Lee, “Microscopic Mechanism of Polishing Based on Vibration of Liquid”, Nanotechnology 18, 2007. doi:10.1088/0957-4484/18/10/105703.

148. H. Y. Tam, H. B. Chenga, Y.W. Wang “Removal rate and surface roughness in the lapping and polishing of RB-SiC optical components”, Journal of Materials Processing Technology 192–193, 276–280, 2007.

149. J. E. DeGroote Nelson, B. Light, D. Savage, B. Wiederhold and M. Mandina "VIBE™ finishing to remove mid-spatial frequency ripple" OSA / IODC/OF&T 2010.

150. C. Klinger, "Vibe: A new process for high speed polishing of optical elements," in Optifab, pp. Z: 1-4, SPIE, Rochester, NY, 2007.

151. Z. Liang, Y. Wu, X. Wang, W. Zhao, “A new two-dimensional ultrasonic assisted grinding method and its fundamental performance in monocrystal silicon machining”, International Journal of Machine Tools and Manufacture. 50 728–736, 2010.

152. J. P. Choi, B.H. Jeon, B.H.Kim, “Chemical-assisted ultrasonic machining of glass”, Journal of Materials Processing Technology 191, 153–156, 2007.

153. D. M. Aikens, J. E. DeGroote, R. N. Youngworth "Specification and Control of Mid-Spatial Frequency Wavefront Errors in Optical Systems" OSA/FiO/LS/META/OF&T, 2008.

154. M. Konyo, A. Yoshida, S. Tadokoro, N. Saiwaki, "A Tactile Synthesis Method Using Multiple Frequency Vibrations for Representing Virtual Touch", IEEE/RSJ International Conference on Intelligent Robots and Systems, 2005.

155. J. Kim, D. Lee, K. Lee, “The Effect of Dynamic Characteristics on the Surface Texture in Mirror Grinding”, Int. Adv Manuf Technol, 27: 274-280, 2005.

156. H. Kato, A. Uetake, “Generation of chatter marks in surface grinding by using horizontal spindle-reciprocation table type machine”, Bull Japan Soc Eng 19(4):266–272, 1985.

157. T. Hoshi, S. Matsumoto, S. Mitsui, O. Horiuchi. “Suppression of wheel regenerative grinding vibration by alternating wheel speed”. Ann CIRP 35(1):231–234, 1986.

158. M. Alfares, A. Elsharkawy “Effect of Grinding Forces on the Vibration of Grinding Machine Spindle System”, International Journal of Machine Tools & Manufacture 40, 2003-2030, 2000.

159. P. Chen, W. Qu, M. H. Miller, A. Chandra "Thermal Effects in Vibration Assisted Grinding" Proc. of the ASPE Annual Meeting, pp. 86-89, 2000.

160. J. Akbari, H. Borzoie, M. H. Mamduhi, “Study of Ultrasonic Vibration Effect on Grinding Process of Alumina Ceramic (Al2O3),” World Academy Science, Engineering and Technology 41, 2008.

161. Y. Wu, B. Zhao, X. S. Zhu, “Modeling of Material Removal in Workpiece Lateral Ultrasonic Vibration Grinding of Fine-crystalline Zirconia Ceramics”, Key Engineering Materials, Vol. 315-316, 304-308, 2006.

162. R.S. Hahn, “Vibration problems and solutions in grinding”, ASTME paper no. MR69-246, 1969.

163. R.A. Thompson, “The character of regenerative chatter in cylindrical grinding”, Transactions of ASME Journal of Engineering Industry 858–864, August 1993.

164. S. Ohno, Self-excited vibration in cylindrical grinding, part 1 and 2, Bulletin of the JSME 13, 616–623, 1970.

165. G. Bi, Y. Guo, K. Pan, C. Jiang, “Effect of Grinding Wheel Vibration on Surface Quality of Axisymmetric Aspheric Lens” Advanced Material Research. Vol 97-101, 2111-2114, 2010.

166. A. Sohn, L. Lamonds, K. Garrard, "Modeling of Vibration in Single-Point Diamond Turning", Proceedings of the 21st Annual ASPE Meeting, ASPE 2006.

167. G. P. Prihandana, M. Mahardika, M. Hamdi, K Mitsui, "Effect of low-frequency vibration on workpiece in EDM processes", Journal of Mechanical Science and Technology 25 (5), 1231-1234, 2011.

168. http://www.physics.udel.edu/~jim/PHYS211Spring2012/Class%20Notes/Class_14.pdf. (Access on January 2013).

169. http://www.mathworks.com/help/images/examples/granulometry-of-snowflakes.html. (Access on May 2012).

170. http://windows.microsoft.com/en-us/windows7/products/features/paint.

171. A. R. S. Marcal "Alternative Methods for Counting Overlapping Grains in Digital Images", ICIAR 2008, LNCS 5112, pp. 1051–1060, Springer-Verlag Berlin Heidelberg, 2008.

172. B. Mullany, M. Mainuddin, “The Influence of Process Vibrations on Precision Polishing Metrics”, Annals of the CIRP, 61/1/2012, 555-558, 2012.

173. J. E. Akin "Finite Element Analysis Concepts: via SolidWorks", Hackensack, NJ : World Scientific, ISBN 9789814313018 2010.

174. http://www.utwente.nl/tnw/onderwijs/practica_tnw/doc/apparatuur/diversen/bruel_kjaer_shaker_type_4809.pdf. (Access on January 2011).

175. K. L. Johnson, Contact Mechanics, Cambridge University Press, 1985.

176. J. A. Greenwood and J. B. P. Williamson, "Contact of Nominally Flat Surfaces", Proc. R. Soc. London Ser. A 295(1442), 300 1966.

177. J. P. Hsu and A. Nacu, "An experimental study on the rheological properties of aqueous ceria dispersions", J. Colloid Interface Sci. 274, 277 2004.

178. F. A. Morrison, 'Understanding Rheology', Oxford, 2001.

179. D. Quemada, P. Flawed, and J. H. Jezequel, Chem. Eng. Commun. 32, 61, 1985.

180. I. Finnie, “Erosion of Surfaces by Solid Particles”, Wear, 3: 87-1 03, 1960.

181. X. C. de Lega and P. J. de Groot, "Lateral resolution and instrument transfer function as criteria for selecting surface metrology instruments", Imaging and Applied Optics Technical Digest, OSA 2012.

182. http://www.hoskin.qc.ca/uploadpdf/Instrumentation/Taylor%20Hobson/hoskin_Talysurf%20Series%20PGI_44abfcf218426.pdf (Access on July 2014).

183. http://www.zygo.com/?sup=/resource/manuals.cgi?type=newview (Access on July 2014.)

APPENDIX A: VIBRATIONAL TRANSMISSION AND Q FACTORS

Before the swept test, the natural frequency of the sample tool platen was evaluated utilizing finite element simulation (FFEPlus solver) in SolidWorks. The frequency modes were set to 7 and the results are presented in Table A-1.

Table A-1: Frequency mode and corresponding natural frequency of sample tool platen (6 mm thick aluminum platen with diameter, Ø = 50 mm).

Frequency Modes	1	2	3	4	5	6	7
Natural Frequency, kHz	5.3	5.6	5.6	8.7	11.7	11.7	24.4

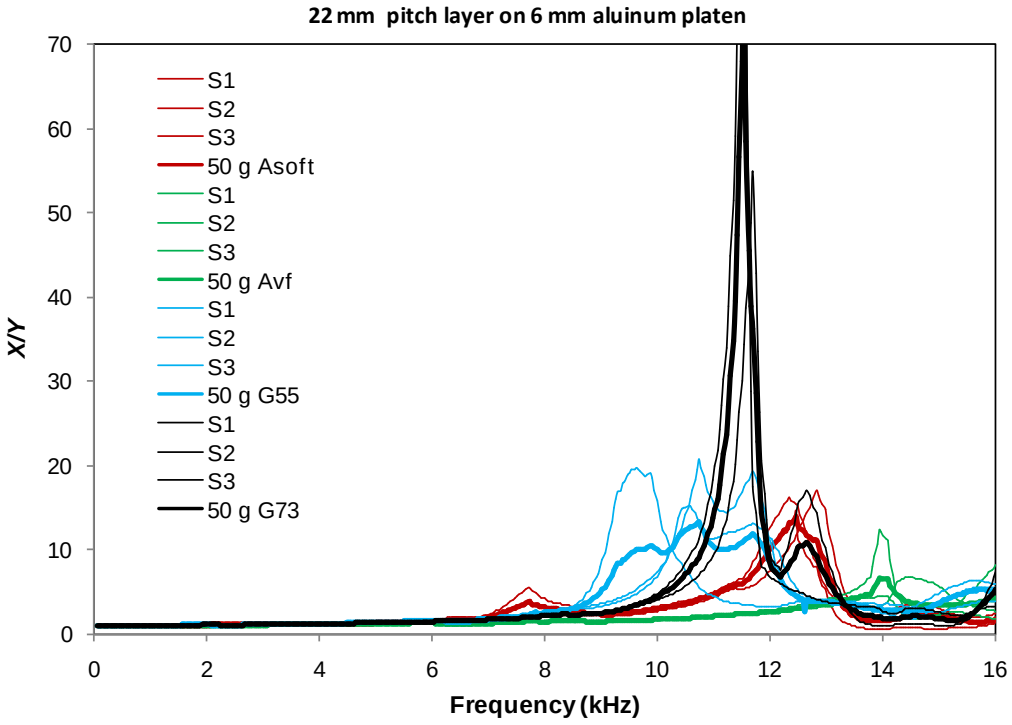

Figure A- 1: Frequency sweep test, red (Asoft) and green (Avf) are synthetic while blue (G55) and black (G73) is natural.

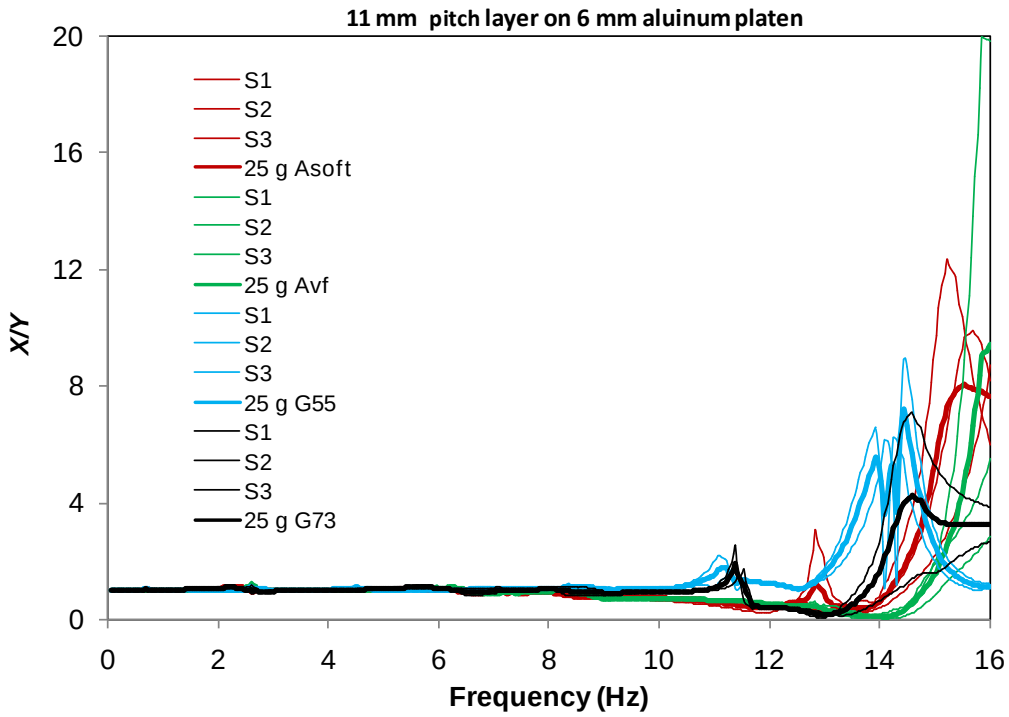

Figure A-2: Frequency sweep test, red (Asoft) and green (Avf) are synthetic while blue (G55) and black (G73) is natural.

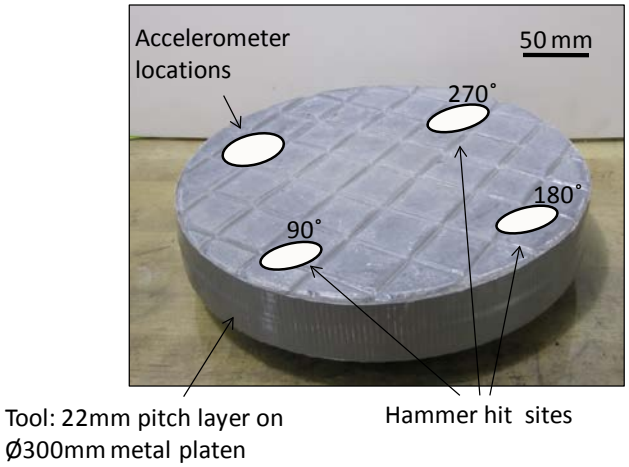

Figure A-3: Impact test hammer hitting location

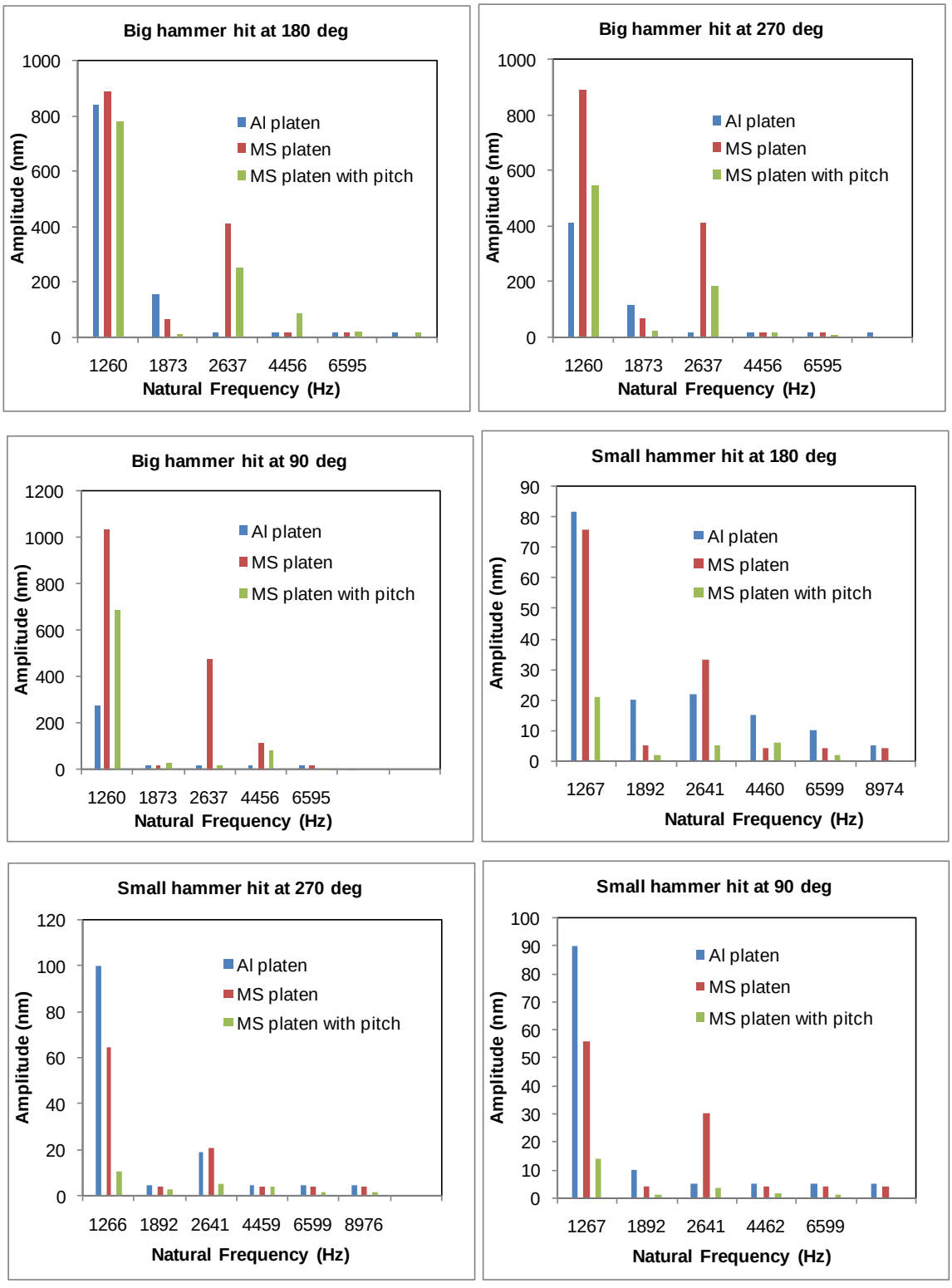

Figure A-4: Corresponding natural frequencies for different platen material and tool.

Q Factor or Quality Factor

The quality factor or Q factor is a dimensionless parameter that describes damping of an oscillator relative to its center frequency [107]. Higher Q value indicates a lower damping system i.e. the oscillations die out more slowly. That's why a parameter termed as 'inverse quality factor', Q^{-1} [106] is used to quantify the damping of vibrational transmission. Higher Q^{-1} value indicates higher damping system. For a response curve as illustrated in Figure A-5, the Q factor can be calculated from equation A-1 [106].

$$\mathbf{Q} = \frac{\textbf{Resonance frequency}}{\textbf{Half-power frequency bandwidth}} = \frac{\mathbf{f_3}}{(\mathbf{f_2}-\mathbf{f_1})} \qquad \text{(A-1)}$$

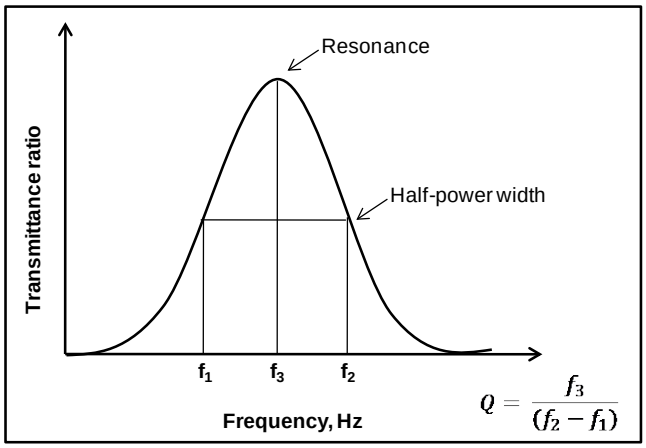

Figure A-5: Q factor calculation for a typical response, higher Q^{-1} means higher attenuation.

APPENDIX B: MATLAB CODE FOR PSD CALCULATION, PSD.M

```
clc;
fid1 = fopen('25I2.txt','r'); % open the file (fid is a file id)
pts1 = fscanf(fid1, '%g %g',[2,inf]);
status = fclose(fid1);         % close the file.
N=length (pts1);               % sample number
Fs = N/max(pts1(1,:));         %N/scan length = sampling

%psd with ft
ydft = ft(pts1(2,:));
ydft = ydft(1:N/2+1);
psdx = (1/(Fs*N)).*abs(ydft).^2;
psdx(2:end-1) = 2*psdx(2:end-1); % default rectangular window
q = 0:Fs/N:Fs/2;

plot(q,psdx);
%plot(q,10*log10(psdx));     % to make y axis logarithmic

xlabel('Frequency, mm^-^1')
ylabel('nm^2.mm^2')
title('PSD of SEM image')

%f = fopen('output1.xls', 'w');
f = fopen('output.txt', 'w');
fprintf(f, '%g \n', psdx);
fclose(f);
```

APPENDIX C: RELATIVE VELOCITY BETWEEN TOOL AND WORKPIECE

For a fixed polishing speed (tool × over-arm = 20×5) the relative speed between tool and workpiece varies as the workpiece travels over the tool radius, see Figure C-1. The workpiece was set to travel back and forth between 40 mm and 120 mm of tool radius. The corresponding relative velocities between tool and workpiece over the radius are modeled in Figure C-2.

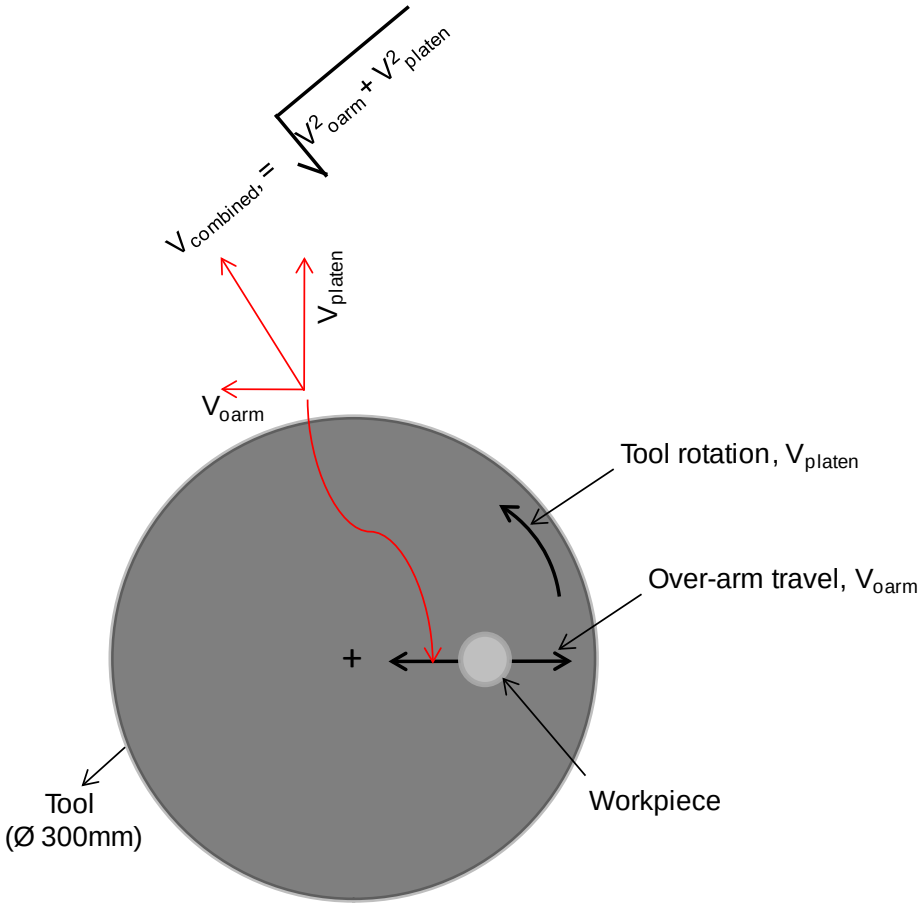

Figure C-1: Schematic of relative velocity calculation between tool and workpiece

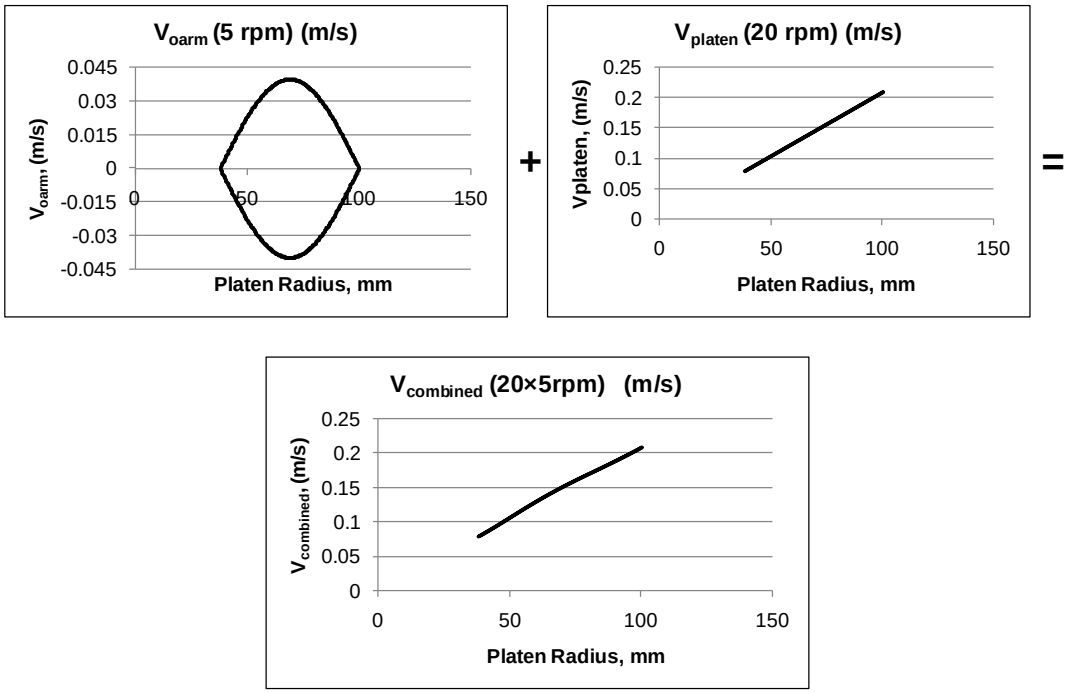

Figure C-2: Velocities of platen, over-arm and combined of both.

Table C-1: Maximum and minimum relative velocities between tool and workpiece from $V_{combined}$.

Relative velocity between tool and workpiece*		
v_{min} = 0.08 m/s	v_{max} = 0.2 m/s	$v_{average}$ = 0.15 m/s

*Considering workpiece fixed with over-arm and not rotating with its own axis.

APPENDIX D: SSD EVALUATION BY DR. WESLEY WILLIAMS

Characterization of vibration-induced subsurface damage: Two samples, which were polished on Machine 1, and two samples which were polished on Machine 2, were exposed to a hydrofluoric acid (8%) etch. Approximately 0.4 µm of material was etched away (based on mass loss), revealing defects - scratches, chatter marks, and pits - consistent with subsurface damage. The level of subsurface damage in the individual specimens was quantified by sampling 36 locations (a 6×6 array) on each etched surface, under an Olympus BX51 optical microscope, and by recording a 850 µm × 660 µm micrograph at 10× magnification. The images were converted to grayscale, with each pixel being represented by an 8-bit integer. A quadratic surface (in two directions) was then fit to the data, after excluding points with grayscale values less than or equal to 140;the latter were seen to correspond to obvious scratches and pits. The fit surface was then subtracted from the original data set, and the standard deviation of the pixel values between the fit and actual surface was calculated. The fit surface and standard deviation were then compared to the original data set (no pixels excluded), and any pixel whose grayscale value deviated from the surface fit by more than three standard deviations was classified as a defect. Qualitatively, this algorithm identified defects that were visible to the human eye in the micrographs, without producing false positives in noisier regions of the images.

Analysis of images from the samples polished on Machine 1 and Machine 2 exhibited a great deal of image-to-image variability in the number of pixels at which defects were detected. Figure D-1 depicts a histogram which bins the number of pixels detecting damage, versus the number of image sample locations having any given pixel-

level degree of damage. Figure D-2 shows example surface images exhibiting low and high levels of SSD. The least damaged sample images exhibited a 0.09% degree of pixel-level damage, while the most damaged samples exhibited a 1.2% degree of damage. [The degree of damage in any given sample is defined as the number of pixels detecting SSD, divided by the total number of pixels in the image.] These results were not unexpected, as defect sites were uncommon and were distributed across the surface, showing up in some fields of view and being absent in others. No significant difference in damage count was observed for samples polished on Machine 1 versus Machine 2; standard deviations were such that more detailed trends could not be extracted.

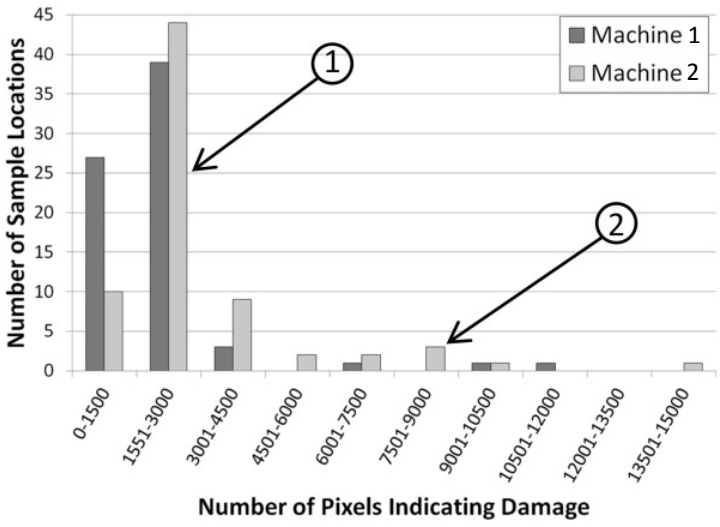

Figure D-1: Distribution of damage levels for Machine 1 and Machine 2. Note 72 surface images generated on Machine 1 were examined, similarly for Machine 2. Representative images from values indicated by detail 1 and 2 are shown in Figure D-2.

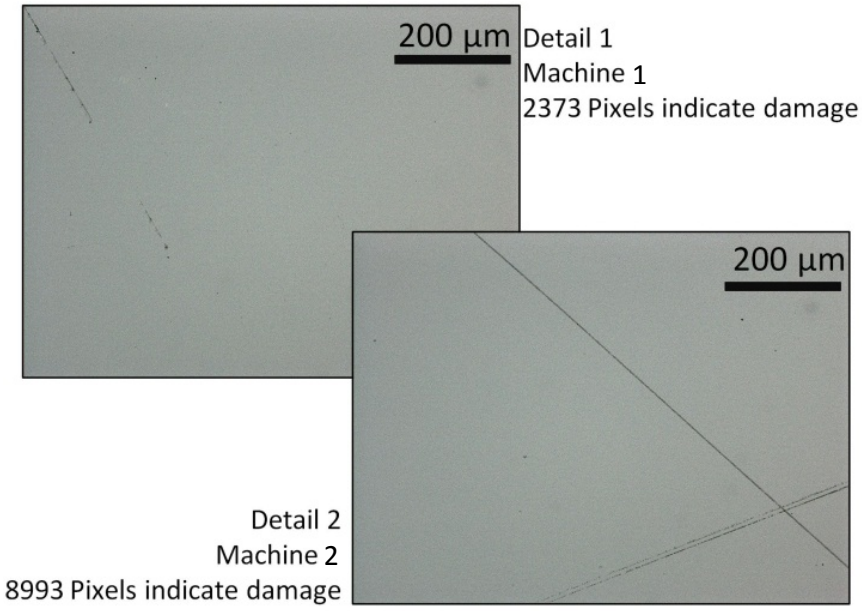

Figure D-2:10× micrographs of samples representative of damage levels indicated in Detail 1 and Detail 2 in Figure D-1.

These simple experiments clearly indicate that even minute levels of vibration can significantly increase achievable MRRs, while producing little to no effect on surface and subsurface quality. In order to better understand the role of vibration on material removal, a test apparatus was constructed which allowed control of both vibration frequency and amplitude during polishing. A description of the experimental system and presentation of the experimental results obtained are detailed in the next two sections.

APPENDIX E: PHASE CALCULATION BY XCORRFUNCTION.M

```
fid = fopen('5µm@500Hz1.txt','r');   % open the file (fid is a file id)
pts = fscanf(fid, '%g %g %g', [3,inf]);
p1=pts';
status = fclose(fid);              % close the file.

[B,A]= BUTTER (2, 5/25000, 'high');  %filtering accls
pts1 = filter (B,A,p1);

[C,D]= BUTTER (2, 50/25000, 'high');  %filtering CapGage
pts2 = filter (C,D,p1(:,3));

disptGlass =1e6*(pts1(:,1)*960.615)/(2*3.14*500)^2; %1e6* for micron
disptTool =1e6*(pts1(:,2)*912.400)/(2*3.14*500)^2;
Gap = pts2*2.5;

x= 1/50000:1/50000:5;
plot (x,disptTool,x,disptGlass,x,(disptTool-disptGlass))
%first column is w/p (acclm 17), 2nd column is tool (acclm 41)

xlabel('Second')
ylabel('Displacement and Gap, µm')
title('Workpiece displacements relative to the tool displacements, 5Micron@500Hz')

%PhaseDifference between tool and glass (not given write values)
i=1;
n=1;
while (n < 250000)
if pts1(n,1)*pts1(n+1,1) < 0.00       %glass phase
T1(1,i) = n*2e-5;
i=i+1;
      n=n+30;
end
   n=n+1;
end
j=1;
n=1;
while (n < 250000)
if pts1(n,2)*pts1(n+1,2) < 0.00
T2(1,j) = n*2e-5;          %tool phase
j=j+1;
      n=n+30;
```

```
end
   n=n+1;
end

sum = 0.0;
for n = 4000:1:4500
T(1,n)= abs (T1(1,n)-T2(1,n));
sum = sum + T(1,n);
end

AvgPhase = sum/500
Stdev = std(T)
```

APPENDIX F: DR. KEANINI'S EMPERICAL MODELS

The results presented in Figure 5-10and Figure 5-11, corresponding to the small-amplitude limit of vibration-assisted polishing, are first considered. In this limit, roughly corresponding to A≲ 1.6 μmand 500 Hz≤f≤8000 Hz, contact between the tool and workpiece is both fluid- and solid-mediated, with the load being shared by pitch-embedded abrasive particlesand a thin, entrapped fluid layer. Abrasive-workpiece contact is assumed Hertzian, and the film thickness, based on local AFM measurements of the pitch surface, is assumed to be on the order of $3\times R_q \approx 200$ nm. In this limit, workpiece material removal occurs by the combined action of chemical-mechanical removal, produced by relative motion between the workpiece and contacting tool asperities, and flow-mediated removal, driven by vibrational acceleration of the slurry film between the tool and workpiece.

Analysis of material removal in the large-amplitude limit, corresponding roughly to $A \geq 5\ \mu$m and$500\ \text{Hz} \leq f \leq 8000\ \text{Hz}$, and yielding the data shown in Figure 5-13,is presented in Sec. K below. In contrast to the small-amplitude limit, it is argued - based on data in Table 5-4and on surface roughness measurements - that when$A \geq 5\ \mu$m, the tool and workpiece remain out of contact, separated by a relatively thick slurry film. Importantly, in this limit, material removal is thus strictly flow-mediated. Note, from this point on, the term 'gap' refers to the slurry-filled space separating the tool and workpiece. As indicated by Figure 6-3and as supported by AFM data, the gap space is densely interpenetrated by tool-embedded polishing abrasives, a large fraction of which are in elastic contact with the workpiece. Thus, the gap space is filled with both slurry and fixed, interpenetrating polishing abrasives.

A. Combined Chemical-mechanical and Flow-induced Removal: Small Amplitude Limit

With regard to the small-amplitude limit, three principal results are presented:

1) The important question concerning the sensitivity of Cook's [12] chemical-mechanical material removal mechanism, MRR_{cm},to low-amplitude vibration is first addressed. Using two physically distinct arguments, and based on observed material removal rates shown in Figure 5-10 and Figure 5-11 it is argued thatMRR_{cm} remains insensitive to low-amplitude vibration.

2) Evidence is presented that the total observed material removal rate, MRR_{tot}, is determined by the superposed action of:

   i) vibration-insensitive chemical-mechanical removal, MRR_{cm}, and

   ii) strictly flow-induced removal, MRR_{flow}, produced by cyclic, vibration-driven acceleration of the polishing slurry film:

$$MRR_{tot} = MRR_{cm} + MRR_{flow} \qquad \text{(F-1)}$$

3) The non-Newtonian fluid dynamics of the nano-scale, vibrationally forced polishing slurry film are analyzed via scaling arguments. Introducing reasonable assumptions concerning the physical mechanisms underlying flow-induced material removal, and using the results of the scaling argument, an experimentally consistent expression forMRR_{flow} is proposed:

$$MRR_{flow} \propto \sqrt{\frac{A}{d_o}} \cdot \omega \qquad \text{(F-2)}$$

   where $\omega = 2\pi f$, and d_o is the characteristic gap thickness.

B. Insensitivity of MRR_{cm} to Vibration: Macroscale Argument

The chemical-mechanical material removal mechanism proposed by Cook [12] is characterized by enhanced diffusion of hydrogen into the workpiece matrix, driven by, and taking place in the vicinity of, nano-scale workpiece-polishing abrasive elastic contact zones. Enhanced hydrogen diffusion produces subsurface weakening of $Si - O_x$ bonds which, in turn, enhances chemical removal of near-surface silicates.

Making the reasonable assumption that Cook's chemical-mechanical removal mechanism can be modeled using Preston's equation [8], one obtains a lumped, macro-scale relationship

$$MRR_{cm}(t) = K_p \frac{F(t)}{A_o} v_r(t) \qquad \text{(F-3)}$$

where

$$F(t) = m(g + A\omega^2 sin\omega t) \qquad \text{(F-4)}$$

is the time-dependent load acting on the polishing tool, A_o is the nominal workpiece area, and $v_r(t)$ is the time-varying translational speed of the workpiece relative to the tool.The Preston coefficient, K_p, captures the effects of process parameters such as slurry composition, pH, and temperature.

Equations (F-3) and (F-4) describe material removal on the short vibration time-scale, $\tau_V = \omega^{-1}$. In order to expose the effect of the vibrational load, $m \cdot A \cdot \omega^2 sin\omega t$, on chemical-mechanical removal, Eq. (F-3) is integrated over a time scale, τ_I, that is long relative to τ_V, but short relative to the time scale for translational motion, τ_T, i.e., $\tau_V \ll \tau_I \ll \tau_T$, where $\tau_T = \frac{D_o}{v_{rc}}$, v_{rc} is the characteristic translational speed of the workpiece relative to the tool, and D_o is the workpiece diameter. [Note, in the present

experiments,$\tau_T \sim 10\,s$ and $\tau_{V,max} \sim 2\,ms.$]. On the intermediate time scale,τ_I,$v_r(t)$ remains nominally fixed and integration of Eq. (F-4) shows that

$$\overline{MRR_{cm}} = \frac{1}{\tau_I}\int_{t_o}^{t_o+\tau_I} MRR_{cm}(t)dt = K_p \frac{mg}{A_o} v_r(t_o) \qquad \text{(F-5)}$$

Thus, at least in theory, vibration appears to play no role in chemical-mechanical removal.

An important question concerns the effect of *non-sinusoidal* load motion on the sensitivity of chemical-mechanical removal to vibration. Specifically, when cyclic load motion is non-sinusoidal and the average vibrational load through each cycle is non-zero (where the latter is zero for sinusoidal motion), the chemical-mechanical removal mechanism does become sensitive to vibration. Moreover, under these circumstances, $\overline{MRR_{cm}} \propto A \cdot f$, consistent with the experimental low-amplitude results shown in Figs 7a and 7b. [The latter relationshipcan be shown by expressing a non-sinusoidal, cyclic load in a Fourier expansion.] However, in order for load motion to differ significantly from the imposed sinusoidal motion, the extremely thin slurry film, again having thickness on the order of three times the root mean tool roughness, $3R_q \sim d_o \sim 200\,nm$,must exert a viscous damping force, $F_{viscous}$, comparable to the (total) elastic contact force, $F_{elastic}$, extant between tool-embeddedpolishing abrasives and the workpiece. A straightforward scaling argument, which assumes Hertzian polishing abrasive-workpiece contact, a uniform polishing abrasive distribution over the tool surface, and a generalized non-Newtonian slurry (see Sec. E below), allows comparison of these forces, showing that:

$$\frac{F_{viscous}}{F_{elastic}} \sim \frac{\mu_\infty \delta_c \omega R_q^{-1} A_o}{(E\delta_c R_q^{-1} a^2) N_c} \qquad \text{(F-6)}$$

where μ_∞, δ_c, E, a, and $N_c = D_o^2 d_p^{-2}$, are, respectively, the slurry viscosity at infinite strain rate (see below), the characteristic elastic deformation of tool-embedded polishing abrasives, the polishing abrasive elastic modulus, the characteristic radius of abrasive-workpiece elastic contact zones, and the characteristic total number of abrasive-workpiece contact points. In addition, D_o and d_p are, respectively, the workpiece diameter and the characteristic diameter of the polishing abrasives. Using a standard formula for a[175], $E = 1.65 \times 10^{11} Nm^{-2}$[85], and values given above for the remaining parameters, it is found that

$$\frac{F_{viscous}}{F_{elastic}} \sim 10^{-5} \qquad \text{(F-7)}$$

Thus, assuming that viscous damping represents the only physical mechanism capable of producing significant non-sinusoidal load motion, it is clear that the motion remains strongly sinusoidal, again suggesting that chemical-mechanical removal remains insensitive to vibration.

C. Insensitivity of MRR_{cm} to Vibration: Micro-scale Argument

Consider next time-dependent nano-scale elastic contact between random tool surface asperities and the workpiece. Using Greenwood and Williamson's [176] model, and assuming a Gaussian distribution of asperity, i.e., polishing abrasive, heights, it is found that, over a wide range of (ensemble averaged) elastic deformations, $\langle \delta(t) \rangle, -0.5\sigma_s \geq \langle \delta(t) \rangle \geq -3.0\sigma_s$, the time-varying, ensemble-average,total elastic stress, $\langle F(t) \rangle \langle A(t) \rangle^{-1}$, exerted by the rough tool surface on the (nominally smooth) workpiece surface remains nominally fixed:

$$\langle F(t) \rangle \langle A(t) \rangle^{-1} \sim \text{constant} \qquad \text{(F-8)}$$

Thus, assuming the validity of Preston-law material removal, represented by Eq. (F-3), this second analysis again strongly suggests that, even for vibration-induced elastic deformations much larger than those expected here, the chemical-mechanical removal mechanism remains largely insensitive to vibration. Here, instantaneous averages, $\langle \cdot (t) \rangle$, are carried out over the distribution of asperity (embedded abrasive) heights, $\langle F(t) \rangle$is the total, instantaneous, ensemble average force produced by elastic deformation of tool asperities, $\langle A(t) \rangle$ is the associated total, instantaneous, ensemble average elastic contact area, and $\sigma_s \sim R_q$is the standard deviation of surface asperity heights relative to the mean datum.

D. Slurry Fluid Dynamics

Next to be considered are the fluid dynamics within the slurry-filled gap between the polishing tool and workpiece; the analysis applies to both the small- and large-amplitude limits defined above. The objectives center on the following:

i) Expose the dominant fluid dynamic processes within the gap.

ii) Identify, and determine the relative importance of, flow processes capable of producing workpiece material removal.

iii) Propose a simple linear relationship between the flow-mediated material removal rate, MRR_{flow}, and the dominant fluid dynamic features identified in ii).

Figure F-1 shows the reference plane, Ω, defined as coincident with the mean datum of the tool surface. Since the measured root mean square roughness of the tool surface, R_q, is on the order of 70 nm, and since this corresponds approximately to a characteristic valley-to-peak distance of $6R_q$, or equivalently, to three times the

characteristic mean datum-to-peak height, the characteristic gap thickness, d_o, is assumed to be on the order of 200 nm; based on the phase lag measurements, Table III above, it is assumed that d_o remains fixed under vibrational motion.

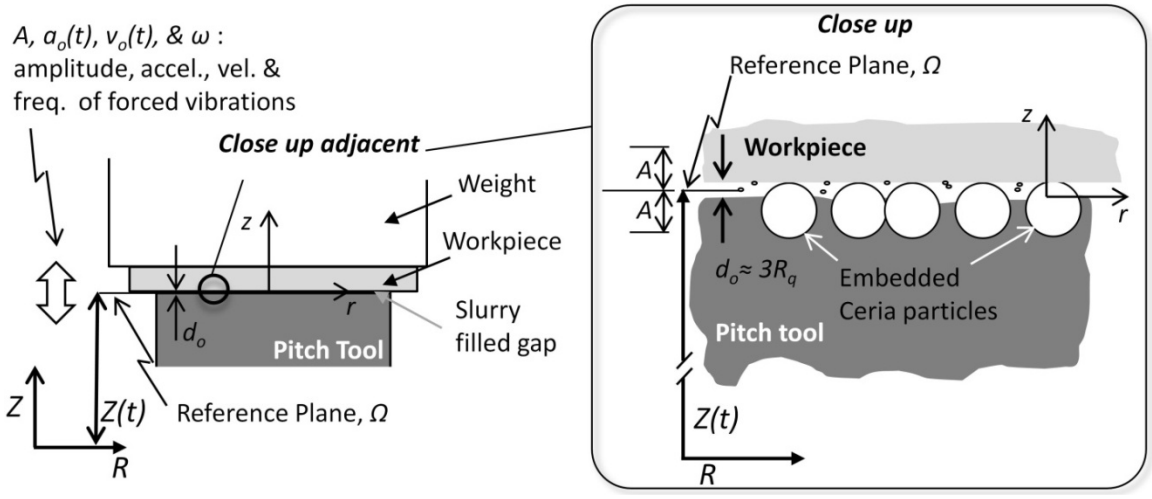

Figure F-1: Model definition and parameters.

E. Non Newtonian Behavior of Slurry

At the outset, five significant limitations are noted, all of which pertain to how the slurry is modeled. First, under the experimental conditions used (which are representative of ceria-based polishing processes), the slurry behaves in a strongly non-Newtonian fashion [177]. Second, while Hsu and Nacu [177] observed shear-thinning behavior for ceria-water mixtures, their measurements were limited to maximum shear rates on the order of 100 s^(-1); shear rates in the present experiments are approximately four orders of magnitude beyond this. Third, the highest ceria-to-water volume ratio examined by Hsu and Nacu was 4.32%; the volume ratio used here is 10 %. Fourth, it appears that no constitutive relationships have been established for ceria-water-based mixtures of any composition. Fifth, thermophysical properties, in particular, the shear-dependent

viscosity, as well as thermal conductivity and specific heat, are unknown. In light of these limitations, the mixture of free ceria particles, water, and products of the polishing process are modeled as a simple, homogeneous, though non-Newtonian fluid. Thus, the generic equation of fluid motion, expressed in terms of the fluid stress tensor, $\tau = \tau(r,t)$, and pressure, $P = P(r,t)$,relative to a tool-fixed coordinate system (z,r), is given by

$$\rho[v_{,t} + v \cdot \nabla v] = -\nabla P + \nabla \cdot \tau + \rho g - \rho a_o - \rho v_o \cdot \nabla v \qquad \text{(F-9)}$$

where ρ is the slurry density, $a_o = a_o(t)$ and $v_o = v_o(t)$are the vertical, cyclic, vibration-driven acceleration and velocity of the tool-fixed coordinate system,$v = v(r,t)$is the slurry velocity field, and $g$the gravity vector. The velocity field, v, associated with the fluid within the gap, is that observed in the non-inertial coordinate system attached to the reference plane, Ω; the flow problem is cast in polar-cylindrical coordinates so that $v = ue_r + ve_\theta + we_z$. In order to highlight the central role of vibration on slurry motion, the last two terms on the right of Eqn. (F-9), which correspond to vibration-driven inertial terms, are viewed as effective body forces.

Considering the constitutive behavior of the slurry, the ceria-water mixture is assumed to behave as a generalized Newtonian fluid [178]:

$$\tau_{ij} = \mu(\dot{\gamma})\dot{\gamma}_{ij} \qquad \text{(F-10)}$$

where$\dot{\gamma}_{ij} = \dot{\gamma}$is the strain rate tensor, and $\dot{\gamma} = Det\dot{\gamma}$is the determinant of $\dot{\gamma}$.Using a generalized Quemeda model [179],and carrying out measurements over fairly wide ranges of slurry pH's, temperatures, and ceria-water weight ratios, Hsu and Nacu [177] determined $\mu(\dot{\gamma})$ for water-ceria mixtures. Although the largest shear rates measured were only on the order of $100\, s^{-1}$,much smaller than the approximate $10^4 - 10^5 s^{-1}(\sim A\omega d_o^{-1})$shear rates extant here, Hsu and Nacu's data suggest that μbegins to

approach asymptotic values, μ_∞,for strain rates greater than approximately $100\ s^{-1}$,consistent with the assumed existence of μ_∞in Quemeda's model [179]. Here, it is assumed that

$$\mu(\dot{\gamma}) = \mu_\infty \tag{F-11}$$

and in numerical estimates, the volume fraction-dependent asymptotic viscosities reported in [177] are used. Thus, Eq. (10) becomes

$$\tau_{ij} = \mu_\infty \dot{\gamma}_{ij} \tag{F-12}$$

F. Order of Magnitude Analysis: Gap Fluid Dynamics

Determining the appropriate radial and vertical velocity scales, $u_s$and w_s, for the slurry within the gap is crucial to arriving at a physically consistent picture of gap dynamics.[Aside: Physical consistency here refers to velocity and length scale estimates that lead to: i) mathematically-consistent ordering of terms in the governing momentum equations, (F-9); ii) a physically reasonable picture of gap fluid dynamics; and iii) experimentally verifiable predictions of flow-induced material removal.] A physically consistent estimate for w_s follows from the z-component of Eq. (F-9). Specifically, it is assumed that vertical vibrational forcing, represented by the penultimate right-side term in Eq. (F-9), induces a significant advective vertical acceleration, $ww_{,z}$.Thus, in an order of magnitude sense, $ww_{,z} \sim a_{oz} \sim A\omega^2$. Approximating $ww_{,z}$as$w_s^2 d_o^{-1}$,where the vertical length scale, $z_s = d_o$, then yields

$$w_s = \sqrt{A d_o}\,\omega \tag{F-13}$$

In order to determine a physically consistent radial velocity scale, u_s, some care is required. Specifically, it is recognized that due to the proliferation of tool-embedded polishing abrasives filling the gap space, radial velocities undergo significant variations

in magnitude and direction, on radial length scales that are on the order of the characteristic gap height, d_o. (In the small-amplitude limit, radial velocities vary significantly on radial length scales on the order of either R_q or d_p,where $R_q \sim d_p \sim d_o$, and where$d_p$roughly determines the lateral spacing between embedded abrasives.) Thus, from the mass conservation constraint, given by the continuity equation, $\nabla \cdot v = 0, u_s$ follows by balancing $u_{,r}$against $w_{,z}$, or $u_s d_o^{-1} \sim w_s d_o^{-1}$, so that

$$u_s = \sqrt{A d_o}\,\omega \qquad \text{(F-14)}$$

Two consistency checks can be carried out. First, the estimates for w_s andu_s, along with the estimated vertical and radial length scales, $z_s = r_s = d_o$, and the time scale, $t_s = \omega^{-1}$, allow comparison of the magnitudes of the advective, $ww_{,z}$,and local vertical acceleration,$w_{,t}$, terms in Eq.(9):

$$\frac{ww_{,z}}{w_{,t}} \sim \frac{uw_{,r}}{w_{,t}} \sim \sqrt{\frac{A}{d_o}} > 1 \qquad \text{(F-15)}$$

While the inequality does not hold for the limited measurements carried out at $A = 100\,nm$, for all other measurements, it remains valid. Thus, the initial assumption concerning the dominance of the advective acceleration over the local is confirmed. Second, and more importantly, the velocity scales in (11) and (12), through their connection to shear stress scales, lead to theoretical material removal rates that are consistent with experimental observations.

Shear stress and pressure scales follow from (10) and (7), respectively, where terms in the strain rate tensor, $\dot{\gamma}$, are of order

$\mu_\infty w_{,r} \sim \mu_\infty w_{,z} \sim \mu_\infty u_{,z} \sim \mu_\infty u_{,r} \sim \mu_\infty w_s d_o^{-1}$; thus,

$$\tau_{rz} \sim \tau_{rr} \sim \tau_{zz} \sim \mu_\infty \frac{w_s}{d_o} \sim \mu_\infty \frac{u_s}{d_o} = \mu_\infty \sqrt{\frac{A}{d_o}}\omega \qquad \text{(F-16a)}$$

$$P \sim \tau_{ij} \sim \mu_\infty \frac{w_s}{d_o} \sim \mu_\infty \frac{u_s}{d_o} = \mu_\infty \sqrt{\frac{A}{d_o}}\omega \qquad \text{(F-16b)}$$

Note, consistent with the extreme thinness of the gap, viscous shears and pressures dominate fluid inertia, where the characteristic ratio of inertia to shear stresses (or pressure) is:

$$\frac{\rho|v\cdot\nabla v|}{\tau_{ij,j}} \sim \frac{\rho\sqrt{Ad_o}\omega d_o}{\mu_\infty} \ll 1 \qquad \text{(F-17)}$$

G. Proposed Flow-mediated Removal Mechanisms

It is proposed that flow-driven removal of workpiece material, under both the small- and large-amplitude limits, takes place by three distinct mechanisms:

i) inertial removal, via cyclic impact of fluid-borne ceria particles on the workpiece surface,

ii) suction/blowing removal via cyclic pressure gradients, and

iii) frictional removal, produced by cyclic viscous slurry shear stresses.

Additionally, it is proposed that the rate of material removal produced by each mechanism is linearly proportional to the scale of each underlying fluid dynamic process. Thus, denoting the material removal rate associated with mechanism i) as MRR_I,and those corresponding to mechanisms ii) and iii) as MRR_P and MRR_S, respectively, gives:

$$MRR_I \propto |\rho v \cdot \nabla v|_s \propto \rho w_s^2 = \rho d_o A \omega^2 \qquad \text{(F-18a)}$$

$$MRR_P \propto |\nabla \mathrm{P}|_s \propto P_s = \mu_\infty \frac{w_s}{d_o} = \mu_\infty \sqrt{\frac{A}{d_o}}\omega \qquad \text{(F-18b)}$$

$$MRR_S \propto |\tau|_s = \mu_\infty \frac{w_s}{d_o} = \mu_\infty \sqrt{\frac{A}{d_o}}\omega \qquad \text{(F-18c)}$$

Using the following characteristic magnitudes for the parameters in Eq. (F-18a)-(16c), $\mu_\infty = 10^{-3} Nsm^{-2}$[176],$\rho = 10^3 kgm^{-3}$ [176], $A = 500\,nm$, $d_o = 200\,nm$,and $\omega = 2\pi \cdot 500 s^{-1}$, and assuming the validity of Eqs. (18a)-(18c), it is found that viscous-shear-driven and suction/blowing material removal dominates inertially-driven removal:

$$MRR_S \sim MRR_P \gg MRR_I \qquad \text{(F-19)}$$

Finally, this gives the main result of the analysis: under both small- and large-amplitude vibration, the total flow-driven material removal rate, MRR_{flow}, corresponds to the sum

$$MRR_{flow} = c_1 MRR_S + c_2 MRR_P \qquad \text{(F-20)}$$

Or more specifically, from Eqs. (18b) and (18c):

$$MRR_{flow} = c_3 \mu_\infty \sqrt{\frac{A}{d_o}}\,\omega \qquad \text{(F-21)}$$

H. A Second Set of Scales for$d_o \approx A$; Analysis of the Data in Figures F-1, F-2, and F-3

A degree of uncertainty attaches to the appropriate scale for d_o, and by extension, to the corresponding velocity scales, w_s and u_s. The analysis underlying Eqs. (13) through (19) assumes that d_o is on the order of 3 ×themeasured root mean square roughness, $R_q \approx 70\,nm$. For d_o of this magnitude, and for most*A*'s tested, $d_o < A$. Under these circumstances, and as indicated in Eq. (F-15), advective acceleration is larger than local acceleration, and w_s and u_s are as given in Eqs. (13) and (14). Based on our measurements of R_q, and assuming $d_o \approx 3 \times R_q$ $(< A)$, we use these scales in analyzing the data in Fig. 5-10.

By contrast, the data in Fig. 5-11 suggests that $d_o \approx A$. Specifically, when $d_o \approx A$, the following scales emerge:

i) $w_s = A\omega$ (obtained by balancing $w_{,t}$ against a_{oz} in the z-momentum equation),

ii) $u_s = w_s = A\omega$ (from continuity),

iii) $\tau_{rz} \sim \tau_{rr} \sim \tau_{zz} \sim \mu_\infty \frac{w_s}{d_o} \sim \mu_\infty \frac{u_s}{d_o} = \mu_\infty \frac{A}{d_o}\omega$ (see, for comparison, Eq. (F-16a)), and

Using these estimates, and introducing the same assumptions underlying Eqs. (18), one obtains,

$$MRR_{flow} \propto A\omega \qquad \text{(F-22)}$$

consistent with the qualitative trend observed in Figure F-1. It is thus assumed, when analyzing the results in this figure, that $d_o \approx A$.[While both scaling lead to reasonable fits of the data in Fig. 5-10, only the second is consistent with the results in Fig. 5-11.]

Finally, since the condition $d_o < A$clearly holds for the large-amplitude data, i.e., $A \geq 5\ \mu m$, as presented in Fig. 5-13, the velocity, pressure, and stress scales in Eqs. (13) through (14) apply. Likewise, the parametric forms of MRR_I, MRR_P, and MRR_S in Eqs. (18) are assumed, leading to Eqs. (19) and (20), as well as an expression for$MRR_{flow}$of the form in Eq. (F-21), i.e., $MRR_{flow} \propto \sqrt{A/d_o}\,\omega$.

I. Combined MRR_{cm} and MRR_{flow}: Comparison with Data in Figure 5-10.

Consider measured removal rates under the small-amplitude limit, $A \lesssim 1.6\ \mu m$.Under these conditions, and as suggested by the apparent maximum gap heights, $d_{o,max} = G$, shown in Table III, it is assumed that the workpiece maintains contact with the tool surface.Thus, both chemical-mechanical [12] and flow-mediated removal take place; since, as argued above, chemical-mechanical removal appears to remain insensitive to vibration, we express the total material removal rate as:

$$MRR_{tot} = MRR_{cm} + MRR_{flow} \qquad (for A \lesssim 1.6\ \mu m) \qquad \text{(F-23a)}$$

or, using Eq. (F-21)

$$MRR_{tot} = MRR_{cm} + c_4\sqrt{\frac{A}{d_o}}\omega \qquad (for A \lesssim 1.6\ \mu m) \qquad \text{(F-23b)}$$

where, due the uncertain magnitude of μ_∞, $c_3\mu_\infty$is rewritten as c_4, while the known parameters A and $\omega$are maintained. In addition, d_o is assumed to be equal to $3R_q(= 200\ nm)$.

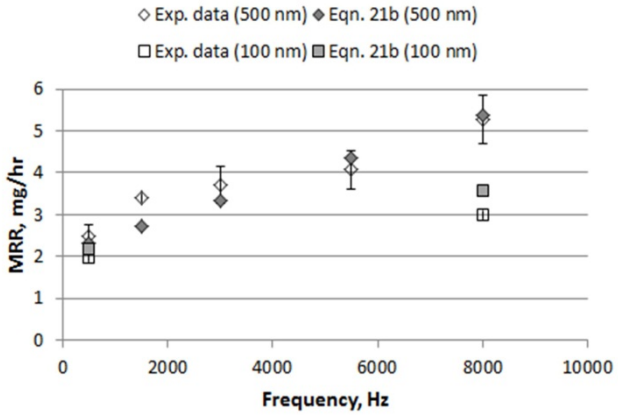

Figure F-2: Comparison between the experimental results shown in Figure 5-10 and the theoretical values fit to equation (F-23b).

Theoretically predicted MRR_{tot}magnitudes from Eq. (F-23b) are compared in Fig.5-11 against experimentally observed material removal rates shown in Fig. 5-10. As noted, two sets of measurements were performed. In the first, vibration amplitude was fixed at A=500 nm and MRR_{tot} was measured over a range of frequencies, $f(= \omega(2\pi)^{-1})$: $500\ Hz \leq f \leq 8000\ Hz$. Inthe second, A was fixed at $100\ nm$, and MRR_{tot} was measured at $f = 500\ Hz$and $f = 8000\ Hz$. The coefficient c_4, and the chemical-mechanical removal rate, MRR_{cm}, in Eq. (F-23b) were determined by a least squares fit, using the A=500 nm data, with the results$c_4 = 4.1\ (10)^{-5} mg \cdot hr^{-1} \cdot s$ and $MRR_{cm} =$

$2.10\ mg \cdot hr^{-1}(R^2 = 0.82)$. These values of c_4 and MRR_{cm} were then used to generate both sets of theoretical MRR_{tot}values shown in Fig.5-11. As shown, Eq. (F-23b) provides reasonable predictions of low-amplitude, vibration-assisted material removal, over fairly wide ranges of vibration amplitude and frequency.

J. Dependence of Small-amplitude MRR_{tot} on Nominal Vibrational Power Input– Figure 5-10.

As noted above, and as shown in Fig. 5-11, when measured material removal rates,MRR_{tot},are plotted against the nominal vibration power input to the workpiece, $\dot{W}_{in} = mgfA$, one observes an approximate linear proportionality between MRR_{tot} and $\dot{W}_{in}$:

$$MRR_{tot} \propto \dot{W}_{in}=mgfA \qquad \text{(F-24)}$$

Where m is the applied load acting on the workpiece (expressed as a mass). It is important to note that while much of the data underlying Fig. 5-11 is the same as that underlying Fig. 5-10, the range of experimental conditions exhibiting the behavior represented by Eq. (F-24) is significantly larger than that underlying Fig. 5-10. Specifically, two additional sets of measurements, obtained at $f = 500\ Hz$,$A = 1.6\ \mu m$, and$m = 2\ kg$, as well as at$f = 8000\ Hz$, $A = 500\ nm$, and $m = 1\ kg$,are observed to follow Eq. (F-24); see Fig. 5-11.

Using the scales noted above, i.e., those associated with the approximate equality,$d_o \approx A$,the observed dependence of MRR_{tot} on $f \cdot A$ (or equivalently, $\omega \cdot A$) can again be explained in terms of gap fluid dynamics. Thus, assuming that chemical-mechanical and flow-driven removal are superposed, as represented by Eq. (F-23a), and using Eq, (22) for MRR_{flow}, we obtain:

$$MRR_{tot} = MRR_{cm} + c_5 mgA\omega (for A \lesssim 1.6\ \mu m) \qquad \text{(F-25)}$$

As a check on the consistency of the above scaling analyses, we note that since Eqs. (23b) and (25) both describe material removal in the small amplitude limit, $A \lesssim 1.6\ \mu m$, then $c_5$should be related to $c_4$according to

$$c_5 mg\omega A = c_4 \sqrt{\frac{A}{d_o}}\omega \qquad \text{(F-26)}$$

Thus, c_5 is determined by a least squares fit of the experimental magnitudes of the product,$mgA\omega$, against $c_4\sqrt{A/d_o}\,\omega$, where $c_4 = 4.1\ (10)^{-5} mg \cdot hr^{-1} \cdot s$(determined above); the result is $c_5 = 7.55 mg \cdot hr^{-1} \cdot W^{-1} (R^2 = 0.76)$.

Using this value forc_5 and $MRR_{cm} = 2.10\ mg \cdot hr^{-1}$ (determined above) in Eq. (F-25) yields the theoretical points shown in Figure 5-14b. The reasonable agreement observed between predicted and measured MRR_{tot}, again seen over a wide range of experimental conditions, provides further evidence of the validity of the proposed picture of small-amplitude, in-gap fluid dynamics and material removal.

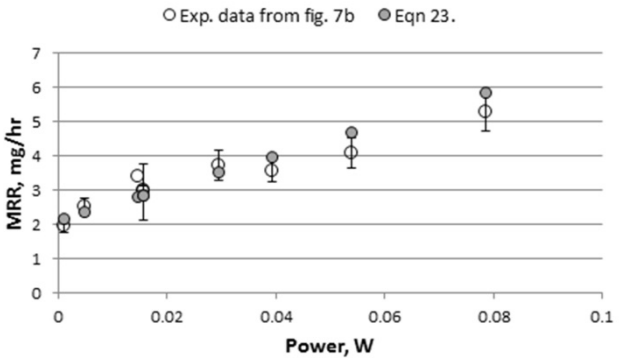

Figure F-3: Comparison between the experimental results shown in Figure 5-11 and the theoretical values fit to equation (F-25).

K. MRR_{flow} only: Non-contact, Large Amplitude Limit –Figure 5-13.

As shown in Table III, under conditions where $A \geq 5\mu m$,maximum gap thicknesses, $d_{o,max} = G$,are, larger than the $3R_q \approx 200\, nm$.A simple argument in which complete cyclic closure of the gap is assumed, and in which the associated volumetric flow rate, *Q=Q(r,t)*, is determined (via integration of the continuity equation), shows that corresponding mean radial velocities,$\bar{u} = \bar{u}(r,t) = Q(r,t)(2\pi r d_o)^{-1}$, are,at the edge of the workpiece, on the order of $50\, ms^{-1}$. Since slurry velocities of this magnitude are never observed, it becomes apparent that for $A \geq 5\mu m$, the gap never completely closes, so that the workpiece and polishing tool remain completely out of contact.

Thus, referring to Eq. (F-23b), the total material removal rate is given by

$$MRR_{tot} = MRR_F = c_6\sqrt{\frac{A}{d_o}}\,\omega\ (for\ A \geq 5\ \mu m) \qquad \text{(F-27)}$$

Equations (F-23b) and (F-27) model physically distinct polishing conditions. In the first case, material removal occurs via combined chemical-mechanical and flow-mediated mechanisms, taking place within thin slurry gaps of height $d_o \sim 3R_q$, where the gapsare punctuated by numerous polishing abrasive asperities; see Figure 6-3. In the second, the characteristic gap height, d_o, is much larger than R_q.Due to this difference, it is expected, and observed, that the proportionality constants, c_4 and c_6, differ.

Thus, the coefficient c_6 is determined, again by a least squares fit, using the four material removal rates, MRR_{tot},observed under large amplitude conditions, $A \geq 5\ \mu m$, with the result $c_6 = 2.75\ (10)^{-4} mg \cdot hr^{-1} \cdot s (R^2 = 0.79)$. Using this $c_6$in Eq. (F-27) then yields the four predicted MRR_{tot}magnitudes presented in Fig. 13.As shown,

theoretically predicted, strictly flow-mediated removal rates are,over $5\ \mu m \leq A \leq 25\ \mu m$, in reasonable agreement with those observed.

Finally, the above scaling analyses can be used to explain the qualitative trends in measured MRR_{tot}, as observed in Figure 5-13.Considering the dependence of the characteristic vertical and radial in-gap velocity scales, $w_s = u_s = \sqrt{d_o A}\omega$, on amplitude, A, as well as the experimentally observed dependence of gap height, d_o, on A, it is found that for $0.1\ \mu m \leq A \leq 10\ \mu m$, fluid velocities increase at a faster rate with A than does d_o. Given the assumed linear dependence of MRR_{flow} on the characteristic slurry shear stresses, τ_{rz}, τ_{rr}, and τ_{zz}, as well as on the characteristic pressure, P_s - all of which are on the order of $\mu_\infty w_s d_o^{-1}$- it thus appears that the observed roll-off in $MRR_{tot}$for $A \leq 10\ \mu m$reflects a roll-off in in-gap fluid stresses. Similarly,

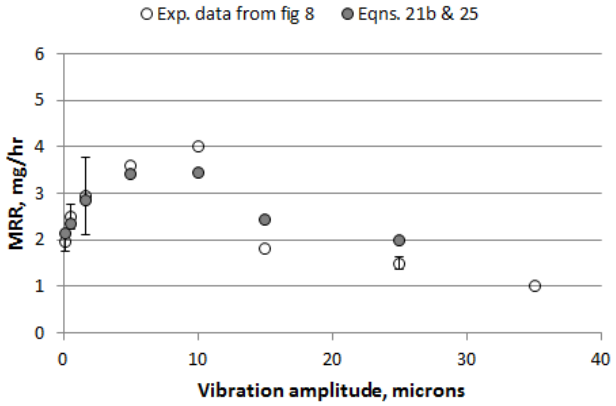

Figure F-4: Comparison between the experimental results shown in Figure 5-13 and the theoretical values obtained from equations (F-23b) and (F-27).Equation (F-23b) is used for $A \lesssim 1.6\ \mu m$ and equation (F-27) is used for $A \geq 5\ \mu m$.

The decay in observed MRR_{tot} for $A \geq 10\ \mu m$ reflects a faster rate of increase in gap thickness, $d_o = d_o(A)$, than the rate of increase in $w_s = w_s(A)$ and $u_s = u_s(A)$; thus, fluid shears and associated $MRR_{tot}'s$ decay.

APPENDIX G: MATLAB CODE FOR PARTICLESSIZE, SNOWFLAKES.M

How the Granulometry of Snowflakes program works:

This example shows how to calculate the size distribution of snowflakes in an image by using Granulometry. Granulometry determines the size distribution of objects in an image without explicitly segmenting (detecting) each objects first.

Read Image:

Read in the 'snowflakes.png' image, which is a photograph of snowflakes.

```
I = imread('snowflakes.png');
figure, imshow(I)
```

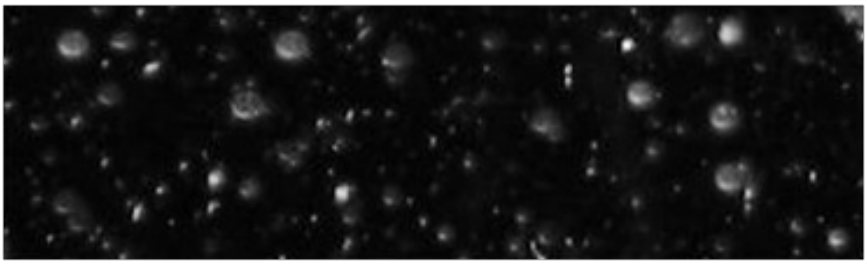

Figure G-1: photograph of snowflakes.

Enhance Contrast:

The first step is to maximize the intensity contrast in the image. It can do this using ADAPTHISTEQ, which performs contrast-limited adaptive histogram equalization. Rescale the image intensity using IMADJUST so that it fills the data type's entire dynamic range.

```
claheI = adapthisteq(I,'NumTiles',[10 10]);
claheI = imadjust(claheI);
imshow(claheI);
```

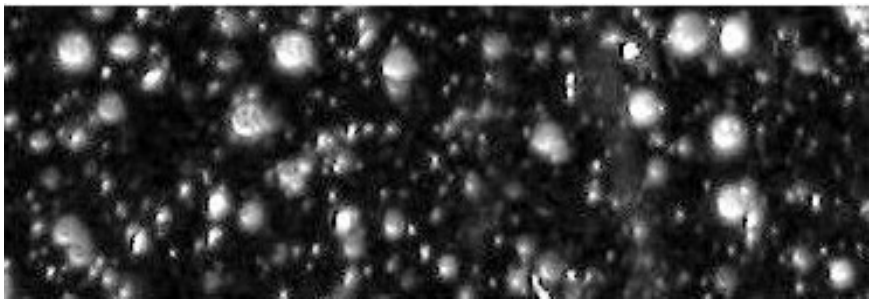

Figure G-2: Enhanced image.

Determine Intensity Surface Area Distribution in Enhanced Image:

Granulometry estimates the intensity surface area distribution of snowflakes as a function of size. Granulometry likens image objects to stones whose sizes can be determined by sifting them through screens of increasing size and collecting what remains after each pass. Image objects are sifted by opening the image with a structuring element of increasing size and counting the remaining intensity surface area (summation of pixel values in the image) after each opening.

Choose a counter limit so that the intensity surface area goes to zero as you increase the size of your structuring element. For display purposes, leave the first entry in the surface area array empty.

```
for counter = 0:22  %particles are disk type and counter is in radius
remain = imopen(clahel, strel('disk', counter));
intensity_area(counter + 1) = sum(remain(:));
end
figure,plot(intensity_area, 'm - *'), grid on;
title('Sum of pixel values in opened image as a function of radius');
xlabel('radius of opening (pixels)');
ylabel('pixel value sum of opened objects (intensity)');
```

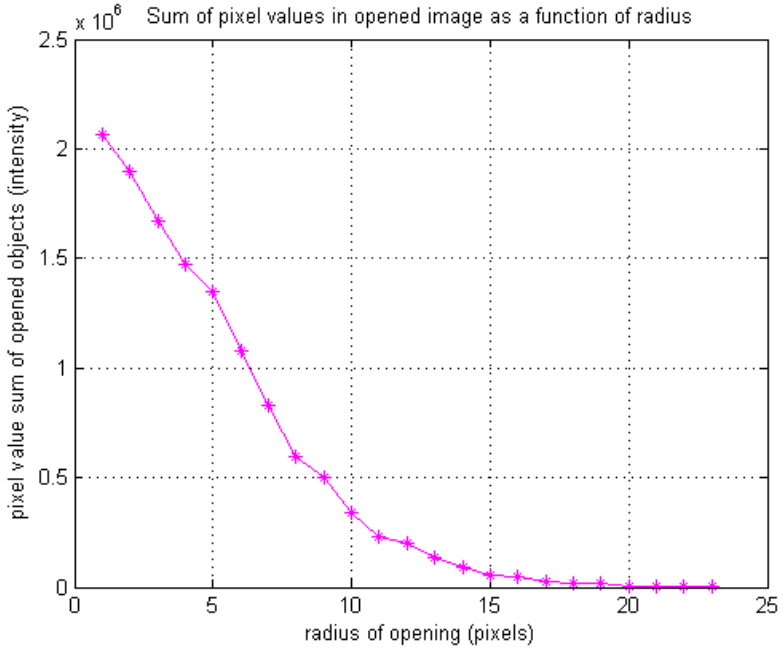

Figure G-3: Sum of pixel values.

Calculate First Derivative of Distribution:

A significant drop in intensity surface area between two consecutive openings indicates that the image contains objects of comparable size to the smaller opening. In above figure most of the particles are in between radius 5-10 pixel. This is equivalent to the first derivative of the intensity surface area array, which contains the size distribution of the snowflakes in the image. Calculate the first derivative with the DIFF function.

```
intensity_area_prime= diff(intensity_area);
plot(intensity_area_prime, 'm - *'), grid on;
title('Granulometry (Size Distribution) of Snowflakes');
set(gca, 'xtick', [0 2 4 6 8 10 12 14 16 18 20 22]);
xlabel('radius of snowflakes (pixels)');
ylabel('Sum of pixel values in snowflakes as a function of radius');
```

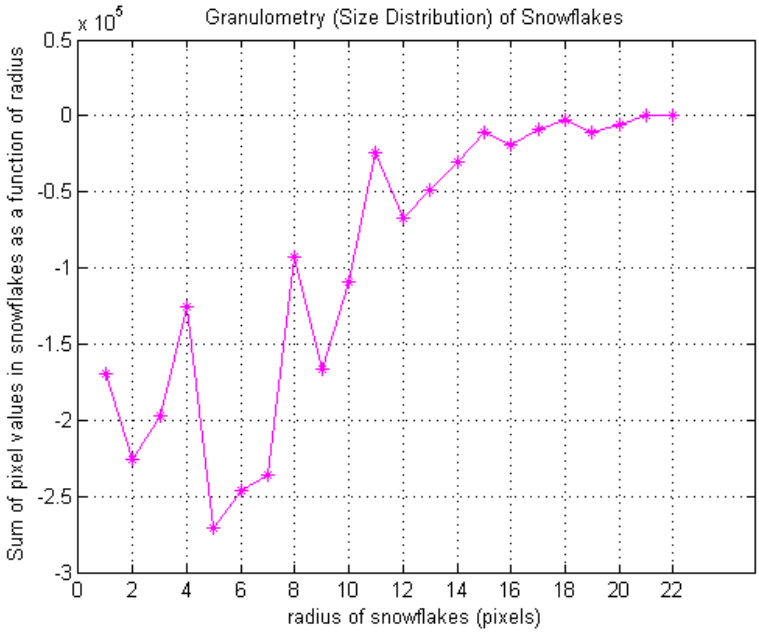

Figure G-4: First derivative of curve in Figure G-3.

Extract Snowflakes Having a Particular Radius:

Notice the minima and the radii where they occur in the graph. The minima tell you that snowflakes in the image have those radii. The more negative of the minimum point means the higher the snowflakes' cumulative intensity at that radius. For example, the most negative minimum point occurs at the 5 pixel radius mark. You can extract the snowflakes having a 5 pixel radius with the following steps.

```
open5 = imopen(claheI,strel('disk',5));
open6 = imopen(claheI,strel('disk',6));
rad5 = imsubtract(open5,open6);          %black for 6 – black for 5
imshow(rad5,[]);
```

Figure G-5: Post processed image.

APPENDIX H: MATLAB CODES FOR PERCENTAGE OF BRIGHT AREA

```
Clear all;

filter_cutoff = 100 ; %70% of the rms of the image in line 98

% Opens gui browser for STL file selection.
[Filename, Pathname, Filterindex] = uigetfile('*.jpg', 'Pick a JPG file.');

ifisequal(Filename,0) || isequal(Pathname,0)
disp('User pressed cancel')
else
disp(['User selected ', fullfile(Pathname, Filename)])

% Merges Pathname and Filename for opening image and creates Excel
% version to save to.
JPGFile = strcat(Pathname,Filename);
XLSFile = strcat(Pathname,Filename(1:end-4),'_enhanced','.xlsx');

% This is for determining the light intensity mean and STD
% reads jpg image into MATLAB
   I=imread(JPGFile);

% Converts image from RGB to gray scale matrix also turns into a 2d matrix
   g=rgb2gray(I);

%select square to crop the gray pic
   r=0;
   c=0;
rend=422;   %Asoft = 757*1004 and Ahard = 623*833
cend=528;
RMSsum=0.00;
i=1;
whilei<=(rend-r)
      j=1;
while j<=(cend-c)
x(i,j)=g(r+i,c+j);
RMSsum = RMSsum+x(i,j)^2;   % for rms calculation
         j=j+1;
end
i=i+1;
end
```

```
% This is to verify that the matrix is an n x n matrix
disp(' Matrix Size:')
disp(size(x))
MatrixMaxValue = max(max(x,[],1),[],2)
MatrixMinValue = min(min(x,[],1),[],2)
%MatrixRMSValue = sqrt(sum/(i-1))
RMSsum
% Determines size of matrix
columns = length(x(:,1));
rows = length(x(1,:));
totalsize = columns*rows;

% The following code removes all values less than the filter cutoff
% from the matrix.
%-----------------------------------------------------------------
assistmatrix = ones(columns,rows)*filter_cutoff;

% Changes X to double, reduce by filter cutoff, then change back to
% uint8. Anything of filter cutoff and before is changed to 0.
new = double(x) - assistmatrix;
new = uint8(new);
imshow(new)

% Reduces all good values to 1's and bad values to 0's.
assistmatrix = uint8(new./new);

% Calculates number of good ('1') and bad ('0') cells
cells_good = sum(sum(assistmatrix))
cells_bad = totalsize - cells_good


% Return new to original values, excluding the 0 cells
new = new + assistmatrix*filter_cutoff;
%-----------------------------------------------------------------

% Gives the average of the values in the rows and columns divided by the size of the
      matrix times a matrix of all good cells.

avg_mean = sum(sum(new)) / cells_good
avg_matrix = avg_mean * double(assistmatrix);
% Used double x because there are decimals in the average values and and the matrix
      originally is an 8bit image
stdeva = (double(new) - avg_matrix).^2;
```

```
% Summing columns and rows
stdevb = sum(sum(stdeva));

% Finding standard deviation by the n-1 formula
stdev = sqrt(stdevb/(cells_good - 1))

% Finds the rms of the image, it only needs the first element because the avg matrix is a
      ones matrix multiplied by the avg value
rms = sqrt((stdev^2 + avg_mean^2))


% This determines ballpark alignment of the dot in the picture

% Percentage of black space
percent_black = (cells_bad/(totalsize))*100

   X = grayslice(new,16);
%imshow(new);
figure, imshow(X,jet(16))

end
```

APPENDIX I: PUBLICATIONS AND PRESENTATIONS OF THE RESEARCH

Journal Publications

M. Mainuddin, R. Keanini, B. Mullany, "Increasing polishing material removal rates through externally applied vibrations" Ready to submit in Int. J. of Abrasive Technology.

B. Mullany, M. Mainuddin, W. Williams, R. Keanini, "An Experimental and Analytical Investigation into the Effects of Process Vibrations on Material Removal Rates during Polishing", Journal of Applied Physics, Vol13, (22), 2013.

B. Mullany, M. Mainuddin, "The Influence of Process Vibrations on Precision Polishing Metrics", Annals of the CIRP, 61/1/2012, 555-558, 2012.

Conference Proceedings

M. Mainuddin, B. Mullany, "Evaluating the Effect of Single Frequency Vibrations on Pitch Polishing Outcomes", Optical Fabrication and Testing (OF&T), Paper OM4D.5, 2012.

M. Mainuddin, E. Browy, B. Mullany, "Design of a Test Platform to Investigate the Role of Process Vibration in Precision Polishing" ASPE 26th annual meeting, Denver, Colorado, USA. 13–18 November 2011.

M. Mainuddin, B. Mullany, "Evaluating the influence of vibrations in precision polishing", Optifab, Rochester, NY, May 2011

M. Mainuddin, B. Mullany, "Vibration Attenuation in optical pitch", ASPE 25th annual meeting, Atlanta, GA, USA. 2010.

Oral Presentation

"Evaluating the influence of vibrations in precision polishing" Presented at Optifab-SPIE conference, Rochester, NY, 2011.

Poster Presentations

Design of a Test Platform to Investigate the Role of Process Vibration in Precision Polishing. ASPE 26th annual meeting, Denver, Colorado, USA, 2011.

Vibration Attenuation in optical pitch, ASPE 25th annual meeting, Atlanta, GA, USA, 2010.